Study of Topological Weyl Points In Metamaterials

Guilherme Ruivo Lopes da Fonseca

Thesis to obtain the Master of Science Degree in

Engenharia Electrotécnica e de Computadores

Supervisors: Prof. Filipa Isabel Rodrigues Prudêncio
Prof. Mário Gonçalo Mestre Veríssimo Silveirinha

Examination Committee

Chairperson: Prof. José Eduardo Charters Ribeiro da Cunha Sanguino
Supervisor: Prof. Filipa Isabel Rodrigues Prudêncio
Member of the Committee: Prof. Sylvain Arnaud Lannebère

November 2022

Declaration

I declare that this document is an original work of my own authorship and that it fulfils all the requirements of the Code of Conduct and Good Practices of the Universidade de Lisboa.

Acknowledgments

First, I want to acknowledge the invaluable role of my supervisors Filipa, Paloma and Mário in edifying me both academically and personally with their teachings. I wholeheartedly thank them for their patience and guidance all the way through the realization of this work.

I would also like to thank my colleagues María, João and Rodrigo for their delightful company at the IT laboratory, and with whom I shared wonderful conversations regarding Science and Life.

I wish to recognize Mariana, Augusto, André, André, Kevin and Brian for being a bastion of support and for showing me the true meaning of friendship. I can't thank you enough.

I owe an eternal dept of gratitude to my mother Paula, my father José and my big brother Gonçalo whose unconditional love allowed me to grow into the person I am.

Finally, I want to acknowledge Joana for the strength, motivation and joy that she constantly provides and for making me strive to be a better person every day.

This work was supported by Fundação para a Ciência e a Tecnologia under project HelicalMETA, UIDB/50008/2020. I also thank Instituto de Telecomunicações for hosting me from January 2021 up until the conclusion of this dissertation.

...para a minha avó Lurdes.

Abstract

One of the main goals in Photonics is the efficient and robust manipulation of light. Topological Photonics offers a path towards this objective by realising electromagnetic modes with protected propagation. In recent years, and inspired by the success of topological materials, where electron propagation is robust against a range of defects and disorder, there has been much interest in topological photonic modes. In this thesis we study two topological photonic systems: a reciprocal chiral metamaterial consisting of an array of metal wires in the shape of elliptical helices; and a magnetized plasma which is a naturally existing continuous medium. Both of these structures display Weyl points which are topological band degeneracies in 3 dimensions that arise at the linear crossing between longitudinal plasmonic modes and transverse modes. First, we analyse how nonlocality, a phenomenon present in these materials, affects the emergence of these three-dimensional linear degeneracies. Next, the topological properties of the magnetized plasma are characterized by a first principles method. Specifically, a photonic Green's function formalism is used in order to study the influence of Weyl degeneracies on the topology in 3-dimensional wave vector space and we calculate their topological charge. We apply two different regularization procedures in order to obtain well-defined topological invariants: introducing the effects of charge diffusion due to electron-electron repulsive interactions; and the application of a full wave vector cut-off. With our approach, we are able to compute the topological charge of Weyl points in metamaterials with in a computationally efficient way.

Keywords

Metamaterials; Helical Metamaterial; Band Structures; Weyl Points; Chern Number; Topological Photonics.

Resumo

Um dos principais objectivos da Fotónica é a manipulação eficiente e robusta da luz. A Fotónica Topológica oferece um caminho na direcção deste objectivo ao realizar modos electromagnéticos com propagação protegida. Recentemente, e inspirado pelo sucesso dos materiais topológicos, onde a propagação de electrões é resistente contra uma variedade de defeitos e desordem, adveio bastante interesse em modos fotónicos topológicos. Nesta tese, nós estudamos dois sistemas fotónicos: um metamaterial quiral recícproco consistente duma matriz de fios metálicos com a forma de helicoidais elípticas; e um plasma magnetizado que é um material contínuo existente na natureza. Ambas estas estruturas exibem pontos Weyl que são degenerações topológicas de bandas em 3 dimensões e que emergem no cruzamento linear entre modos plasmónicos longitudinais e modos transversos. Primeiramente, analisamos como a dispersão espacial, um fenómeno presente nestes materiais, afecta o aparecimento destas degenerações lineares tridimensionais. Seguidamente, as propriedades topológicas de um plasma magnetizado são caracterizadas por um método de primeiros princípios. Especificamente, um formalismo que emprega a função de Green fotónica é utilizada para estudar a influência de degenerações de Weyl na topologia dum espaço de vector de onda tridimensional e calculamos as suas cargas topológicas. Aplicam-se duas regularizações diferentes para obter invariantes topológicos bem definidos: introduz-se o efeito da difusão de cargas devido às interacções repulsivas entre electrões; e aplica-se um corte completo do vector de onda. Com a nossa abordagem, somos capazes de calcular a carga topológica de pontos Weyl em metamateriais duma maneira computacionalmente eficiente.

Palavras Chave

Metamateriais; Metamaterial Helicoidal; Estrutura de Bandas; Pontos Weyl; Número de Chern; Fotónica Topológica.

Contents

1 Introduction **1**

1.1 Sate of the Art 2

1.2 Objectives 7

1.3 Original Contributions 8

1.4 Structure of Dissertation 8

2 Methodology **9**

2.1 Dispersion Relations 10

2.2 Topological Formalism 12

2.2.1 Numerical Green's Function Formalism For A Continuum 12

2.2.2 Operator $\hat{L}_{\mathbf{k}}$ 15

3 Dispersion and Weyl Points **17**

3.1 Helical Metamaterial 18

3.1.1 Bianisotropic Model 19

3.1.2 Weyl Crossings in the Homogenization Limit 23

3.2 Magnetized Plasma 26

3.2.1 Local Model 26

3.2.2 Hydrodynamic Model 37

3.2.3 Full Cut-Off Model 40

4 Topological Characterisation of Band Structures **45**

4.1 Ill-Defined Topology of Local Model 46

4.2 Topological Study of Models With Regularized Responses 51

4.3 Convergence Study 57

5 Conclusion **61**

Bibliography **65**

List of Figures

1.1 Example of a metamaterial made by a periodic arrangement of inclusions embedded in a host medium. 2

1.2 Saddle surface with normal planes in directions of principal curvatures. 3

1.3 Illustration of unidirectional edge modes (in green) emerging from a nonreciprocal magnetized material. The ”C”s are the Chern numbers of each set of bands in grey. 4

1.4 Illustration of **a)** infinite bands in frequency and **b)** accumulating branches due to band folding when using a homogeneous medium as unit cell inclusions in a photonic crystal. . . 6

1.5 Illustration of the dispersion for the two types of Weyl point. 7

2.1 Illustration of the complex frequency integral path within a band gap of a nonreciprocal continuous medium. 13

3.1 Helical metamaterial - geometry and orientation. 18

3.2 Dispersion along the k_z axis. Crossings between longitudinal mode (green) and transverse modes (blue and yellow) are Weyl points. The parameters used here were $\omega_p = 1, \epsilon_x = 2, \epsilon_y = 1.7, \mu_t = 1, \mu_z = 1, \gamma = 0.8$. 20

3.3 Dispersion along the k_z axis with a nonlocal ϵ_z. The parameters used on both plots were $\omega'_p = 1, \epsilon_x = 2, \epsilon_y = 1.7, \mu_t = 1, \mu_z = 1$. For the plot on the left: $\alpha = 0.5, \gamma = 1$ and for the plot on the right: $\alpha = -0.1, \gamma = 0.71$. 21

3.4 Dispersion around second Weyl point with $\alpha > 0$: **a)** in $\hat{x}$ and $\hat{y}$; **b)** in $\hat{z}$ and $\hat{y}$. The parameters used here were $\alpha = 0.5, \gamma = 1, \omega'_p = 1, \epsilon_x = 2, \epsilon_y = 1.7, \mu_t = 1, \mu_z = 1$. 22

3.5 Dispersion around second Weyl point with $\alpha < 0$: **a)** in $\hat{x}$ and $\hat{y}$; **b)** in $\hat{z}$ and $\hat{y}$. The parameters used here were $\alpha = -0.1, \gamma = 0.71, \omega'_p = 1, \epsilon_x = 2, \epsilon_y = 1.7, \mu_t = 1, \mu_z = 1$. . . 22

3.6 Dispersion along k_z axis. The longitudinal mode is in green and the transverse modes are in yellow and blue. The momentum axis' values are normalized as $\overline{Z} = k_z p/(2\pi)$. 24

3.7 Dispersion in $\hat{x}$ direction, from Weyl point. The momentum axis' values are normalized as $\overline{X} = k_x a/(2\pi)$. 24

3.8 Dispersion in $\hat{y}$ direction, from Weyl point. The momentum axis' values are normalized as $\overline{Y} = k_y a/(2\pi)$. 25

3.9 Dispersion in the diagonal direction formed between k_x and k_y, from Weyl point. The momentum axis' values are normalized as $\overline{M} = Ma/(2\pi)$ with $M^2 = k_x^2 + k_y^2$ (for $k_x = k_y$). 25

3.10 Dispersion characteristics in the k_z axis for $\omega_c = 0.8\omega_p$ on the left, $\omega_c = 1.2\omega_p$ on the right and $\omega_p = 0.5c$ in both plots. The longitudinal mode is highlighted in red. 28

3.11 Three-dimensional dispersion showcasing two crossings. Parameters used here were for $\omega_c = 0.8\omega_p$ and $\omega_p = 0.5c$ 29

3.12 Three-dimensional dispersion showcasing four crossings. Parameters used here were for $\omega_c = 1.2\omega_p$ and $\omega_p = 0.5c$ 29

3.13 TM modes' dispersion in the xoy plane for $\omega_c = 0.8\omega_p$ on the left, $\omega_c = 1.2\omega_p$ on the right and $\omega_p = 0.5c$ in both plots. 30

3.14 Dispersion of the TM modes in blue and TE modes in red in the xoy plane for $\omega_c = 0.8\omega_p$ on the left, $\omega_c = 1.2\omega_p$ on the right and $\omega_p = 0.5c$ in both plots. 31

3.15 Varying k_z shows that there is no high-frequency band gap before the 1st Weyl point. From left to right: $k_z = 0$, $k_z = \frac{3}{4}W_1$ and $k_z = W_1$, with W_1 being the location of the 1st Weyl point in momentum space. The low-frequency band gap is present. The yellow arrows point in the orientation of increasing values in k_z. Parameters used here were $\omega_c = 1.2\omega_p$ and $\omega_p = 0.5c$ 33

3.16 A full high-frequency band gap is observable only for a high value of k_z, after the 1st Weyl point. From left to right: $k_z = \frac{5}{4}W_1$, $k_z = W_2$ and $k_z = \frac{5}{4}W_2$, with W_1 and W_2 being the location of the 1st and 2nd Weyl points in momentum space. The low-frequency band gap is present before and after the 2nd Weyl point. The yellow arrows point in the orientation of increasing values in k_z. Parameters used here were $\omega_c = 1.2\omega_p$ and $\omega_p = 0.5c$ 33

3.17 Dispersion in xoy plane ($k_z = 0$) with new ϵ_z. TM modes are in blue and TE mode is in red. Parameters used on the left were $\omega_c = 0.8\omega_p$ $\omega_p' = \sqrt{2}\omega_p$, $\omega_c = 1.2\omega_p$ $\omega_p' = \sqrt{2.8}\omega_p$ on the right and $\omega_p = 0.5c$ in both plots. 35

3.18 Dispersion in $\hat{z}$ direction with new ϵ_z. The longitudinal mode is in red. Parameters used on the left were $\omega_c = 0.8\omega_p$ $\omega_p' = \sqrt{2}\omega_p$, $\omega_c = 1.2\omega_p$ $\omega_p' = \sqrt{2.8}\omega_p$ on the right and $\omega_p = 0.5c$ in both plots. 35

3.19 3-dimensional dispersion with shifted plasma frequency in the $\hat{\mathbf{z}}$ direction. The parameters used here were $\omega_c = 1.2\omega_p$, $\omega_p' = \sqrt{3}\omega_p$ and $\omega_p = 0.5c$. 36

3.20 Dispersion in xoy plane ($k_z = 0$) - varying with β: from left to right, $\beta = 0.05c$, $\beta = 0.1c$, $\beta = 0.3c$. The TM modes are displayed in blue and the TE modes are displayed in red. All of the plots have the parameters $\omega_c = 0.8\omega_p$, $\omega_p = 0.5c$. 38

3.21 Dispersion in the k_z axis - varying with β: from left to right, $\beta = 0.05c$, $\beta = 0.1c$, $\beta = 0.3c$. The longitudinal mode is displayed in red and the transverse modes are displayed in blue. All of the plots have the parameters $\omega_c = 0.8\omega_p$, $\omega_p = 0.5c$. 38

3.22 Showcasing the three possible cases of Weyl crossings in the k_z axis - varying with β: from left to right, $\beta = 0.1c$, $\beta \approx 0.189c$, $\beta = 0.3c$. The longitudinal mode is displayed in red and the transverse modes are displayed in blue. All of the plots have the parameters $\omega_c = 1.3\omega_p$, $\omega_p = 0.5c$. 39

3.23 Dispersion surfaces and isofrequency curves around Weyl point in **a)** $\hat{\mathbf{x}}$ and $\hat{\mathbf{y}}$ directions and in **b)** $\hat{\mathbf{z}}$ and $\hat{\mathbf{x}}$ directions. The parameters used here were $\beta = 0.6c$, $\omega_c = 0.2\omega_p$ and $\omega_p = 0.5c$. 39

3.24 Dispersion in xoy plane - varying with k_{max}: from left to right, $k_{max} = 100\omega_p/c$, $k_{max} = 10\omega_p/c$, $k_{max} = 2\omega_p/c$. The TM modes are displayed in blue and the TE modes are displayed in red. All of the plots have the parameters $\omega_c = 0.8\omega_p$, $\omega_p = 0.5c$. 41

3.25 Dispersion in the k_z axis - varying with k_{max}: from left to right, $k_{max} = 100\omega_p/c$, $k_{max} = 10\omega_p/c$, $k_{max} = 2\omega_p/c$. The longitudinal mode is displayed in red and the transverse modes are displayed in blue. All of the plots have the parameters $\omega_c = 0.8\omega_p$, $\omega_p = 0.5c$. . 41

3.26 Dispersion surfaces and isofrequency curves around Weyl point in **a)** $\hat{\mathbf{x}}$ and $\hat{\mathbf{y}}$ directions and in **b)** $\hat{\mathbf{z}}$ and $\hat{\mathbf{x}}$ directions. The parameters used here were $k_{max} = \omega_p/c$, $\omega_c = 1.2\omega_p$ and $\omega_p = 0.5c$. 42

3.27 Dispersion in xoy plane with new ϵ_z. TM modes are in blue and TE mode is in red. Parameters used on the left were: $\omega_c = 0.8\omega_p$ $\omega'_p = \sqrt{2}\omega_p$. On the right: $\omega_c = 1.2\omega_p$ $\omega'_p = \sqrt{2.8}\omega_p$. On both plots were: $\omega_p = 0.5c$ and $k_{max} = \omega_p/c$. 42

4.1 Dispersion in the k_x axis of the TM modes of a local magnetized plasma with parameters $\omega_c = 1.2\omega_p$ and $\omega_p = 0.5c$. The band gaps are highlighted in grey. 46

4.2 Local model - dispersion in k_z and k_x. The propagating modes along k_z are showcased on the foreground. The Weyl crossing is represented by the blue circle. The parameters used here were $\omega_c = 1.2\omega_p$, $\omega'_p = \sqrt{3}\omega_p$ and $\omega_p = 0.5c$. 47

4.3 Dispersion in the k_z axis on the left exhibits the two regions of interest, in blue and orange. On the right is a cross section of the 3-dimensional dispersion (fig. 4.2), for $k_z = 0$, where the high-frequency band gap is highlighted in blue and the low-frequency one is in orange. The Weyl crossing is represented by the blue circle. The parameters used here were $\omega_c = 1.2\omega_p$, $\omega'_p = \sqrt{3}\omega_p$ and $\omega_p = 0.5c$. 48

4.4 k_x dispersion showcasing the positive and negative frequencies for $k_z = 0$. High-frequency band gaps are highlighted in blue and the low-frequency one in orange. Parameters used here were $\omega_c = 1.2\omega_p$, $\omega'_p = \sqrt{3}\omega_p$ and $\omega_p = 0.5c$. 50

4.5 Hydrodynamic model - dispersion in k_z and k_x. The propagating modes along k_z are showcased on the foreground. The Weyl crossing is represented by the green circle. The parameters used here were $\beta = 0.6c$, $\omega_c = 0.2\omega_p$, $\omega_p' = \omega_p$ and $\omega_p = 0.5c$. 51

4.6 Dispersion in the k_z axis exhibiting the two regions of interest in blue and orange. The Weyl crossing is highlighted with the green circle. The parameters used here were $\beta = 0.6c$, $\omega_c = 0.2\omega_p$, $\omega_p' = \omega_p$ and $\omega_p = 0.5c$. 52

4.7 Cross sections of the 3-dimensional dispersion (fig. 4.5) for different values of k_z. From left to right, $k_z = 0$, $k_z = W$ and $k_z = \frac{3}{2}W$. The band gaps are highlighted in orange and the Weyl point with the green circle. The parameters used here were $\beta = 0.6c$, $\omega_c = 0.2\omega_p$, $\omega_p' = \omega_p$ and $\omega_p = 0.5c$. 52

4.8 Full cut-off model - dispersion in k_z and k_x. The propagating modes along k_z are showcased on the foreground. The inner Weyl crossing is represented by the red circle and the outer one is represented by the red square. The parameters used here were $k_{max} = \omega_p/c$, $\omega_c = 1.2\omega_p$, $\omega_p' = \sqrt{3}\omega_p$ and $\omega_p = 0.5c$. 53

4.9 Dispersion in the k_z axis exhibiting the two regions of interest in blue and orange. The parameters used here were $k_{max} = \omega_p/c$, $\omega_c = 1.2\omega_p$, $\omega_p' = \sqrt{3}\omega_p$ and $\omega_p = 0.5c$. 54

4.10 First set of cross sections of the 3-dimensional dispersion (fig. 4.8) for different k_z values. From left to right, $k_z = 0$, $k_z = \frac{3}{4}W_1$ and $k_z = W_1$. The high-frequency band gaps are highlighted in blue, the low-frequency ones in orange and the inner Weyl point with the red circle. The parameters used here were $k_{max} = \omega_p/c$, $\omega_c = 1.2\omega_p$, $\omega_p' = \sqrt{3}\omega_p$ and $\omega_p = 0.5c$. 54

4.11 Second set of cross sections of the 3-dimensional dispersion (fig. 4.8) for different k_z values. From left to right, $k_z = \frac{5}{4}W_1$, $k_z = W_2$ and $k_z = \frac{5}{4}W_2$. The high-frequency band gaps are highlighted in blue, the low-frequency ones in orange and the outer Weyl point with the red square. The parameters used here were $k_{max} = \omega_p/c$, $\omega_c = 1.2\omega_p$, $\omega_p' = \sqrt{3}\omega_p$ and $\omega_p = 0.5c$. 55

4.12 The plot on top is the k_z axis dispersion of the hydrodynamic model with the Weyl pair as green circles. The plot on the bottom is the k_z axis dispersion of the cut-off model with the inner Weyl pair as red circles and the outer pair as red squares. The numbers in white circles represent the gap Chern numbers obtained in each region. Near the Weyl points of the cut-off model you can see the number that represents their topological charge. The parameters used for the hydrodynamic model were $\beta = 0.6c$, $\omega_c = 0.2\omega_p$, $\omega_p' = \omega_p$ and $\omega_p = 0.5c$ and the ones used for the full cut-off model were $k_{max} = \omega_p/c$, $\omega_c = 1.2\omega_p$, $\omega_p' = \sqrt{3}\omega_p$ and $\omega_p = 0.5c$. 56

4.13 Convergence study of the numerical gap Chern number of the high-frequency band gap in $k_z = 0$ as a function of N, for a full cut-off model with the parameters above. The parameters used here were $N_w = 150$, $\xi_{max} = 3$ and $\omega'_{gap} = 0.7$. 57

4.14 Convergence study of the numerical gap Chern number of the high-frequency band gap in $k_z = 0$ as a function of N_w and ξ_{max}, for a full cut-off model with the parameters above. The parameters used on the right plot were $N = 50$, $\xi_{max} = 3$ and $\omega'_{gap} = 0.7$ and on the left plot $N_w = 150$, $N = 50$ and $\omega'_{gap} = 0.7$. 58

4.15 Convergence study of the numerical gap Chern number for band gaps in the blue region of figure 4.9 in different cross sections, for a full cut-off model with the same constitutive parameters. The red line represents the frontier between the two topologically inequivalent subregions at the wave vector location of the Weyl crossing. The program parameters used here were $N = 50$, $N_w = 100$, $\xi_{max} = 3$ and ω'_{gap} takes a different value for cross section. 59

Acronyms

BZ	Brillouin zone
DOS	density of states
DC	direct current
DNG	“double-negative” media
EM	electromagnetic
PEC	perfectly electrical conductors
TE	transverse electric
TM	transverse magnetic

1

Introduction

Contents

1.1 Sate of the Art 2
1.2 Objectives 7
1.3 Original Contributions 8
1.4 Structure of Dissertation 8

1.1 Sate of the Art

Metamaterials are artificial structures and composite materials, not found in nature, that have tailored responses to electromagnetic waves. They are composed of unit cells made up of “meta-atoms”, periodically arranged in space and embedded in a host medium. They hold great potential because of this flexibility for realizing desired responses, by varying parameters which depend on the geometry and composition of the unit cell [1, 2]. If the meta-atoms’ size is much smaller than the wavelength of the light propagating in such media, then the metamaterial can be approximated as a continuum and its electromagnetic response can be described by effective parameters. The process that relates these effective parameters with the structure of the metamaterial unit cell is called homogenization [3, 4]. A very important example of what can be achieved with metamaterials is “double-negative” media (DNG) which have both negative permittivity and permeability [5] and that are capable of exotic phenomena such as negative refraction.

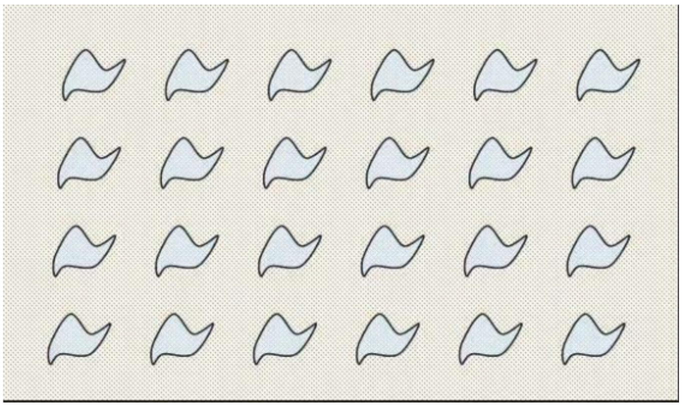

Figure 1.1: Example of a metamaterial made by a periodic arrangement of inclusions embedded in a host medium. Picture taken from [1].

Topology is a branch of mathematics that studies the properties of objects that stay invariant under a continuous transformation. When some property of a mathematical object is unaffected by a deformation it is called a topological invariant. A most notable example is the number of holes on a surface which does not change when you deform said surface continuously. This means that it is a global property since it does not depend on the local aspects of the structure, and so it is indeed a topological invariant, known as the genus g. Furthermore, two objects with the same topological invariants are defined as being topologically equivalent. For instance, continuing with the classic example, that would mean a doughnut is topologically equivalent to a coffee mug.

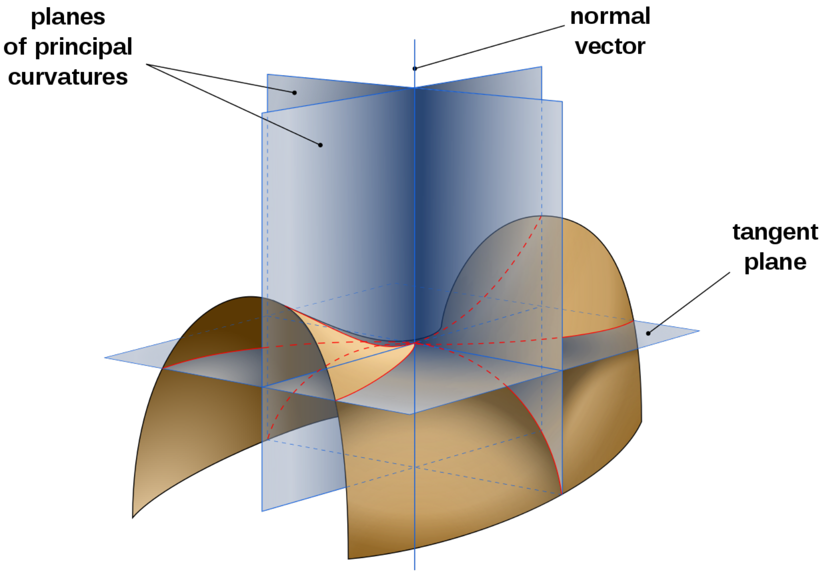

Figure 1.2: Saddle surface with normal planes in directions of principal curvatures. Picture taken from $https://en.wikipedia.org/wiki/Gaussian\_curvature$ (October 2022).

The Gaussian curvature K of a surface at any point is given by the product of the principal curvatures k_1 and k_2 at that point. The principal curvatures measure how the surface bends by different amounts in different directions. This can be related with the curvature radii R_1 and R_2 as so:

$$K = k_1 k_2 = \frac{1}{R_1 R_2}, \tag{1.1}$$

which means for example that the Gaussian curvature of a sphere is given by the inverse squared radius $1/r^2$. This is related with the number of holes on a surface S through the ”Theorema Egregium” which stands for remarkable theorem in Latin, also known as Gauss-Bonnet theorem:

$$\frac{1}{4\pi} \int\limits_S K = (1 - g) \tag{1.2}$$

Surprisingly, the genus which is a discrete global property is linked with the Gaussian curvature which is a locally defined property, after integrating it over the entire surface. It is implied then that the total curvature is discretely quantized as an integer number multiplied by a factor of 4π. Consequently, a smooth perturbation of the surface can dramatically change the local curvature and yet the total curvature remains invariant. This special invariance of a structure's properties in the face of smooth deformations justifies the importance of studying topologically protected phenomena.

Topological photonics has attracted much attention due to the prediction of topologically protected edge states that propagate without backscattering, enabling the flow of light immune to disorder and imperfections such as sharp bends or corners [6,7]. The study of this field began with photonic crystals, in which propagation of light depends on global characteristics of the band structure [8,9]. These are also periodic structures but contrarily to metamaterials, their unit cell's dimensions is on the order of the wavelength.

The topological invariant of a 2D dispersion band is the Chern number:

$$C_n = \frac{1}{2\pi} \int\limits_{BZ} \mathbf{F}_n d^2\mathbf{k}, \tag{1.3}$$

$$\mathbf{F}_{n\mathbf{k}} = i\left[\langle \partial_1 \mathbf{Q}_{n\mathbf{k}} | \partial_2 \mathbf{Q}_{n\mathbf{k}} \rangle - \langle \partial_2 \mathbf{Q}_{n\mathbf{k}} | \partial_1 \mathbf{Q}_{n\mathbf{k}} \rangle\right], \tag{1.4}$$

where BZ is a Brillouin zone, $\mathbf{F}_n$ is the Berry curvature of the n-th band and $\mathbf{Q}_{n\mathbf{k}}$ is the n-th eigenstate. The gap Chern number is by definition given by the sum of the individual Chern numbers of each set of bands below the specific band gap, and it predicts the number of chiral edge states that propagate without backscattering [9]. Additionally, the bulk-edge correspondence principle [10,11] states that when two topologically inequivalent photonic systems share a common band gap, the number of edge modes supported at an interface between them is given by the difference of the gap Chern numbers.

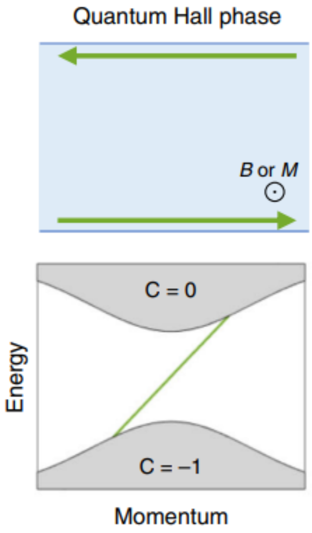

Figure 1.3: Illustration of unidirectional edge modes (in green) emerging from a nonreciprocal magnetized material. The "C"s are the Chern numbers of each set of bands in grey. Picture taken from [12]

The standard theory used to calculate these topological invariants requires the Berry curvature which depends on the normal modes of the system as given in equation (1.4) [13]. However, the formalism that will be adopted for this work makes explicit use of the photonic Green's function which is also linked with the Chern invariants [14, 15]. Specifically, the gap Chern number is given by an integral of the photonic Green's function over a contour in the complex-frequency plane that links $-\infty$ to $+\infty$ and is contained in the relevant band:

$$\mathcal{C}_{gap} = \frac{1}{(2\pi)^2} \iint\limits_{BZ} d^2\mathbf{k} \int\limits_{\omega'_{gap}-i\infty}^{\omega'_{gap}+i\infty} d\omega Tr\{\partial_1 \mathcal{G}_{\mathbf{k}}^{-1} \cdot \mathcal{G}_{\mathbf{k}} \cdot \partial_2 \mathcal{G}_{\mathbf{k}}^{-1} \cdot \partial_\omega \mathcal{G}_{\mathbf{k}}\}, \tag{1.5}$$

where Tr is the trace operator, ∂_ω=$\partial/\partial\omega$ and $\partial_j \mathcal{G}_{\mathbf{k}}^{-1} = \partial \mathcal{G}_{\mathbf{k}}^{-1}/\partial \mathbf{k}_j$ for $j = \{1, 2\}$ with $k_1 = k_x$ and $k_2 = k_y$. As previously stated, the wave vector integral domain BZ is a Brillouin zone (BZ). Although the wave vector integral might be performed over a different domain, the BZ is typically used because it is a closed surface with no boundary. This is a necessary condition for integer Chern numbers. Naturally, periodic structures which have an induced periodicity in the spectral domain are often used in studies regarding topological photonic phenomena, yet it is not a requirement.

It is possible to topologically classify continuous media, with no intrinsic periodicity, i.e with an underlying wave vector space that is an unbounded open region as was shown by M. G. Silveirinha [16]. One solution is to map each point into a unit radius sphere surface by stereographic projection. However, the condition of a wave vector space that is a closed surface with no boundary is not enough to guarantee integer Chern numbers due to ill-defined topologies. This holds true even for periodic structures. In [17] it is shown that a dispersive photonic crystal may have an ill-defined gap Chern number because of an infinite number of bands bellow the gap which might result in a divergent series. Another potential reason is the band folding that causes an accumulation of branches at a resonance frequency, due to the periodicity. Both problems are illustrated in figure 1.4. In order to overcome the problem of an ill-defined topology, a physical regularization procedure must be applied to the material response. A general solution to guarantee a well-defined topology of a continuous system is to apply a full wave vector cut-off which acts by suppressing the nonreciprocal part of the material response, for large wave vectors. Different regularization procedures can achieve two topologically inequivalent structures. This can be illustrated with an example of a torus with a vanishing inner radius which has an ill-defined topology, because it stands between two possible genera (0 or 1). A perturbation can be applied by opening a hole, turning it into a torus with $g = 1$ or by separating the top and bottom sections and turning it into a sphere with $g = 0$.

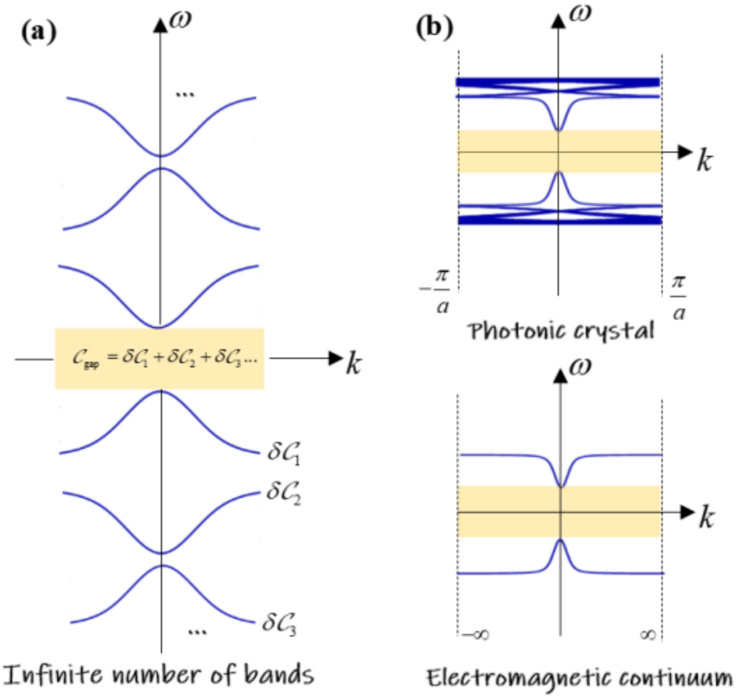

Figure 1.4: Illustration of **a)** infinite bands in frequency and **b)** accumulating branches due to band folding when using a homogeneous medium as unit cell inclusions in a photonic crystal. Picture taken from [17].

The gap Chern number which relates to the existence of edge states along one-dimensional boundaries is defined over a 2-dimensional wave vector space. However, there exists a 3-dimensional gapless topological phase characterized by 0-dimensional Weyl degeneracies which are called Weyl points. These physical entities are singular points that emerge as linear crossings between two topologically inequivalent bands. They are monopoles of the Berry curvature and come in pairs in symmetric points of momentum space with opposite charge. Initially studied in electronic systems, it is possible to find them in classical wave systems such as electromagnetic and acoustic ones. They have been realised in complex three-dimensional photonic systems, such as photonic crystals and metamaterials [18–23] and more recently in simple magnetized plasmas [24, 25]. Importantly, they only emerge in systems with a broken time-reversal symmetry, a broken inversion symmetry or both. Since they always come in pairs with opposite charges, it is only possible to create or remove them by respectively generating the Weyl point pair together or by annihilating each other. This leads to robust topological surface states between a pair of Weyl points, often called photonic Fermi arcs [12].

There are two types of Weyl points. Type-I and type-II, both being topologically nontrivial, but exhibiting different physical properties. The isofrequency surface around a type-I Weyl point is an ellipsoid, hence these are also referred as elliptical Weyl points. In the case of the type-II Weyl point, the isofrequency surface is a hyperboloid, thus these are called hyperbolic Weyl points [20]. They are also characterized by the density of states (DOS) or of modes at the frequency of the Weyl crossing. Type-I is described by a vanishing DOS and type-II by a non-zero DOS as illustrated in figure 1.5. Because of this categorical difference, the DOS related phenomena such as spontaneous emission and resonant scattering exhibit very different behaviours in the two types of photonic Weyl systems [22].

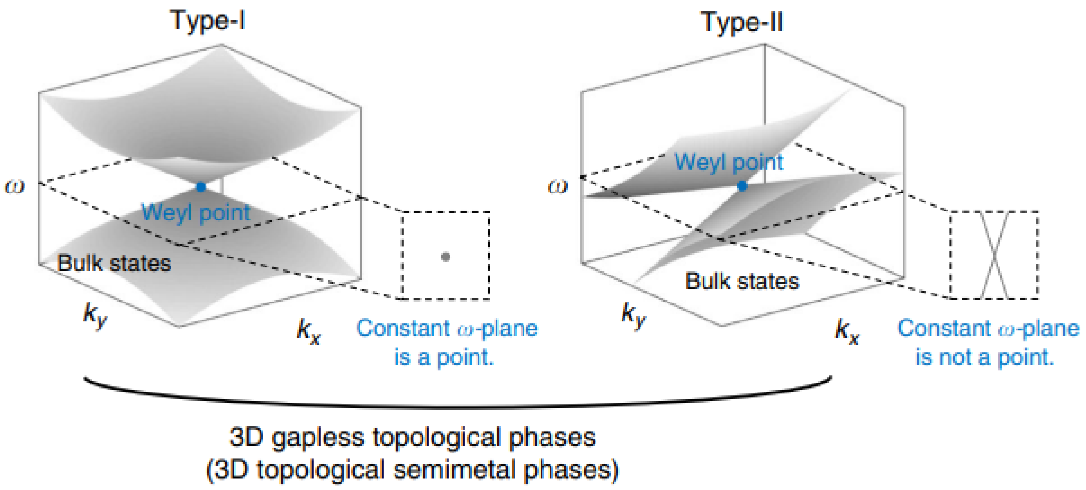
Type-I
Type-II
ω
Weyl point
Bulk states
k_y
k_x
Constant ω-plane is a point.
ω
Weyl point
Bulk states
k_y
k_x
Constant ω-plane is not a point.
3D gapless topological phases
(3D topological semimetal phases)

Figure 1.5: Illustration of the dispersion for the two types of Weyl point. Picture taken from [12]

1.2 Objectives

The main objective for this work is to compute gap Chern numbers in photonic structures that possess Weyl points and understand their influence on the Chern topological invariants.

For this purpose two structures are studied. The first one is a metamaterial composed by an array of equally spaced metal wires, shaped like elliptical helices. The second one is a well known naturally existing medium - magnetized plasma. We also analyse the conditions in which Weyl degeneracies emerge in these two systems. We apply two different regularization procedures in order to prevent ill-defined topologies in band structures.

The main computational tool employed in the work of this thesis is Wolfram Mathematica [26]. With this software, we solved eigenvalue problems, computed and plotted 2-dimensional and 3-dimensional dispersion bands and implemented the first principles Green's function method numerically.

Finally, with this work, we aim at adapting a numerical implementation of the first principles Green's function method previously developed to study topological invariants of 2D photonic Chern insulators [15, 17, 27], to a more general scenario, particularly Weyl points in a 3D magnetized plasma.

1.3 Original Contributions

The outputs of this thesis comprise the developed Mathematica programs and a poster with the title "First Principles Study of the Topological Charge of Weyl Points in a Magnetized Plasma" presented in the 16th International Congress on Artificial Materials for Novel Wave Phenomena - Metamaterials'2022, in Siena, Italy.

1.4 Structure of Dissertation

This thesis is organized as follows: Chapter 1 offers an overview of the main topics and concepts that will be dealt with throughout this dissertation. In chapter 2, a description is given about the most important methods that will be used to solve the problems presented in section 1.2. In chapter 3, the helical metamaterial and the magnetized plasma are analysed, in terms of: dispersion relation and characteristics of the bulk modes; how the Weyl points arise in these photonic systems; and most importantly, the feasibility of the application of the Green's function formalism, for the case of the magnetized plasma. Chapter 4 is the most important on in this thesis. Two magnetized plasma models with different regularized responses are topologically characterized with a numerical implementation of the Green's function formalism. In the last chapter (5), we present and summarize the main results and conclusions from throughout this work.

2

Methodology

Contents

2.1 Dispersion Relations 10

2.2 Topological Formalism 12

The methods used throughout this thesis are detailed in this chapter. They consist of the dispersion relations that describe propagation within media and the Green's function formalism that computes gap Chern numbers.

2.1 Dispersion Relations

The main tool employed in this thesis to characterise the properties of the electromagnetic (EM) modes supported by the media under study will be the dispersion relation. More specifically, it provides a connection between spatial frequency k and temporal frequency ω, depending on the direction of propagation. Here we introduce a general method to derive dispersion relations of waves for a given medium characterised by a set of constitutive parameters. To be as general as possible, a generic bianisotropic [28] medium is considered, with the following material matrix:

$$\mathbf{M} = \begin{pmatrix} \overline{\epsilon} & \overline{\xi} \\ \overline{\zeta} & \overline{\mu} \end{pmatrix}, \tag{2.1}$$

where the matrix entries are 3 by 3 tensors: $\overline{\epsilon}$ is the permittivity, $\overline{\mu}$ is the permeability and the anti-diagonal terms $\overline{\xi}$ and $\overline{\zeta}$ are the cross-coupling or the magnetoelectric coupling terms. Their elements are called the constitutive parameters. The starting point is to consider the macroscopic Maxwell's equations that define wave propagation:

$$\nabla \times \mathbf{E} = -\frac{\partial}{\partial t}\mathbf{B}, \tag{2.2}$$

$$\nabla \times \mathbf{H} = \frac{\partial}{\partial t}\mathbf{D} + \mathbf{J}, \tag{2.3}$$

$$\nabla \cdot \mathbf{D} = \rho, \tag{2.4}$$

$$\nabla \cdot \mathbf{B} = 0, \tag{2.5}$$

where $\mathbf{E}$ and $\mathbf{H}$ are the electric and the magnetic fields, $\mathbf{D}$ and $\mathbf{B}$ are the electric displacement and the magnetic induction fields and the EM sources are described by the electric current density $\mathbf{J}$ and by the electric charge density ρ. Following with the constitutive relations, which describe mathematically the electromagnetic properties of media through the material matrix. This provides a link between $(\mathbf{E}, \mathbf{H})$ and $(\mathbf{D}, \mathbf{B})$:

$$\begin{pmatrix} \mathbf{D} \\ \mathbf{B} \end{pmatrix} = \begin{pmatrix} \overline{\epsilon} & \overline{\xi} \\ \overline{\zeta} & \overline{\mu} \end{pmatrix} \begin{pmatrix} \mathbf{E} \\ \mathbf{H} \end{pmatrix} = \mathbf{M} \cdot \begin{pmatrix} \mathbf{E} \\ \mathbf{H} \end{pmatrix} \tag{2.6}$$

Since the interest of this problem is to describe propagation within the medium, sources are nullified. That means $\mathbf{J} = 0$ and $\rho = 0$. However, current displacement and charge density contributions caused by external fields in the system can be absorbed into $\mathbf{D}$ and therefore are not accounted for in equations

(2.2)-(2.5). Then, plane wave solutions with harmonic spatial and time variation of the type $e^{i\mathbf{k}\cdot\mathbf{r}}e^{-i\omega t}$ are considered. This mathematically simplifies the manipulation of Maxwell's equations because one can simply substitute the spatial and temporal derivatives as such: $\frac{\partial}{\partial t} \leftrightarrow -i\omega$, $\frac{\partial}{\partial j} \leftrightarrow ik_j$, $j = \{x, y, z\}$. Under these conditions, the represented EM vector fields are time-independent, described by an underlined notation. Equations (2.2) and (2.3) are transformed to:

$$\mathbf{k} \times \underline{\mathbf{E}} = \omega(\overline{\zeta} \cdot \underline{\mathbf{E}} + \overline{\mu} \cdot \underline{\mathbf{H}}) \tag{2.7}$$

$$\mathbf{k} \times \underline{\mathbf{H}} = -\omega(\overline{\epsilon} \cdot \underline{\mathbf{E}} + \overline{\xi} \cdot \underline{\mathbf{H}}) \tag{2.8}$$

The underline of the electromagnetic fields denotes that they are in the spectral domain. By defining an operator $\overline{k}$ such that $\overline{k} \cdot \mathbf{A} = \mathbf{k} \times \mathbf{A}$, for any vector $\mathbf{A}$:

$$\overline{k} \equiv \begin{pmatrix} 0 & -k_z & k_y \\ k_z & 0 & -k_x \\ -k_y & k_x & 0 \end{pmatrix}, \tag{2.9}$$

it is then possible to rewrite equations (2.7)-(2.8) in the form of a matrix acting on the electric field.

$$\left(\omega^2\overline{\epsilon} + \left[\overline{k} + \omega\overline{\xi}\right] \cdot \overline{\mu}^{-1} \cdot \left[\overline{k} - \omega\overline{\zeta}\right]\right) \cdot \underline{\mathbf{E}} = 0 \tag{2.10}$$

The dispersion relation of plane waves in a generic bianisotropic medium is given by the determinant of the matrix, once it is equal to zero. This gives the connection between the components of $\mathbf{k}$ and the temporal frequency ω, as:

$$\left|\omega^2\overline{\epsilon} + \left[\overline{k} + \omega\overline{\xi}\right] \cdot \overline{\mu}^{-1} \cdot \left[\overline{k} - \omega\overline{\zeta}\right]\right| = 0 \tag{2.11}$$

From equation 2.11, all of the particular cases that describe propagation in different kinds of media can be derived such as ($\mathbb{1}$ is the identity matrix):

- isotropic: $\overline{\xi} = 0$, $\overline{\zeta} = 0$, $\overline{\epsilon} = \epsilon\mathbb{1}$ and $\overline{\mu} = \mu\mathbb{1}$;
- anisotropic: $\overline{\xi} = 0$, $\overline{\zeta} = 0$ and the permittivity $\overline{\epsilon}$ and the permeability $\overline{\mu}$ tensors are matrices, each formed by different components;
- biisotropic: material matrix entries are scalar and either $\overline{\xi} \neq 0$, or $\overline{\zeta} \neq 0$ or both are non-zero.
- bianisotropic: material matrix entries are all matrices.

It is also easy to specify a particular direction of propagation for a simpler analysis. For example, plane waves travelling in the $\hat{\mathbf{z}}$ direction ($k_x = k_y = 0$) or in the xoy plane ($k_z = 0$).

2.2 Topological Formalism

2.2.1 Numerical Green's Function Formalism For A Continuum

The first principles Green's function formalism which is described by equation (1.5) is a crucial component for the work of this thesis and specifically for the execution of the main objective of computing the topological charge of Weyl points in photonic systems. Due to the 3D nature of Weyl degeneracies, which are crossings with linear dispersions along the 3 wave vector directions, we must consider the dispersion in a wave vector space with 3 dimensions. Since even a continuous medium like the magnetized plasma can have complex dispersion relations, when we consider every wave vector component, analytically computing the Green's function for every mode is not a simple task. This is why we chose to implement a numerical version of this method, in order to compute gap Chern numbers.

The photonic Green's function is defined as:

$$\mathcal{G}_{\mathbf{k}} = i\left(\hat{L}_{\mathbf{k}} - \omega\mathbb{1}\right)^{-1}, \tag{2.12}$$

where $\hat{L}_{\mathbf{k}}$ is a frequency-independent differential operator that effectively models the propagation in a dispersive medium. Typically, this entails modeling the effects of the material dispersion with additional variables that represent the internal degrees of freedom of the medium responsible for the dispersive response. It is parameterized by the real wave vector $\mathbf{k}$ and its derivation is performed for a specific medium in the next section [17].

The topological characterization of a photonic system is based on equation (1.5). If we apply the substitutions $\partial_\omega \mathcal{G}_{\mathbf{k}} = -i\mathcal{G}_{\mathbf{k}}^2$ and $\partial_j \mathcal{G}_{\mathbf{k}}^{-1} = -i\partial\hat{L}_{\mathbf{k}}/\partial k_j$, we get [15]:

$$\mathcal{C}_{gap} = \frac{i}{(2\pi)^2} \iint\limits_{BZ} d^2\mathbf{k} \int\limits_{\omega'_{gap}-i\infty}^{\omega'_{gap}+i\infty} d\omega Tr\{\partial_1\hat{L}_{\mathbf{k}} \cdot \mathcal{G}_{\mathbf{k}} \cdot \partial_2\hat{L}_{\mathbf{k}} \cdot \mathcal{G}_{\mathbf{k}}^2\} \tag{2.13}$$

Equation (2.13) shows that the gap Chern number is given by an integral along a line of the complex frequency plane parallel to the imaginary axis. The line crosses the real frequency axis on a chosen value ω'_{gap} and this value should be confined between the lower and upper limits of the respective band gap in the real frequency axis as illustrated in figure 2.1. Here, ξ denotes the imaginary part of the complex frequency and not a magnetoelectric coupling term. The same notation was chosen to be consistent with the reference article.

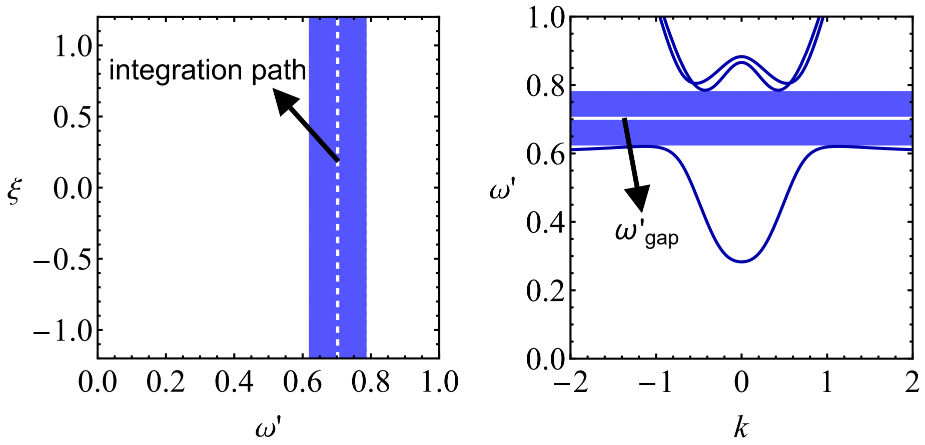

Figure 2.1: Illustration of the complex frequency integral path within a band gap of a nonreciprocal continuous medium.

The numerical implementation of equation 2.13 for a 3-dimensional continuum is based on [15]. Contrarily to our case, in the referenced work, the topological study is done on a 2-dimensional photonic crystal, which is a periodic structure. However, we adapted it for our case by changing some key aspects which are explained below. First of all, we perform a change of variables in 2.13:

$$\mathcal{C}_{gap} = \int_{-1/2}^{1/2} \int_{-1/2}^{1/2} d\beta_1 d\beta_2 \int_{0}^{\infty} d\xi g\left(\xi, \beta_1, \beta_2\right), \tag{2.14}$$

where we use coordinates $\omega = \omega'_{gap} + i\xi$ and $\mathbf{k} = \beta_1 \mathbf{b}_1 + \beta_2 \mathbf{b}_2$, where $\mathbf{b}_j$ are the reciprocal lattice primitive vectors of the photonic crystal and $-1/2 < \beta_j < 1/2 \quad (j = \{1, 2\})$ and the integrand function $g\left(\xi, \beta_1, \beta_2\right)$ is:

$$\begin{aligned} g\left(\xi, \beta_1, \beta_2\right) = \frac{i}{(2\pi)^2} |\mathbf{b}_1 \times \mathbf{b}_2| \Big[& Tr\{\partial_1 \hat{L}_{\mathbf{k}} \cdot \mathcal{G}_{\mathbf{k}} \cdot \partial_2 \hat{L}_{\mathbf{k}} \cdot \mathcal{G}^2_{\mathbf{k}}\}|_{\omega=\omega'_{gap}+i\xi, \mathbf{k}=\beta_1\mathbf{b}_1+\beta_2\mathbf{b}_2} \\ & + Tr\{\partial_1 \hat{L}_{\mathbf{k}} \cdot \mathcal{G}_{\mathbf{k}} \cdot \partial_2 \hat{L}_{\mathbf{k}} \cdot \mathcal{G}^2_{\mathbf{k}}\}|_{\omega=\omega'_{gap}-i\xi, \mathbf{k}=\beta_1\mathbf{b}_1+\beta_2\mathbf{b}_2} \Big] \end{aligned} \tag{2.15}$$

For practical reasons, the upper-limit of the integral in ξ is truncated and so we change ∞ to ξ_{max}. Typically, g decays exponentially fast with ξ so ξ_{max} is not required to have a large value, as we will see in section 4.3. Finally, the numerical integrals in ξ, β_1 and β_2 are done using the trapezoidal rule or the Simpson rule. The integration in β_i is over N_i subintervals with $i = \{1, 2\}$, so the integral over the wave vector space is done over $N_1 \times N_2$ subintervals. For simplicity we have $N_1 = N_2 = N$. The integration over the complex frequencies is done over N_w subintervals.

The photonic crystal in the reference has a honeycomb lattice, with lattice constant a and its direct lattice primitive vectors are taken as:

$$\mathbf{a}_1 = \frac{a}{2}\left(3\hat{\mathbf{x}} - \sqrt{3}\hat{\mathbf{y}}\right), \quad \mathbf{a}_2 = \frac{a}{2}\left(3\hat{\mathbf{x}} + \sqrt{3}\hat{\mathbf{y}}\right). \tag{2.16}$$

The first modification comes from the fact that since we will be dealing with homogeneous media, the integrals over the wave vector domain BZ do not require a specific direction, as is the case with an inhomogeneous structure. Therefore, we changed these vectors to simply point along the $\hat{\mathbf{x}}$ and $\hat{\mathbf{y}}$ directions.

$$\mathbf{a}_1 = \frac{a}{2}\left(\hat{\mathbf{x}}\right), \quad \mathbf{a}_2 = \frac{a}{2}\left(\hat{\mathbf{y}}\right) \tag{2.17}$$

The second modification was done to the constitutive parameters of the components in the unit cell. The photonic crystal is formed by two sub-lattices of cylindrical rods embedded in a background of air. We changed the constitutive parameters of each lattice and of the background itself by forcing them to be the same, and by doing this we substituted the inhomogeneous unit cell with a homogeneous one. With this alteration the medium is effectively a continuum.

Finally, in the article, a plane wave expansion was performed due to the periodic nature of the photonic crystal, and so the authors have an additional plane wave representation of the operator $\hat{L}_{\mathbf{k}}$. We have no need to perform this expansion since we will not topologically characterize a periodic structure. As we will see chapter in 4, with this implementation, we can have numerical results with extremely small absolute errors.

2.2.2 Operator $\hat{L}_{\mathbf{k}}$

Here we show an example of the derivation of the operator $\hat{L}$ from which $\hat{L}_{\mathbf{k}}$ is obtained. In this thesis we have characterized the topology of the magnetized plasma in 3D. This topological study includes both local and non-local models for this medium, as will be shown in chapter 4. Thus, the $\hat{L}$ operator will only be derived for these models. Here we introduce a general method to derive this operator which is described in [17] and we consider a local and lossless model of a magnetized plasma, as a first instance. This medium will be studied in section 3.2, so we will not elaborate much on its properties in this section.

We start with Maxwell's equations in time domain, for propagation in free space ($\partial_t \equiv \frac{\partial}{\partial_t}$):

$$\begin{aligned} -i\nabla \times \mathbf{E} &= i\mu_0 \partial_t \mathbf{H}, \\ i(\nabla \times \mathbf{H} - \mathbf{j}) &= i\epsilon_0 \partial_t \mathbf{E}, \end{aligned} \tag{2.18}$$

where μ_0 and ϵ_0 are the vacuum's permeability and permittivity, respectively. We then consider the continuity equation given by:

$$\partial_t \rho + \nabla \cdot \mathbf{j} = 0 \tag{2.19}$$

The current $\mathbf{j}$ and charge ρ densities model the response of the dispersive electric gyrotropic material. Making use of Newton's second law of motion plus Lorentz's Force law, one can derive the transport equation for a free electron gas biased with a static magnetic field ($\mathbf{B}_0 = B_0 \hat{z}$):

$$\partial_t \mathbf{j} = \epsilon \omega_p^2 \mathbf{E} + \frac{q}{m} \mathbf{j} \times \mathbf{B}_0, \tag{2.20}$$

where $q = -e$ is the charge of an electron with opposite sign and m is its effective mass. Equations (2.18)-(2.20) can be rewritten as a Schrödinger-type equation:

$$\hat{L} \cdot \mathbf{Q} = \frac{1}{c} i \partial_t \mathbf{Q} \tag{2.21}$$

The state vector $\mathbf{Q}$ is given by $\mathbf{Q} = \begin{bmatrix} E_x & E_y & E_z & \tilde{H}_x & \tilde{H}_y & \tilde{H}_z & \tilde{j}_x & \tilde{j}_y & \tilde{j}_z & \tilde{\rho} \end{bmatrix}^T$, with "T" being the transpose operator. We introduce the normalized magnetic field, current and charge density: $\tilde{\mathbf{H}} = \eta_0 \mathbf{H}$, $\tilde{\mathbf{j}} = \eta_0 \mathbf{j}$, $\tilde{\rho} = \eta_0 c \rho$, with η_0 being the vacuum wave impedance and c the speed of light.

Since we are interested in the 3-dimensional case of the continuous magnetized plasma, we assume a spatial and time variation of the state vector of the type $e^{i\mathbf{k}\cdot\mathbf{r}} e^{-i\omega t}$, with wave vector $\mathbf{k} = k_x \hat{x} + k_y \hat{y} + k_z \hat{z}$. We are also interested in analysing the dispersion of all light modes in this medium, thus we assume the propagating superposition of every polarization possible: $\mathbf{E} = E_x \hat{x} + E_y \hat{y} + E_z \hat{z}$, $\mathbf{H} = H_x \hat{x} + H_y \hat{y} + H_z \hat{z}$ and $\mathbf{j} = j_x \hat{x} + j_y \hat{y} + j_z \hat{z}$ which justifies the dimension of the state vector written above.

By applying the curl operator to the electric and magnetic fields described above, we get ($\partial_i \equiv \frac{\partial}{\partial_i}, i =$

$\{x, y, z\}$):

$$\begin{aligned} \nabla \times \mathbf{E} &= (\partial_y E_z - \partial_z E_y)\hat{x} - (\partial_x E_z - \partial_z E_x)\hat{y} + (\partial_x E_y - \partial_y E_x)\hat{z} \\ \nabla \times \mathbf{H} &= (\partial_y H_z - \partial_z H_y)\hat{x} - (\partial_x H_z - \partial_z H_x)\hat{y} + (\partial_x H_y - \partial_y H_x)\hat{z} \end{aligned} \tag{2.22}$$

Additionally, the cross product between the current density vector and the bias magnetic field renders:

$$\mathbf{j} \times \mathbf{B}_0 = j_y B_0 \hat{x} - j_x B_0 \hat{y} \tag{2.23}$$

By manipulating equations (2.18)-(2.20), inserting the previous results, taking into account that $c\mu_0 = \eta_0$ and that the cyclotron frequency is defined as $\omega_c = -qB_0/m$, we get:

$$\begin{aligned} -i \begin{bmatrix} \partial_y E_z - \partial_z E_y \\ \partial_z E_x - \partial_x E_z \\ \partial_x E_y - \partial_y E_x \end{bmatrix} &= i\frac{1}{c}\eta_0 \partial_t \begin{bmatrix} H_x \\ H_y \\ H_z \end{bmatrix} \\ \eta_0 i \left(\begin{bmatrix} \partial_y H_z - \partial_z H_y \\ \partial_z H_x - \partial_x H_z \\ \partial_x H_y - \partial_y H_x \end{bmatrix} - \begin{bmatrix} j_x \\ j_y \\ j_z \end{bmatrix} \right) &= i\frac{1}{c}\partial_t \begin{bmatrix} E_x \\ E_y \\ E_z \end{bmatrix} \\ -i\eta_0(\partial_x j_x + \partial_y j_y + \partial_z j_z) &= i\frac{1}{c}c\eta_0 \partial_t \rho \\ i\frac{\omega_p^2}{c^2} \begin{bmatrix} E_x \\ E_y \\ E_z \end{bmatrix} + i\eta_0 \frac{\omega_c}{c} \begin{bmatrix} -j_y \\ j_x \\ 0 \end{bmatrix} &= i\frac{1}{c}\eta_0 \partial_t \begin{bmatrix} j_x \\ j_y \\ j_z \end{bmatrix} \end{aligned} \tag{2.24}$$

Now, we only need to associate the rows of the operator with the state vector components present on the right side of the system of equations in (2.24) and its columns with the components present on the left side. The entries are simply the leftover factors multiplied with the state vector components so as to maintain the same structure of equation (2.21). Following this algorithm, we acquire the $\hat{L}$ operator:

$$\hat{L}(-i\nabla) = \begin{pmatrix} 0 & 0 & 0 & 0 & -i\partial_z & i\partial_y & -i & 0 & 0 & 0 \\ 0 & 0 & 0 & i\partial_z & 0 & -i\partial_x & 0 & -i & 0 & 0 \\ 0 & 0 & 0 & -i\partial_y & i\partial_x & 0 & 0 & 0 & -i & 0 \\ 0 & i\partial_z & -i\partial_y & 0 & 0 & 0 & 0 & 0 & 0 & 0 \\ -i\partial_z & 0 & i\partial_x & 0 & 0 & 0 & 0 & 0 & 0 & 0 \\ i\partial_y & -i\partial_x & 0 & 0 & 0 & 0 & 0 & 0 & 0 & 0 \\ i\frac{\omega_p^2}{c^2} & 0 & 0 & 0 & 0 & 0 & 0 & -i\frac{\omega_c}{c} & 0 & 0 \\ 0 & i\frac{\omega_p^2}{c^2} & 0 & 0 & 0 & 0 & i\frac{\omega_c}{c} & 0 & 0 & 0 \\ 0 & 0 & i\frac{\omega_p^2}{c^2} & 0 & 0 & 0 & 0 & 0 & 0 & 0 \\ 0 & 0 & 0 & 0 & 0 & 0 & -i\partial_x & -i\partial_y & -i\partial_z & 0 \end{pmatrix} \tag{2.25}$$

The operator $\hat{L}_{\mathbf{k}}$ from equation 2.12 can be obtained by substituting the spatial derivatives in 2.25 with the corresponding wave vector components $\frac{\partial}{\partial j} \leftrightarrow ik_j$, $j = \{x, y, z\}$.

3

Dispersion and Weyl Points

Contents

3.1 Helical Metamaterial 18

3.2 Magnetized Plasma 26

In this chapter, we will analyse the dispersion relations of the two main photonic systems under study which are the helical metamaterial and the magnetized plasma. In addition, we will present how the Weyl points emerge and what are the physical properties they possess.

3.1 Helical Metamaterial

The first structure under study is a metamaterial consisting of an array of infinitely long wires shaped like elliptical helices, made from perfectly electrical conductors (PEC) and embedded in air. Its physical realization exhibits type-II Weyl points due to its nonlocal response, as it will be shown. Its geometry can be visualized in figure 3.1, where a is the lattice constant of the square unit cell where one helix is positioned, $a_z = |p|$ is the pitch of the helix (we consider that all helices have the same handedness), ρ_x and ρ_y are the semi-major axes lengths in the $\hat{\mathbf{x}}$ and $\hat{\mathbf{y}}$ directions, respectively, and finally r_w is the wire radius.

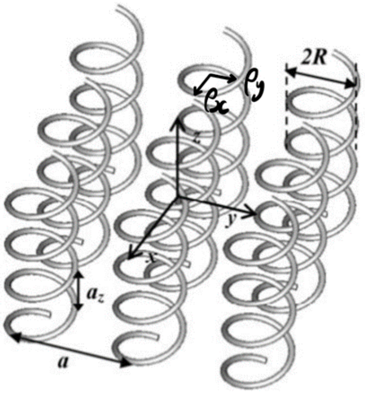

Figure 3.1: Helical metamaterial - geometry and orientation. Picture taken from [4]

Metamaterials can be regarded as continuous media if the inclusions that constitute the unit cell are electrically small, i.e. their dimension is much smaller than the wavelength of the electromagnetic wave in the specific direction of propagation. Take our structure for example. If a wave is travelling along the $\hat{\mathbf{z}}$ direction, then its lattice constant a_z given by the pitch of the helix should be considerably smaller than the wavelength. In this situation they can be described by effective constitutive parameters which correspond to a homogenized model.

Before we analyse the dispersion of electromagnetic waves in a possible physical realization of this metamaterial, we will focus on the class of materials where the homogenized model of the helical metamaterial belongs to.

3.1.1 Bianisotropic Model

We start with a bianisotropic homogeneous medium that possesses no spatial dispersion. The bianisotropy is due to chiral coupling (γ) between electric and magnetic fields and because the components of the permittivity and permeability tensors are all different. This type of media is anisotropic and chiral and it is described by the following constitutive relations:

$$\begin{pmatrix} \mathbf{D} \\ \mathbf{B} \end{pmatrix} = \begin{pmatrix} \overline{\epsilon} & i\sqrt{\epsilon_0\mu_0}\overline{\gamma} \\ -i\sqrt{\epsilon_0\mu_0}\overline{\gamma} & \overline{\mu} \end{pmatrix} \begin{pmatrix} \mathbf{E} \\ \mathbf{H} \end{pmatrix} \tag{3.1}$$

where the only nonvanishing component of $\overline{\gamma}$ is $\gamma_{zz} = \gamma$ and the permittivity and permeability tensors are as follows [20]:

$$\frac{\overline{\epsilon}}{\epsilon_0} = \begin{bmatrix} \epsilon_x & 0 & 0 \\ 0 & \epsilon_y & 0 \\ 0 & 0 & \epsilon_z \end{bmatrix} \tag{3.2}$$

$$\epsilon_z = 1 - \frac{\omega_p^2}{\omega^2} \tag{3.3}$$

$$\frac{\overline{\mu}}{\mu_0} = \begin{bmatrix} \mu_t & 0 & 0 \\ 0 & \mu_t & 0 \\ 0 & 0 & \mu_z \end{bmatrix} \tag{3.4}$$

As a first approximation, we consider ϵ_z to be the only dispersive constitutive parameter. It is characterized by Drude's dispersion and ω_p is a resonance frequency, also known as plasma frequency. This parameter is related to the geometry of the metamaterial as will be shown.

By applying the method described in section 2.1, the complete dispersion relation for this class of media is derived:

$$det \begin{bmatrix} \epsilon_x \left(\frac{\omega}{c}\right)^2 - \frac{k_y^2}{\mu_z} - \frac{k_z^2}{\mu_t} & \frac{k_x k_y}{\mu_z} & \frac{k_x k_z}{\mu_t} + i\frac{k_y \gamma_{zz}}{\mu_z}\left(\frac{\omega}{c}\right) \\ \frac{k_x k_y}{\mu_z} & \epsilon_y \left(\frac{\omega}{c}\right)^2 - \frac{k_x^2}{\mu_z} - \frac{k_z^2}{\mu_t} & \frac{k_y k_z}{\mu_t} - i\frac{k_x \gamma_{zz}}{\mu_z}\left(\frac{\omega}{c}\right) \\ \frac{k_x k_z}{\mu_t} - i\frac{k_y \gamma_{zz}}{\mu_z}\left(\frac{\omega}{c}\right) & \frac{k_y k_z}{\mu_t} + i\frac{k_x \gamma_{zz}}{\mu_z}\left(\frac{\omega}{c}\right) & \left(\epsilon_z - \frac{\gamma_{zz}^2}{\mu_z}\right)\left(\frac{\omega}{c}\right)^2 - \frac{k_x^2+k_y^2}{\mu_t} \end{bmatrix} = 0 \tag{3.5}$$

As we will see, the Weyl points arise along the k_z axis in the wave vector space, so we will focus mainly on propagation along the $\hat{\mathbf{z}}$ direction. The system supports three propagating modes, two of them transverse and one longitudinal. The transverse modes' dispersion relations are given by

$$\omega = \pm c k_z/\sqrt{\mu_t \epsilon_x}, \qquad \omega = \pm c k_z/\sqrt{\mu_t \epsilon_y}, \tag{3.6}$$

and so they are only degenerate when $\epsilon_x = \epsilon_y$. The longitudinal mode's dispersion relation is given by the solution to the equation $\epsilon_z - \gamma^2/\mu_z = 0$. It is a flat mode whose frequency is fixed at

$$\omega = \pm\omega_p/\sqrt{1 - \frac{\gamma^2}{\mu_z}} = \pm\omega_p', \tag{3.7}$$

independently of k_z.

The Weyl points in this system arise as crossings between this flat longitudinal mode and the transverse modes. They have been shown to be indeed Weyl crossings [20], because they are twofold degenerate (not three) due to the anisotropy of the permittivity in the $\hat{\mathbf{x}}$ and $\hat{\mathbf{y}}$ directions, and because they are linear in all directions due to the chiral coupling. Without the chiral coupling, the dispersion in the $\hat{\mathbf{y}}$ direction is quadratic.

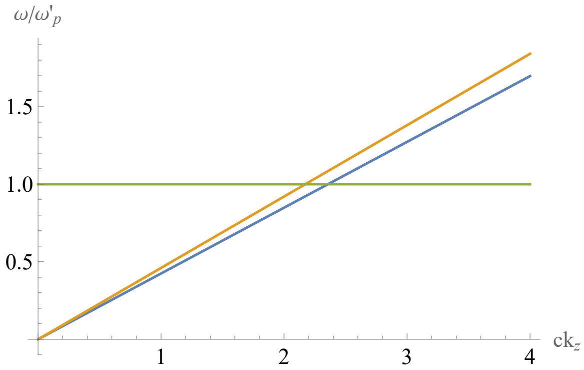

Figure 3.2: Dispersion along the k_z axis. Crossings between longitudinal mode (green) and transverse modes (blue and yellow) are Weyl points. The parameters used here were $\omega_p = 1, \epsilon_x = 2, \epsilon_y = 1.7, \mu_t = 1, \mu_z = 1, \gamma = 0.8$.

The Weyl points displayed in figure 3.2 are at the boundary separating type-I and type-II. To achieve either one, nonlocality must be introduced. Nonlocality or spatial dispersion occurs when a medium's constitutive parameters depend on the wave vector component of the propagating electromagnetic wave. Wire metamaterials are known to exhibit this nonlocal effect [29], hence we will now consider a different ϵ_z [20] that models spatial dispersion:

$$\epsilon_z = 1 - \frac{\omega_p'^2}{\omega^2} + \frac{\gamma^2}{\mu_z} + \alpha k_z^2 \tag{3.8}$$

The nonlocality affects the longitudinal mode's dispersion by introducing a curvature or concavity that either tilts it up or down. The alpha parameter controls this tilt and thus the type of Weyl point generated in the crossing. Recalling that this mode's dispersion is the solution to the equation $\epsilon_z - \gamma^2/\mu_z = 0$:

$$\omega = \pm \frac{\omega_p'}{\sqrt{1 + \alpha k_z^2}} \tag{3.9}$$

By analysing the second derivative of equation (3.9) with respect to the wave vector, it can be seen that it is positive for $\alpha < 0$ and negative for $\alpha > 0$, which means that with the first condition we have an upwards concavity and a downward concavity for the second one. Additionally, for $\alpha < 0$, the magnitude of this parameter cannot be too large due to the possibility of the longitudinal mode diverging thus precluding a crossing:

$$\alpha k_z^2 > -1 \Leftrightarrow k_z^2 > -1/\alpha \Rightarrow -\sqrt{-1/\alpha} < k_z < \sqrt{-1/\alpha} \tag{3.10}$$

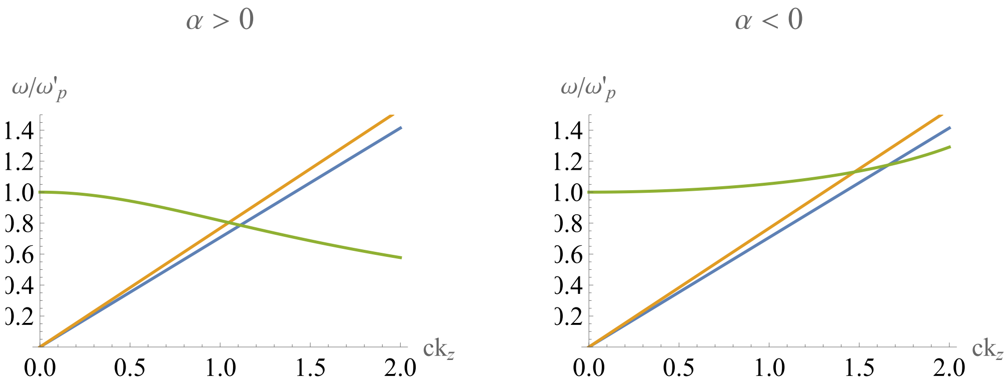

Figure 3.3: Dispersion along the k_z axis with a nonlocal ϵ_z. The parameters used on both plots were $\omega_p' = 1, \epsilon_x = 2, \epsilon_y = 1.7, \mu_t = 1, \mu_z = 1$. For the plot on the left: $\alpha = 0.5, \gamma = 1$ and for the plot on the right: $\alpha = -0.1, \gamma = 0.71$.

Figure 3.3 shows the effect of a positive and a negative alpha parameter on the concavity of the longitudinal mode. Since in the plots of this figure there are two degeneracies, we need to distinguish them. We will denominate the crossing between the yellow transverse mode and the green longitudinal mode as the first or inner Weyl point and the one between the blue and green modes as the second or outer Weyl point. By plotting the dispersion curves around one of the Weyl crossings, for example the second one, the conclusion can be derived that for $\alpha > 0$, the equifrequency curves are elliptical, signifying that it is type-I. On the other hand, for $\alpha < 0$, the equifrequency curves become hyperbolic, hence it becomes type-II. It is to be noted that the plots of the dispersion surfaces in figures 3.4 and 3.5 always display elliptical isofrequency curves, for the pair of wave vector components k_x and k_y, since there is no shift in k_z.

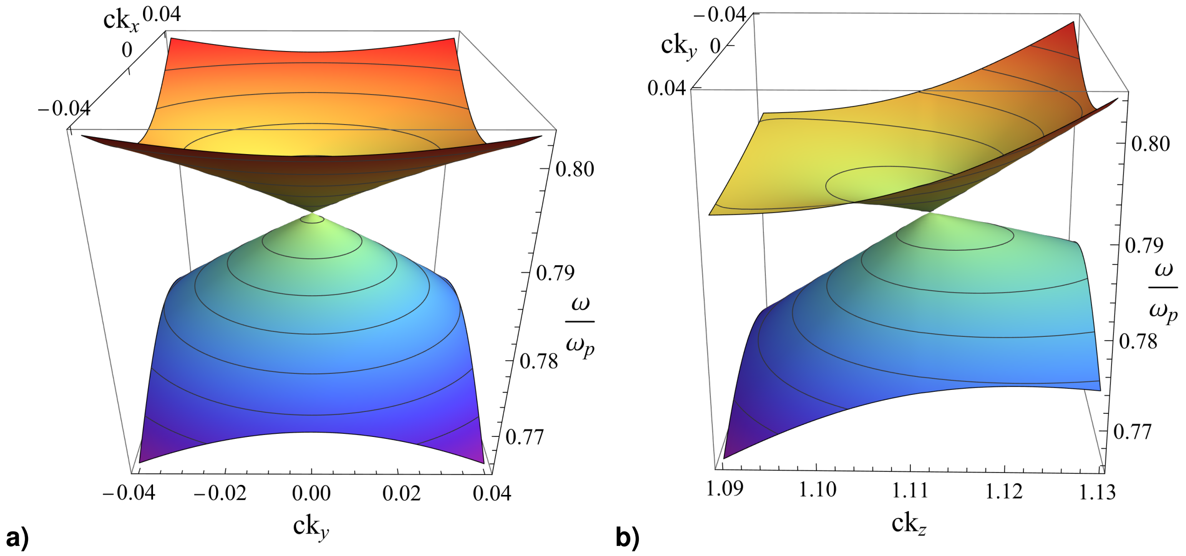

Figure 3.4: Dispersion around second Weyl point with $\alpha > 0$: **a)** in $\hat{x}$ and $\hat{y}$; **b)** in $\hat{z}$ and $\hat{y}$. The parameters used here were $\alpha = 0.5, \gamma = 1, \omega_p' = 1, \epsilon_x = 2, \epsilon_y = 1.7, \mu_t = 1, \mu_z = 1$.

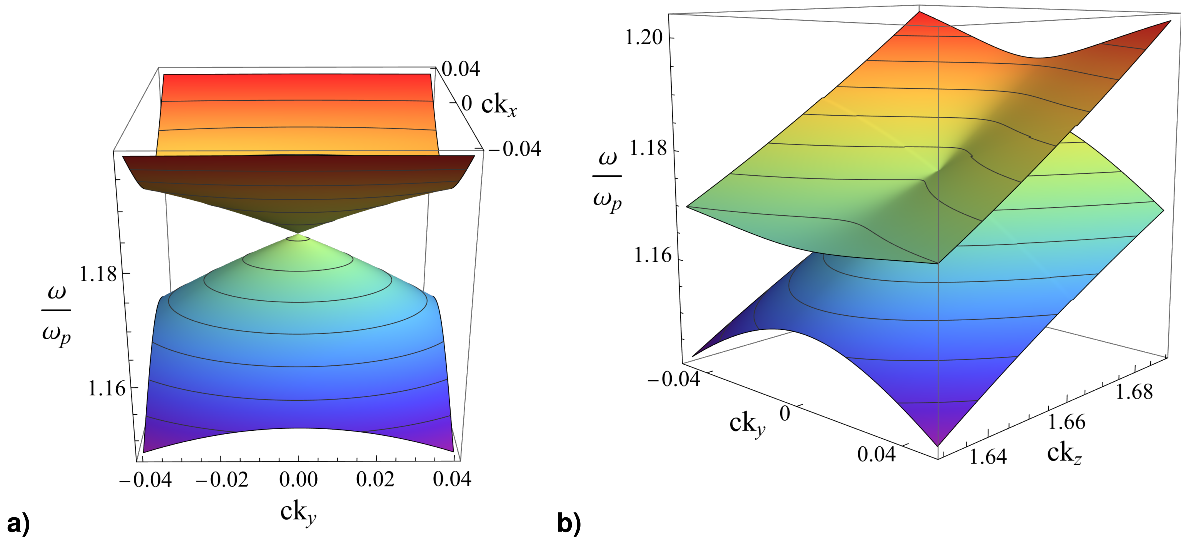

Figure 3.5: Dispersion around second Weyl point with $\alpha < 0$: **a)** in $\hat{x}$ and $\hat{y}$; **b)** in $\hat{z}$ and $\hat{y}$. The parameters used here were $\alpha = -0.1, \gamma = 0.71, \omega_p' = 1, \epsilon_x = 2, \epsilon_y = 1.7, \mu_t = 1, \mu_z = 1$.

As we will see in the next section, for a physical realization of this metamaterial, it is only possible to obtain type-II Weyl points.

3.1.2 Weyl Crossings in the Homogenization Limit

In this section, we will provide the link between the nonlocal bianisotropic model described previously and the effective medium theory of this metamaterial that is described in [4] and expanded in [20] to include ellipticity. This homogenization provides significant information about the physical realization of this metamaterial, specifically about its geometry. For example, the fact that the constituent of this metamaterial's unit cell is an elliptical helix is the reason the values for ϵ_x and ϵ_y differ and consequently originate two non-degenerate transverse modes, for propagation along the k_z axis. There is also an effective chirality due to lack of inversion symmetry of the helix (broken inversion symmetry). Moreover, in the previous section we studied a simplified model where only ϵ_z was dispersive, but the effective parameters μ_z and γ of the helical metamaterial are also dispersive. Because of this, we cannot obtain analytical formulas for the modes. We can only calculate them numerically. From the effective parameter formulae, we have:

$$\epsilon_x = 1 + \frac{(\pi \rho_x)^2}{V_{cell} C_{11}}, \tag{3.11}$$

$$\epsilon_y = 1 + \frac{(\pi \rho_y)^2}{V_{cell} \tilde{C}_{11}}, \tag{3.12}$$

$$\epsilon_z = 1 - \frac{1}{\beta^2/\beta_{p1}^2 - k_z^2/\beta_{p2}^2} + \frac{\gamma^2}{\mu_z}, \tag{3.13}$$

$$\mu_z = \left(1 + \frac{\beta^2 A^2}{\beta^2/\beta_{p1}^2 - k_z^2/\beta_{p2}^2}\right)^{-1}, \tag{3.14}$$

$$\mu_z^{-1}\gamma = \frac{\beta A}{2\left(\beta^2/\beta_{p1}^2 - k_z^2/\beta_{p2}^2\right)}, \tag{3.15}$$

where $\beta = \omega/c$ is frequency normalized to speed of light in the vacuum, $A = \pi\rho_x\rho_y/p$, V_{cell} is the volume of the unit cell, C_{11}, $\tilde{C}_{11}$, β_{p1} and β_{p2} are positive real-valued frequency independent parameters that depend only on the unit cell's geometry and lattice constant. We approximate the middle term of ϵ_z as:

$$\frac{1}{\frac{\beta^2}{\beta_{p1}^2} - \frac{k_z^2}{\beta_{p2}^2}} = \frac{1}{\frac{\beta^2}{\beta_{p1}^2}\left(1 - \frac{\beta_{p1}^2}{\beta^2}\frac{k_z^2}{\beta_{p2}^2}\right)} \approx \frac{1}{\beta^2/\beta_{p1}^2}\left(1 + \frac{\beta_{p1}^2}{\beta^2}\frac{k_z^2}{\beta_{p2}^2}\right), \quad \frac{\beta_{p1}}{\beta_{p2}}\left|\frac{k_z}{\beta}\right| \ll 1 \tag{3.16}$$

This corresponds to expanding the same term in a geometric series, while only keeping the first two orders:

$$\frac{1}{1-x^2} = \sum_{k=0}^{\infty} x^{2k}, \quad |x| < 1, \tag{3.17}$$

We can now link the $\gamma_{zz} = \gamma$ component of the chirality tensor in equation (3.1) with the effective chiral component in (3.15) and μ_z in equation (3.4) with the effective permeability in (3.14). The nonlocal permittivity model in equation (3.8) is the effective permittivity ϵ_z in (3.13) with γ and μ_z given as well by equations (3.15) and (3.14), respectively. The leftover constants ω_p' and α are given by:

$$\begin{aligned} \omega_p' &= c\beta_{p1} \\ \alpha &= -\frac{\beta_{p1}^4}{\beta_{p2}^2\beta^4} \end{aligned} \tag{3.18}$$

With this, we show that the alpha parameter is indeed negative (and in this case also dispersive), and so we conclude that this metamaterial possesses hyperbolic or type-II Weyl points.

Finally, we obtain the dispersion bands of a physical realization of this metamaterial with the geometric parameters: $p = 0.2a$, $\rho_x = 0.2a$ $\rho_y = 0.1a$. This simulation is executed with the effective medium theory. Firstly, in figure 3.6, the band structure along the k_z axis is presented, where we can see the two Weyl crossings. Since the longitudinal mode (in green) tilts up, as expected due to the sign of the α parameter, the crossings are type-II Weyl points. The crossing between the green and yellow modes is the first Weyl point, and the crossing between the green and blue modes is the second one. Following, in figures 3.7, 3.8 and 3.9 we have the dispersion in the $\hat{\mathbf{x}}$, $\hat{\mathbf{y}}$ and diagonal directions from the second Weyl point. The dispersion in these three directions are linear, close to the crossing.

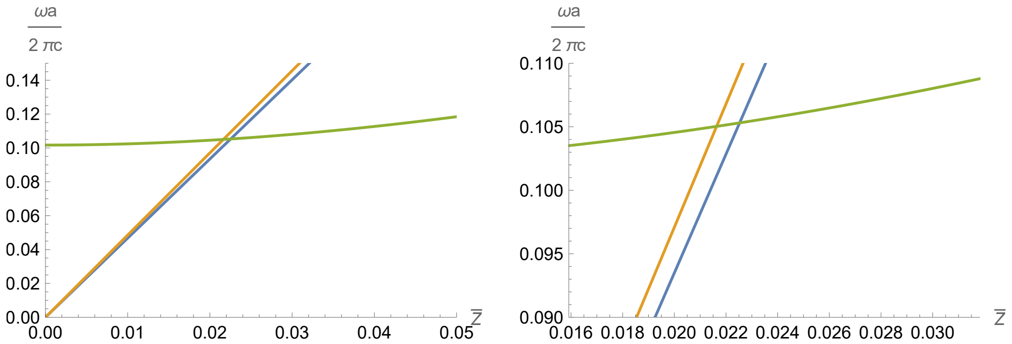

Figure 3.6: Dispersion along k_z axis. The longitudinal mode is in green and the transverse modes are in yellow and blue. The momentum axis' values are normalized as $\overline{Z} = k_z p/(2\pi)$.

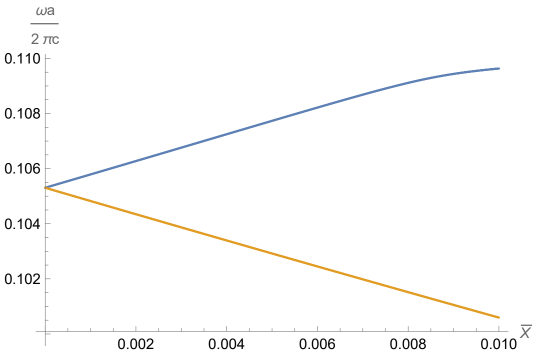

Figure 3.7: Dispersion in $\hat{x}$ direction, from Weyl point. The momentum axis' values are normalized as $\overline{X} = k_x a/(2\pi)$.

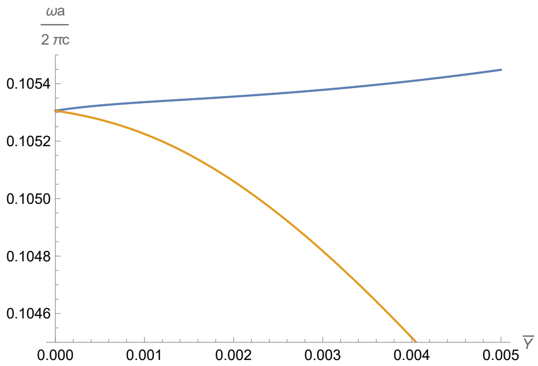

Figure 3.8: Dispersion in $\hat{y}$ direction, from Weyl point. The momentum axis' values are normalized as $\overline{Y} = k_y a/(2\pi)$.

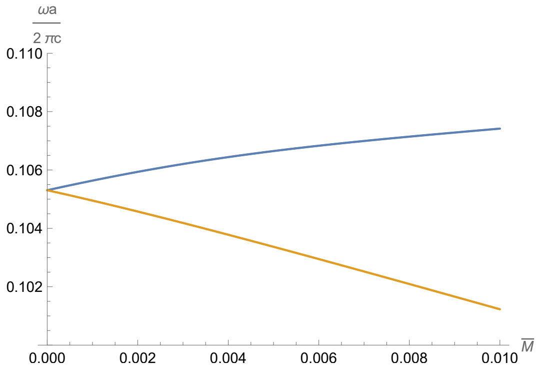

Figure 3.9: Dispersion in the diagonal direction formed between k_x and k_y, from Weyl point. The momentum axis' values are normalized as $\overline{M} = Ma/(2\pi)$ with $M^2 = k_x^2 + k_y^2$ (for $k_x = k_y$).

3.2 Magnetized Plasma

In this section we derive and analyse the dispersion relation for a magnetized plasma which is a continuous medium. This medium represents a naturally occurring plasma medium (metal or semiconductor) subjected to a magnetic field.

3.2.1 Local Model

We will derive the transport equation for a free electron medium, such as a metal. In a first instance, we consider the force of an electromagnetic field acting on a single electron. Starting with the Lorentz Force Law and Newton's Law (second law of motion), we have:

$$m\frac{d\mathbf{v}}{dt} = q(\mathbf{E} + \mathbf{v} \times \mathbf{B}), \tag{3.19}$$

where m is the effective mass of an electron, $\mathbf{v}$ is the instantaneous velocity vector, $q = -e = 1.6 \times 10^{-19}C$ is the charge of an electron with opposite sign, $\mathbf{E}$ is the electric field and $\mathbf{B}$ is the magnetic induction field. If $v = \|\mathbf{v}\|$ is much smaller than the speed of light c, then we can neglect the contribution of $\mathbf{B}$. Secondly, we average the equation over the whole set of electrons with volume density N. The collision frequency between these particles and the lattice will be neglected. This is acceptable when the wave frequency is much greater than the frequency of these collisions, so we are effectively dealing with a lossless medium. Taking into account that the electric current density of the ensemble is defined as $\mathbf{j} = Nq\mathbf{v}$, we get

$$\frac{d\mathbf{j}}{dt} = \epsilon_0 \omega_p^2 \mathbf{E}, \tag{3.20}$$

where ϵ_0 is the vacuum permittivity and ω_p is the plasma frequency which is defined as

$$\omega_p = \sqrt{\frac{Nq^2}{m\epsilon_0}}. \tag{3.21}$$

One can easily find the permittivity of this medium. If we consider monochromatic plane waves with time harmonic variation and take into account the relation between $\mathbf{j}$ and the polarizability vector $\mathbf{j} = \partial_t \mathbf{P}$, then we just need to solve equation (3.20) with respect to $\mathbf{j}$ and substitute in the constitutive equation $\mathbf{D} = \epsilon_0 \mathbf{E} + \mathbf{P} = \bar{\epsilon} \cdot \mathbf{E}$. Thus, we derive the isotropic permittivity expression for an electron plasma, which has Drude's dispersion:

$$\epsilon_p(\omega) = \epsilon_0 \left[1 - \frac{\omega_p^2}{\omega^2}\right] \tag{3.22}$$

The solutions for a plane wave propagating in a plasma medium show that for $\omega < \omega_p$, the wave vector k is purely imaginary, hence being an evanescent wave, and for $\omega > \omega_p$, the wave vector is real [28]. That means that lossless plasmas are entirely reflective for electromagnetic waves with frequency less than the plasma frequency, and entirely transmissive for frequencies above it [30].

When an external direct current (DC) or static magnetic field $\mathbf{B}_0$ is applied to the plasma medium, it becomes anisotropic. The field's effect is represented in the permittivity tensor through the cyclotron frequency. This is the angular frequency with which a free electron describes a circular cyclotron orbit, when it is under the influence of the magnetic field and is defined as:

$$\omega_c = -qB_0/m \tag{3.23}$$

Throughout this work, the application of $\mathbf{B}_0$ is assumed to be in the $\hat{z}$ direction with positive orientation. To derive the permittivity tensor for a magnetized plasma, we follow the same process as before, but now we consider $\mathbf{B}$ in (3.19) to be the sum of a harmonic magnetic field and the applied static field. The same approximation for $v \ll c$ is taken, but because $\mathbf{B}_0$ is constant and can have a large magnitude, the electrons are still significantly affected by this component. Hence, the transport equation that describes the dynamics of an electron mass biased with a static magnetic field is [17, 28]:

$$\frac{d\mathbf{j}}{dt} = \epsilon_0 \omega_p^2 \mathbf{E} + \frac{q}{m} \mathbf{j} \times \mathbf{B}_0 \tag{3.24}$$

The permittivity tensor is an antisymmetric matrix with a gyrotropic structure [2]:

$$\bar{\epsilon} = \begin{bmatrix} \epsilon_t & -i\epsilon_g & 0 \\ i\epsilon_g & \epsilon_t & 0 \\ 0 & 0 & \epsilon_z \end{bmatrix}, \tag{3.25}$$

where each entry is

$$\epsilon_t = \epsilon_0 \left[1 - \frac{\omega_p^2}{\omega^2 - \omega_c^2}\right], \tag{3.26}$$

$$\epsilon_g = \epsilon_0 \left[\frac{-\omega_c \omega_p^2}{\omega(\omega^2 - \omega_c^2)}\right], \tag{3.27}$$

$$\epsilon_z = \epsilon_0 \left[1 - \frac{\omega_p^2}{\omega^2}\right]. \tag{3.28}$$

Since (3.25) is not symmetric $\bar{\epsilon} \neq \bar{\epsilon}^T$, this medium has a nonreciprocal response. The application of the bias field also breaks time reversal symmetry. Because we are considering a lossless case, these two notions are equivalent [16]. Furthermore, we will consider a nonmagnetic response $\overline{\mu} = \mathbb{1}$ and trivial magnetoelectric coupling $\overline{\xi} = \overline{\zeta} = 0$. Since the system's material matrix does not depend on the wave vector then this is a local model. The $\hat{L}$ operator that describes wave propagation in this medium is the one in equation (2.25) derived in section 2.2.2.

Our next objective is to obtain the dispersion characteristics of the bulk modes. This is possible by simply deriving the wave equation from Maxwell's equations (without a source), assuming a harmonic variation of the type $e^{i(\mathbf{k}\cdot\mathbf{r}-\omega t)}$:

$$\mathbf{k}\times(\mathbf{k}\times\underline{\mathbf{E}})+\frac{\omega^2}{c^2}\bar{\epsilon}\cdot\underline{\mathbf{E}}=0 \tag{3.29}$$

The wave vector of the solution for the equation above satisfies the dispersion relation [31]

$$\left(\epsilon_t^2-\epsilon_g^2\right)\epsilon_z\frac{\omega^4}{c^4}-\left(\left[\epsilon_t\left(\epsilon_t+\epsilon_z\right)-\epsilon_g^2\right]k_t^2+2\epsilon_t\epsilon_z k_z^2\right)\frac{\omega^2}{c^2}+\left(\epsilon_t k_t^2+\epsilon_z k_z^2\right)\left(k_t^2+k_z^2\right)=0, \tag{3.30}$$

where $k_t=\|\mathbf{k_t}\|=\|k_x\hat{\mathbf{x}}+k_y\hat{\mathbf{y}}\|$, with subscript t representing wave vector components that are orthogonal to the static magnetic field.

As previously stated, the magnetized plasma presents photonic Weyl degeneracies, otherwise known as Weyl points. Due to the direction of $\mathbf{B}_0$, these appear along the k_z axis, i.e. only for wave vectors **k** $=(0,0,k_z)$. Along this axis there are straight horizontal bands at $\omega=\pm\omega_p$ which are longitudinal bulk plasmon modes that occur for $\epsilon_z=0$. The Weyl points arise as crossings between this plasmon mode and transverse modes and the location of these linear degeneracies in wave vector space is given by [24]:

$$k_z^{Weyl}=\pm\frac{\omega_p}{c}\sqrt{\frac{\omega_c}{\omega_c\pm\omega_p}} \tag{3.31}$$

By fixing the plasma frequency ω_p and varying the cyclotron frequency ω_c which corresponds to varying the magnitude of the static bias magnetic field, we vary the number of Weyl crossings:

- $\omega_c<\omega_p$: 1 pair of Weyl points in momentum space;
- $\omega_c>\omega_p$: 2 pairs of Weyl points in momentum space;

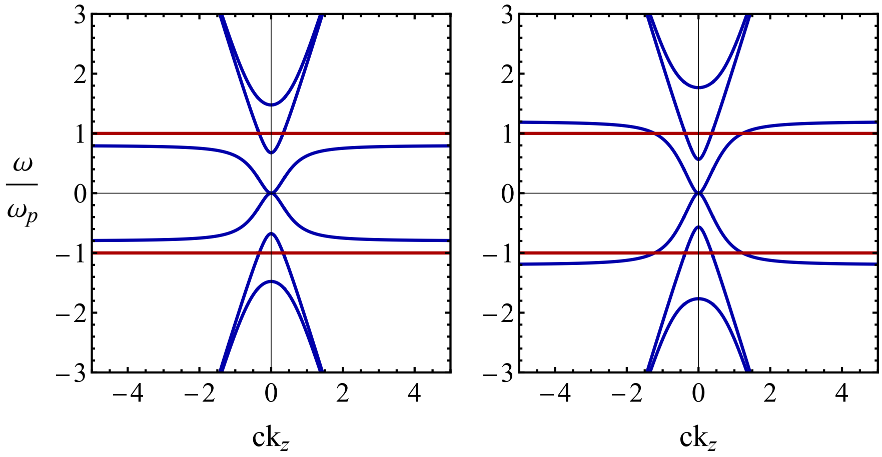

Figure 3.10: Dispersion characteristics in the k_z axis for $\omega_c=0.8\omega_p$ on the left, $\omega_c=1.2\omega_p$ on the right and $\omega_p=0.5c$ in both plots. The longitudinal mode is highlighted in red.

We will consider these two different regimes throughout this section. The dispersion diagrams for modes propagating in the direction of the applied static magnetic field are shown in figure 3.10, for both regimes. We can observe that the number of crossings between the longitudinal (in red) and the transverse (in blue) modes is indeed different between the two cases: while there are 4 crossings in the left panel, the right one shows 8. When $\omega_c = \omega_p$ the outer Weyl points go to infinity and for $\omega_c < \omega_p$ they are purely imaginary and so, in these conditions, only the inner Weyl points appear.

To visualize the point-like crossings properly, three-dimensional dispersion characteristics are shown in figures 3.11-3.12:

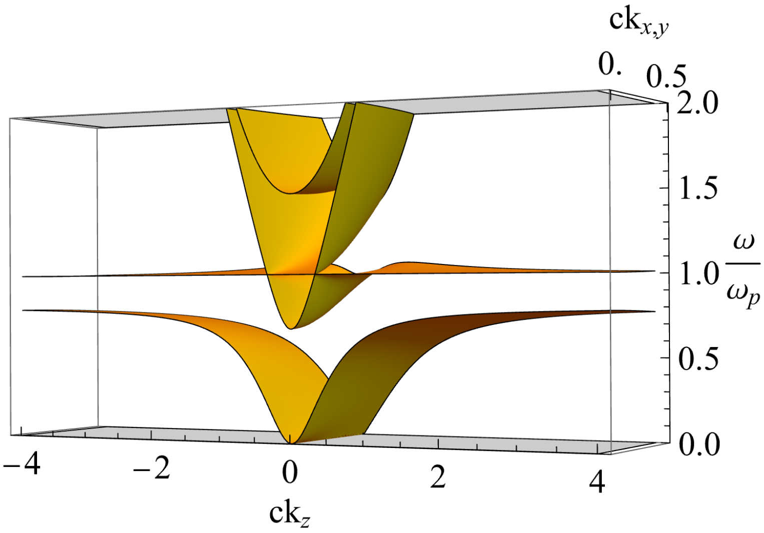

Figure 3.11: Three-dimensional dispersion showcasing two crossings. Parameters used here were for $\omega_c = 0.8\omega_p$ and $\omega_p = 0.5c$

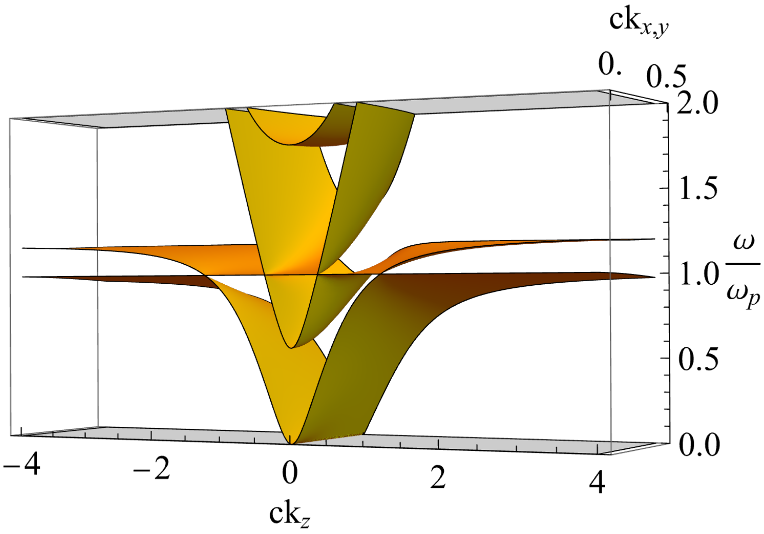

Figure 3.12: Three-dimensional dispersion showcasing four crossings. Parameters used here were for $\omega_c = 1.2\omega_p$ and $\omega_p = 0.5c$

For propagation in the xoy plane, hence for a wave vector **k** $= (k_x, ky, 0)$, the plane waves supported by the medium decouple into transverse electric (TE) waves ($E_z \neq 0$ and $H_z = 0$) and transverse magnetic (TM) waves ($H_z \neq 0$ and $E_z = 0$). The dispersion relations for these photonic modes are, respectively:

$$k^2 = \epsilon_z \left(\frac{\omega}{c}\right)^2, \quad \text{TE modes,} \tag{3.32}$$

$$k^2 = \epsilon_{ef} \left(\frac{\omega}{c}\right)^2 \Leftrightarrow k^2 = \frac{\epsilon_t^2 - \epsilon_g^2}{\epsilon_t} \left(\frac{\omega}{c}\right)^2, \quad \text{TM modes.} \tag{3.33}$$

By examining the dispersion relation of the whole system in (3.30), one can see that the dispersion characteristics have rotational symmetry for planes in wave vector space which are orthogonal to the k_z axis (xoy plane). This is why there is no difference in choosing k_y or k_x for dispersion analysis. In figure 3.13, one can see the TM modes' dispersion for the propagation in this plane for the two regimes:

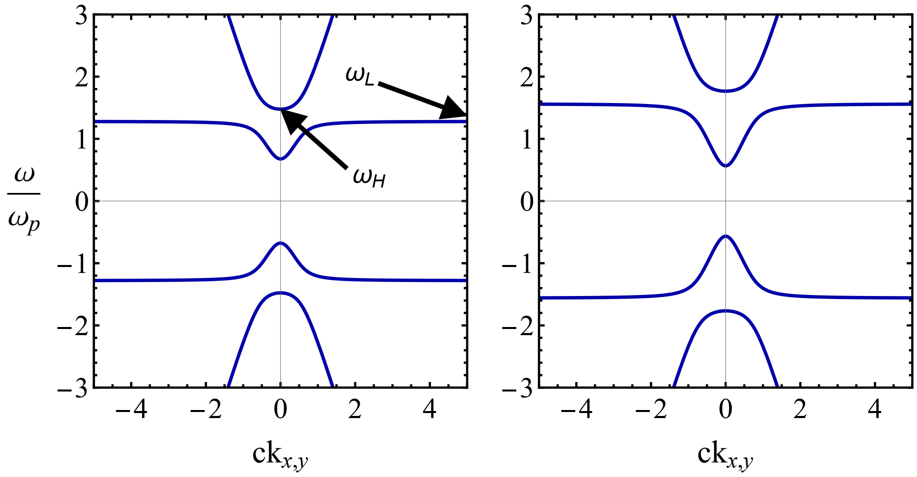

Figure 3.13: TM modes' dispersion in the xoy plane for $\omega_c = 0.8\omega_p$ on the left, $\omega_c = 1.2\omega_p$ on the right and $\omega_p = 0.5c$ in both plots.

Since we are interested in computing gap Chern numbers, here follows a study of the existence of a full band gap between the low and high-frequency bands, situated in the positive frequency half-plane. Having a closer look at the dispersion relation for the TM modes and using the explicit expressions of the constitutive parameters, the following equation and solutions are derived:

$$k^2 = \frac{1}{c^2} \frac{\omega^4 + \omega_p^4 - \omega^2(\omega_c^2 + 2\omega_p^2)}{\omega^2 - \omega_c^2 - \omega_p^2} \tag{3.34}$$

$$\omega_{TM} = \pm\sqrt{\frac{c^2k^2 + \omega_c^2 + 2\omega_p^2 \pm \sqrt{c^4k^4 - 2c^2k^2\omega_c^2 + \omega_c^4 + 4\omega_c^2\omega_p^2}}{2}} \tag{3.35}$$

Four solutions are derived, one for each observed branch in the plots of figure 3.13. Let us define

$\omega_{gap,1} = \omega_H - \omega_L$ as the function that measures the amplitude of the band gap under study. Expressions for ω_H and ω_L are given below:

$$\omega_H = \lim_{k\to 0} \sqrt{\frac{c^2k^2 + \omega_c^2 + 2\omega_p^2 + \sqrt{c^4k^4 - 2c^2k^2\omega_c^2 + \omega_c^4 + 4\omega_c^2\omega_p^2}}{2}} = \frac{\omega_c}{2} + \sqrt{\left(\frac{\omega_c}{2}\right)^2 + \omega_p^2} \tag{3.36}$$

$$\omega_L = \lim_{k\to \infty} \sqrt{\frac{c^2k^2 + \omega_c^2 + 2\omega_p^2 - \sqrt{c^4k^4 - 2c^2k^2\omega_c^2 + \omega_c^4 + 4\omega_c^2\omega_p^2}}{2}} = \sqrt{\omega_c^2 + \omega_p^2} \tag{3.37}$$

Finally, solving the inequality $\omega_{gap,1} > 0$, the conclusion is that for any positive real values of ω_c and ω_p, the band gap is always open. If we now consider the existence of a band gap between the low-frequency mode and the zero frequency $\omega = 0$, defining the amplitude as the solution to the inequality $\omega_{gap,2} > 0$, with

$$\begin{aligned}\omega_{gap,2} &= \lim_{k\to 0} \sqrt{\frac{c^2k^2 + \omega_c^2 + 2\omega_p^2 - \sqrt{c^4k^4 - 2c^2k^2\omega_c^2 + \omega_c^4 + 4\omega_c^2\omega_p^2}}{2}} \\ &= \sqrt{\frac{\omega_c^2 + 2\omega_p^2 - \sqrt{+\omega_c^4 + 4\omega_c^2\omega_p^2}}{2}},\end{aligned} \tag{3.38}$$

we derive the same conclusion. The results stand for the negative frequency branches since the solutions of equation (3.33) have reflection symmetry over both axes.

The story is different when the existence of both the TM and TE modes is considered, as one can perceive by looking at their dispersion characteristics simultaneously, in figure 3.14:

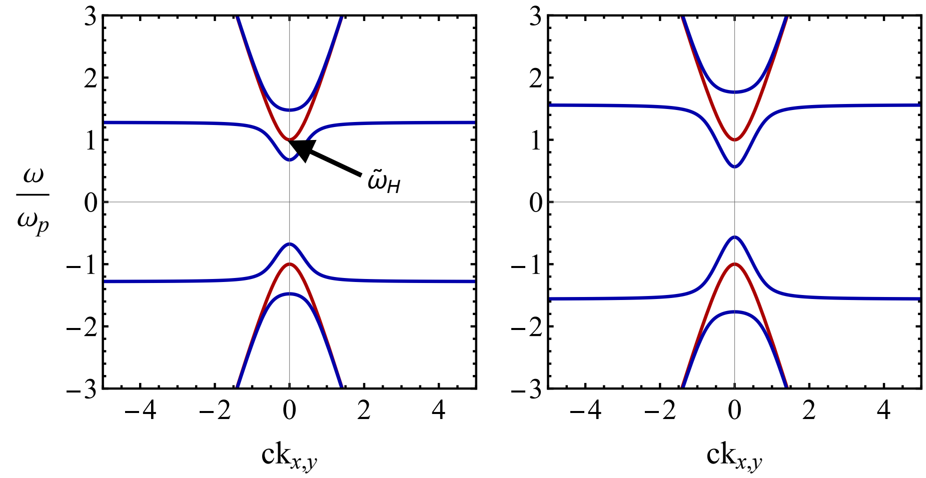

Figure 3.14: Dispersion of the TM modes in blue and TE modes in red in the xoy plane for $\omega_c = 0.8\omega_p$ on the left, $\omega_c = 1.2\omega_p$ on the right and $\omega_p = 0.5c$ in both plots.

The problem is now understanding if there could be a full band gap between the low-frequency TM band and the TE band (blue and red in figure 3.14, respectively). A similar analysis is conducted for this purpose, by firstly solving the dispersion equation (3.32) for the TE modes:

$$k^2 = \frac{\omega^2 - \omega_p^2}{c^2} \tag{3.39}$$

$$\omega_{TE} = \pm\sqrt{c^2k^2 + \omega_p^2} \tag{3.40}$$

If we define the new function for the amplitude of the "gap" in question as $\widetilde{\omega}_{gap,1} = \widetilde{\omega}_H - \omega_L$, with ω_L staying the same (3.37) and $\widetilde{\omega}_H$ as

$$\widetilde{\omega}_H = \lim_{k\to 0} \sqrt{c^2k^2 + \omega_p^2} = \sqrt{\omega_p^2} = \omega_p, \tag{3.41}$$

we can then solve the inequality $\widetilde{\omega}^1_{gap} > 0$ to see if it is possible to get a full band gap.

$$\widetilde{\omega}_{gap,1} > 0 \Leftrightarrow \sqrt{\omega_p^2} > \sqrt{\omega_c^2 + \omega_p^2} \Rightarrow \omega_p^2 > \omega_c^2 + \omega_p^2 \Leftrightarrow \omega_c^2 < 0 \tag{3.42}$$

There is no real valued ω_c that satisfies the inequality, thus there is no band gap between these two bands. This is a very relevant result for this work, since we can only apply the Green's function formalism to compute the gap Chern number for the low-frequency gap. It is to be noted that the TE modes also present reflection symmetry over both axes, and so there is no high-frequency band gap in the negative branches.

Weyl points are monopoles of Berry curvature and they always come in pairs, located at symmetric positions in momentum space, with opposite charges. This means that for each pair, there is always one source from which the field lines of the Berry curvature diverge and one sink to which the field lines converges. Since in this system these crossings arise along the k_z axis, we are aiming to "capture" this pseudo vector field, by selecting cross sections of the 3-dimensional dispersion characteristic that are orthogonal to this axis. Although our formalism does not consider the Berry curvature directly, it is equivalent to the traditional formalism in the sense that by calculating gap Chern numbers in band gaps situated in these cross sections, we compute the influence of the Berry flux. Furthermore, since the topological charge of the Weyl crossings is determined by the jump in the Berry flux along a straight line that joins the pair [7], by computing gap Chern numbers in orthogonal cross sections before and after one of these degeneracies, the difference of the gap Chern numbers quantifies this jump, and consequently its topological charge. This problem will be better illustrated in chapter 4, but now we know that we must analyse cross sections that are orthogonal to the k_z axis and investigate the existence of band gaps in the same ones.

In the xoy plane case, we have seen it is impossible to have a full band gap between the low-frequency TM mode and the TE mode. Now we will take cross sections (figures 3.15-3.16) of the dispersion along the k_z axis to see the behaviour of the bands graphically, in order to check if we can apply the Green's function formalism before and after the Weyl points. We consider the regime $\omega_c > \omega_p$ so both Weyl pairs are originated.

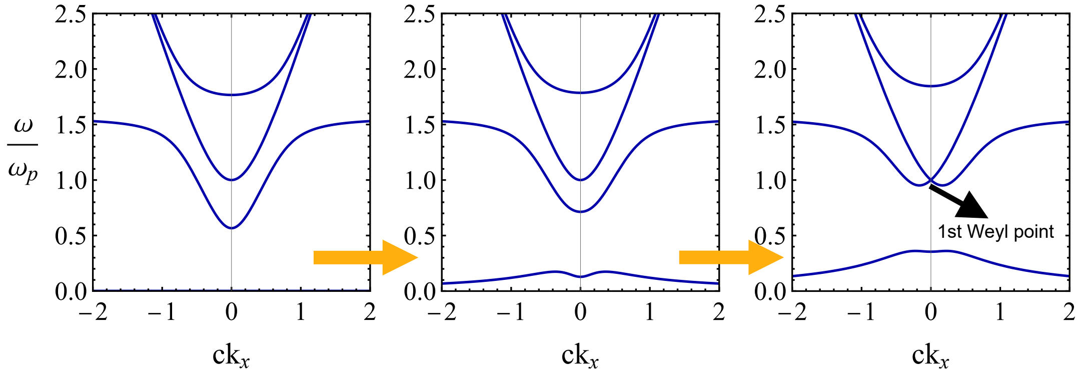

Figure 3.15: Varying k_z shows that there is no high-frequency band gap before the 1st Weyl point. From left to right: $k_z = 0$, $k_z = \frac{3}{4}W_1$ and $k_z = W_1$, with W_1 being the location of the 1st Weyl point in momentum space. The low-frequency band gap is present. The yellow arrows point in the orientation of increasing values in k_z. Parameters used here were $\omega_c = 1.2\omega_p$ and $\omega_p = 0.5c$

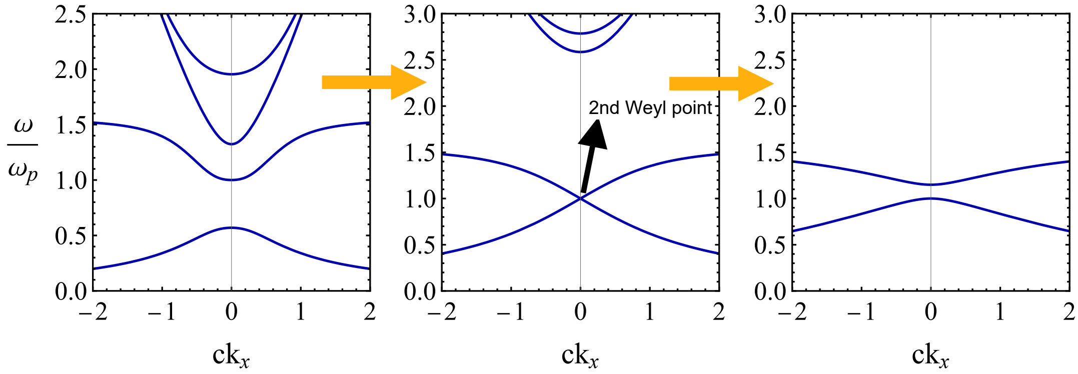

Figure 3.16: A full high-frequency band gap is observable only for a high value of k_z, after the 1st Weyl point. From left to right: $k_z = \frac{5}{4}W_1$, $k_z = W_2$ and $k_z = \frac{5}{4}W_2$, with W_1 and W_2 being the location of the 1st and 2nd Weyl points in momentum space. The low-frequency band gap is present before and after the 2nd Weyl point. The yellow arrows point in the orientation of increasing values in k_z. Parameters used here were $\omega_c = 1.2\omega_p$ and $\omega_p = 0.5c$

Regarding the first or inner Weyl point, we see that the bands that originate this crossing only possess a full band gap for a high enough k_z value, after the crossing itself. Before it, the bands display the same behaviour as in the xoy plane, the reason why there is no band gap. The case is different for the second or outer Weyl point. The bands that originate this crossing possess full band gaps at all cross sections situated before and after it.

To work around the issue of an absent band gap before the first Weyl point, we studied other models for the permittivity. A solution was achieved when shifting the plasma frequency as seen by the EM plane waves solely in the $\hat{\mathbf{z}}$ direction, and so we only change ϵ_z:

$$\frac{\epsilon_z}{\epsilon_0} = 1 - \frac{\omega_p'^2}{\omega^2}, \tag{3.43}$$

where $\omega_p' = \sqrt{K}\omega_p$ and K is a scalar. Considering that the only modes affected by this permittivity tensor component are the TE (3.32), for propagation in the xoy plane, we derive a new set of solutions for the dispersion characteristic:

$$k^2 = \frac{\omega^2 - \omega_p'^2}{c^2} \tag{3.44}$$

$$\omega_{TE} = \pm\sqrt{c^2k^2 + \omega_p'^2} \tag{3.45}$$

We study the possibility of a full band gap between this mode and the low-frequency TM mode, by redefining $\widetilde{\omega}^1_{gap} = \widetilde{\omega}_{H,K} - \omega_L$, with $\widetilde{\omega}_{H,K}$ as

$$\widetilde{\omega}_{H,K} = \lim_{k\to 0} \sqrt{c^2k^2 + \omega_p'^2} = \omega_p', \tag{3.46}$$

and so we need to find K that satisfies $\widetilde{\omega}^1_{gap} > 0$.

$$\widetilde{\omega}_{gap} > 0 \Leftrightarrow \sqrt{K\omega_p^2} > \sqrt{\omega_c^2 + \omega_p^2} \Rightarrow K\omega_p^2 > \omega_c^2 + \omega_p^2 \Leftrightarrow K > \frac{\omega_c^2}{\omega_p^2} + 1 \tag{3.47}$$

The value of $\widetilde{\omega}_{H,K}$ must also be smaller than ω_H. This is because the longitudinal mode appearing along the k_z axis also suffers a shift with this new model. In fact, this flat mode's frequency is given by $\omega = \omega_p'$ and so it intersects the xoy plane's TE mode at its lowest point, in the wave vector space origin $\mathbf{k} = (0,0,0)$. If the longitudinal mode intersects the higher frequency transverse mode, specifically at ω_H, it could potentially alter the topology of the medium, meaning that different Weyl crossings may be achieved, which is not our objective.

$$\sqrt{K\omega_p^2} < \frac{\omega_c}{2} + \sqrt{\left(\frac{\omega_c}{2}\right)^2 + \omega_p^2} \Rightarrow K < \frac{\omega_c^2}{2\omega_p^2} + \frac{\omega_c}{\omega_p^2}\sqrt{\left(\frac{\omega_c}{2}\right)^2 + \omega_p^2} + 1 \tag{3.48}$$

The constant must then be within an interval that depends only on the constitutive parameters ω_c and ω_p:

$$\frac{\omega_c^2}{\omega_p^2} + 1 < K < \frac{\omega_c^2}{2\omega_p^2} + \frac{\omega_c}{\omega_p^2}\sqrt{\left(\frac{\omega_c}{2}\right)^2 + \omega_p^2} + 1 \tag{3.49}$$

For example, if $\omega_c = 0.8\omega_p$, it is possible to guarantee a band gap between the TE mode and the low-frequency TM mode if K is in the range $[1.64, 2.18]$. If $\omega_c = 1.2\omega_p$, it must be in the range $[2.44, 3.11]$. The achieved band gaps are observable in figure 3.17:

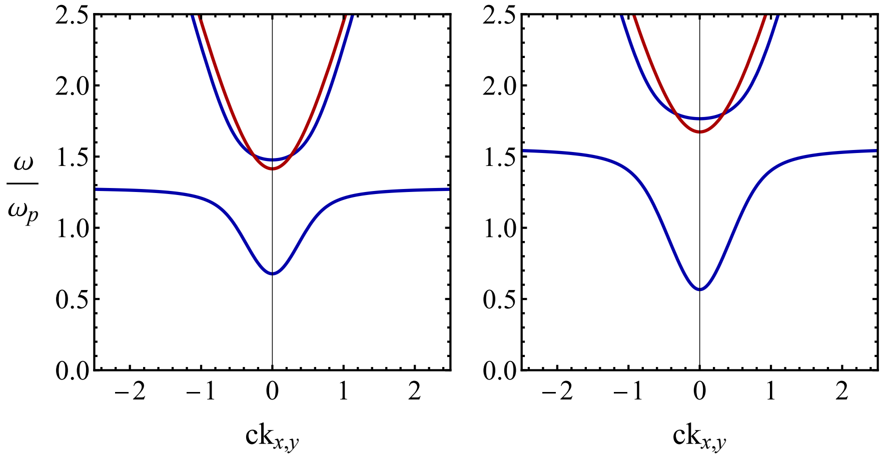

Figure 3.17: Dispersion in xoy plane ($k_z = 0$) with new ϵ_z. TM modes are in blue and TE mode is in red. Parameters used on the left were $\omega_c = 0.8\omega_p$ $\omega_p' = \sqrt{2}\omega_p$, $\omega_c = 1.2\omega_p$ $\omega_p' = \sqrt{2.8}\omega_p$ on the right and $\omega_p = 0.5c$ in both plots.

We can see that by shifting the TE band upwards it intersects the high-frequency TM band. This does not constitute a problem because the TE mode was shown to be topologically trivial [31]. This means that the Chern number of the high-frequency TM band before the intersection is equal to the Chern number of the set formed by the same band plus the intersecting TE band. However one crucial effect is noticed when looking at the dispersion in the k_z axis. For the regime $\omega_c < \omega_p$, the number of Weyl points is the same as with the original model, but in the regime $\omega_c > \omega_p$ the outer Weyl points no longer emerge in this system. This can be explained by analysing the low-frequency transverse modes propagating in the $\hat{\mathbf{z}}$ direction. When $k_z \to \infty$, the frequency of these modes will tend to a value $\omega \to \omega_c$ which, due to the plasma frequency shift, it is always smaller than ω_p'.

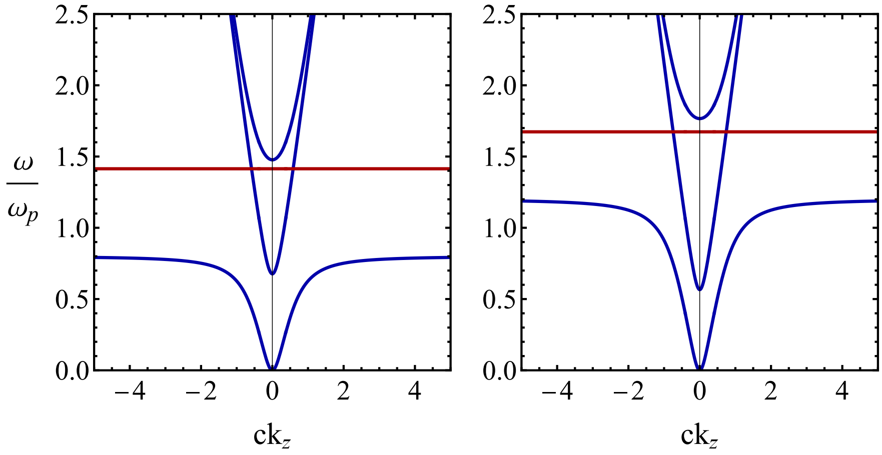

Figure 3.18: Dispersion in $\hat{z}$ direction with new ϵ_z. The longitudinal mode is in red. Parameters used on the left were $\omega_c = 0.8\omega_p$ $\omega_p' = \sqrt{2}\omega_p$, $\omega_c = 1.2\omega_p$ $\omega_p' = \sqrt{2.8}\omega_p$ on the right and $\omega_p = 0.5c$ in both plots.

Thus, this model only possesses one Weyl pair. Their location in momentum space is given by:

$$k_z^{Weyl} = \pm i\sqrt{\frac{\omega_p'(\omega_p^2 - \omega_c\omega_p' - \omega_p'^2)}{c^2(\omega_c + \omega_p')}} \tag{3.50}$$

The 3-dimensional dispersion can be observed in figure 3.19:

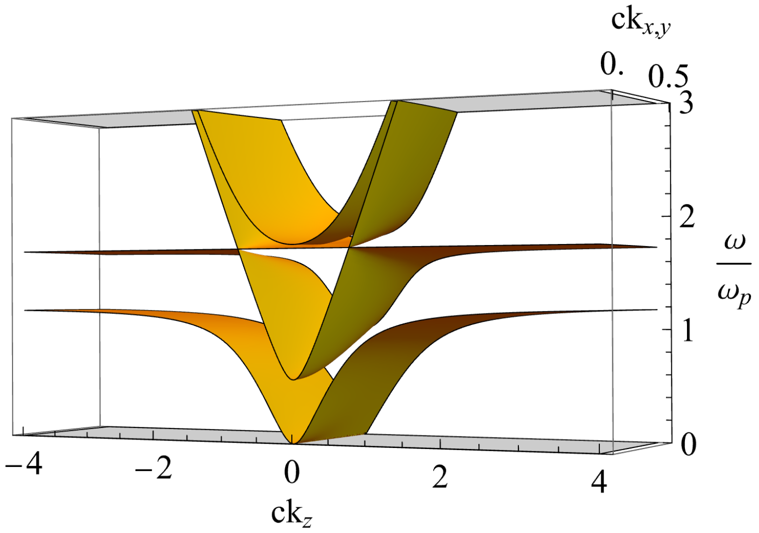

Figure 3.19: 3-dimensional dispersion with shifted plasma frequency in the $\hat{\mathbf{z}}$ direction. The parameters used here were $\omega_c = 1.2\omega_p$, $\omega_p' = \sqrt{3}\omega_p$ and $\omega_p = 0.5c$.

The $\hat{L}$ operator that describes this slightly different model is obtained by simply changing ω_p to ω_p' in the (9,3) component in the matrix of equation 2.25

$$\hat{L}(-i\nabla) = \begin{pmatrix} 0 & 0 & 0 & 0 & -i\partial_z & i\partial_y & -i & 0 & 0 & 0 \\ 0 & 0 & 0 & i\partial_z & 0 & -i\partial_x & 0 & -i & 0 & 0 \\ 0 & 0 & 0 & -i\partial_y & i\partial_x & 0 & 0 & 0 & -i & 0 \\ 0 & i\partial_z & -i\partial_y & 0 & 0 & 0 & 0 & 0 & 0 & 0 \\ -i\partial_z & 0 & i\partial_x & 0 & 0 & 0 & 0 & 0 & 0 & 0 \\ i\partial_y & -i\partial_x & 0 & 0 & 0 & 0 & 0 & 0 & 0 & 0 \\ i\frac{\omega_p^2}{c^2} & 0 & 0 & 0 & 0 & 0 & 0 & -i\frac{\omega_c}{c} & 0 & 0 \\ 0 & i\frac{\omega_p^2}{c^2} & 0 & 0 & 0 & 0 & i\frac{\omega_c}{c} & 0 & 0 & 0 \\ 0 & 0 & i\frac{\omega_p'^2}{c^2} & 0 & 0 & 0 & 0 & 0 & 0 & 0 \\ 0 & 0 & 0 & 0 & 0 & 0 & -i\partial_x & -i\partial_y & -i\partial_z & 0 \end{pmatrix} \tag{3.51}$$

It turns out that, as shown in the next chapter, this model does not always have well-defined topologies, i.e. the bands don't always have integer Chern numbers. In order to ensure well-defined topologies, we need to apply a regularization procedure which suppresses the nonreciprocal response of the material matrix for large wavelengths. For this purpose two solutions were explored and they are discussed in the following sections 3.2.2 and 3.2.3.

3.2.2 Hydrodynamic Model

The hydrodynamic or drift-diffusion model of a magnetized plasma is an extension of the system described in section 3.2.1, where the repulsive interactions between electrons are accounted for. To attain this model, one must include a factor on the right-hand side of equation 3.24 that describes the diffusion-type force contribution. That term is $-\beta^2\nabla\rho$, where ρ is the charge density and $\beta^2 = \langle v^2 \rangle = \frac{3}{5}v_F^2$ determines the strength of the diffusion, with v_F being the Fermi-velocity of the electrons. The minus sign indicates that the electrons feel a force "pushing" them away from the directions of high charge concentrated areas. Thus, the transport equation of the hydrodynamic model of a magnetized plasma is [2, 17]

$$\frac{d\mathbf{j}}{dt} = \epsilon_0\omega_p^2\mathbf{E} + \frac{q}{m}\mathbf{j}\times\mathbf{B}_0 - \beta^2\nabla\rho, \tag{3.52}$$

and if we wish to retrieve the local model, we just set β as zero.

By employing the method described in section 2.2.2, one can acquire the $\hat{L}$ operator that effectively models the propagation in this medium. Instead of using the transport equation (2.20) for this purpose, we substitute it with (3.52). We obtain:

$$\hat{L}(-i\nabla) = \begin{pmatrix} 0 & 0 & 0 & 0 & -i\partial_z & i\partial_y & -i & 0 & 0 & 0 \\ 0 & 0 & 0 & i\partial_z & 0 & -i\partial_x & 0 & -i & 0 & 0 \\ 0 & 0 & 0 & -i\partial_y & i\partial_x & 0 & 0 & 0 & -i & 0 \\ 0 & i\partial_z & -i\partial_y & 0 & 0 & 0 & 0 & 0 & 0 & 0 \\ -i\partial_z & 0 & i\partial_x & 0 & 0 & 0 & 0 & 0 & 0 & 0 \\ i\partial_y & -i\partial_x & 0 & 0 & 0 & 0 & 0 & 0 & 0 & 0 \\ i\frac{\omega_p^2}{c^2} & 0 & 0 & 0 & 0 & 0 & 0 & -i\frac{\omega_c}{c} & 0 & -i\frac{\beta^2}{c^2}\partial_x \\ 0 & i\frac{\omega_p^2}{c^2} & 0 & 0 & 0 & 0 & i\frac{\omega_c}{c} & 0 & 0 & -i\frac{\beta^2}{c^2}\partial_y \\ 0 & 0 & i\frac{\omega_p^2}{c^2} & 0 & 0 & 0 & 0 & 0 & 0 & -i\frac{\beta^2}{c^2}\partial_z \\ 0 & 0 & 0 & 0 & 0 & 0 & -i\partial_x & -i\partial_y & -i\partial_z & 0 \end{pmatrix} \tag{3.53}$$

To get the dispersion relations for this model, we can either solve equation (3.52) with respect to $\mathbf{j}$, obtain the polarizability and electric displacement vectors and with it derive the permittivity tensor, just like in section 3.2.1, or we can solve the equivalent eigenvalue problem with the help of the $\hat{L}$ operator. The permittivity tensor of this model for $k_z = 0$ is:

$$\frac{\overline{\epsilon}_{hydro}}{\epsilon_0}(\omega,\mathbf{k}) = \mathbb{1} - \frac{\omega_p^2}{\omega^2}\left(\frac{\Delta}{\Delta+\omega_c^2}\mathbb{1}_t + \hat{\mathbf{z}}\otimes\hat{\mathbf{z}} - \frac{\beta^2\mathbf{k}\otimes\mathbf{k}}{\Delta+\omega_c^2}\right) + \frac{1}{\omega}\frac{i\omega_c\omega_p^2}{\Delta+\omega_c^2}\hat{\mathbf{z}}\times\mathbb{1}, \tag{3.54}$$

where $\Delta = \beta^2k^2 - \omega^2$, $k^2 = \mathbf{k}\cdot\mathbf{k}$ and $\otimes$ is the tensor product.

This model introduces spatial dispersion or nonlocality since the electric displacement and the electric fields are linked by differential operators, or in other words, the permittivity tensor depends on the wave vector $\mathbf{D} = \overline{\epsilon}(\omega,\mathbf{k})\cdot\mathbf{E}$, with $\mathbf{k} = -i\nabla$ (in the harmonic regime). The nonlocality only affects the longitudinal modes [2, 16] and this is well observed in figures 3.20-3.21. For xoy propagation, the low frequency TM mode bends upward, so it no longer has the limit from equation (3.37), but now $\omega \to \infty$ as $k \to \infty$. In the direction orthogonal to this plane, in the k_z axis, it is the longitudinal mode that gets curved, no longer staying flat and $\omega \to \infty$ as $k \to \infty$.

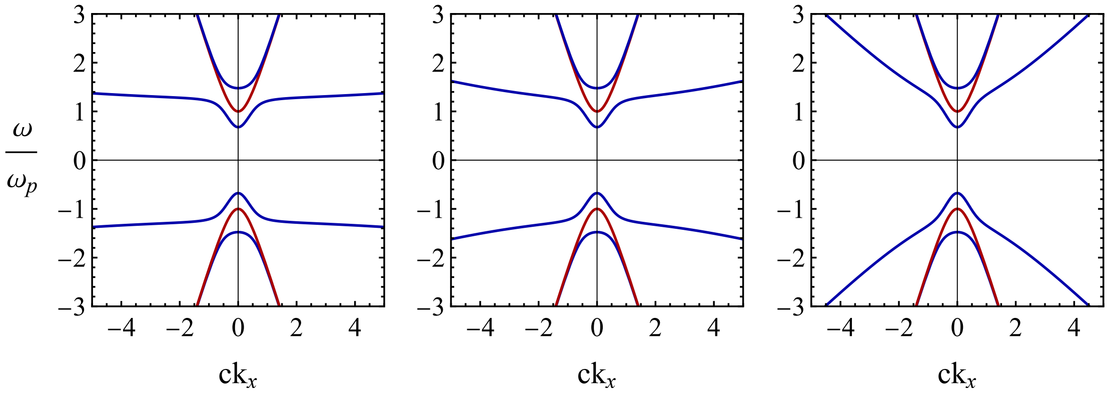

Figure 3.20: Dispersion in xoy plane ($k_z = 0$) - varying with β: from left to right, $\beta = 0.05c$, $\beta = 0.1c$, $\beta = 0.3c$. The TM modes are displayed in blue and the TE modes are displayed in red. All of the plots have the parameters $\omega_c = 0.8\omega_p$, $\omega_p = 0.5c$.

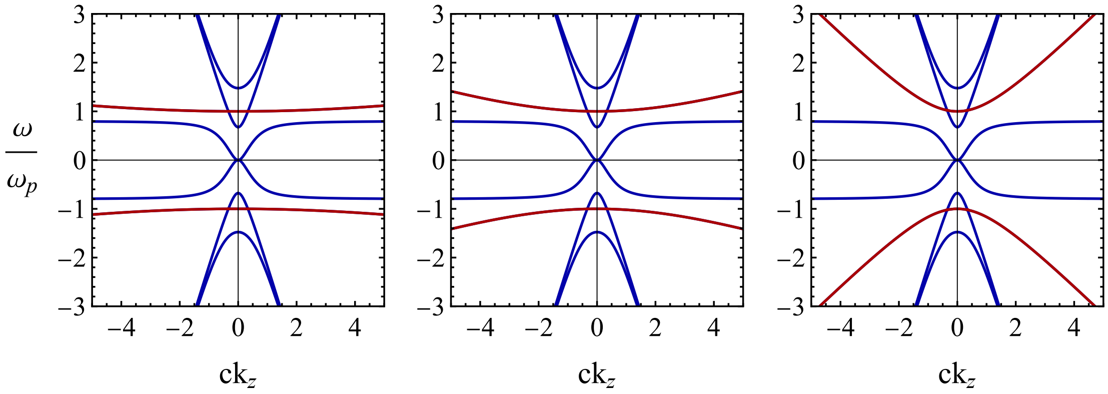

Figure 3.21: Dispersion in the k_z axis - varying with β: from left to right, $\beta = 0.05c$, $\beta = 0.1c$, $\beta = 0.3c$. The longitudinal mode is displayed in red and the transverse modes are displayed in blue. All of the plots have the parameters $\omega_c = 0.8\omega_p$, $\omega_p = 0.5c$.

With this model, the number of Weyl points one can get is now dependent on one more parameter. Moreover, the maximum number of Weyl pairs (in momentum space) that emerge in this system is now three. This means that with a specific combination of parameters $(\omega_p, \omega_c, \beta)$, it is possible to satisfy the different cases where there is only one, two or three pairs of Weyl crossings. See figure 3.22 for the three cases. Specifically, in the regime $\omega_c < \omega_p$ there is only one Weyl pair, but for the regime $\omega_c > \omega_p$ it is possible to have up to three, as observed in figure 3.22.

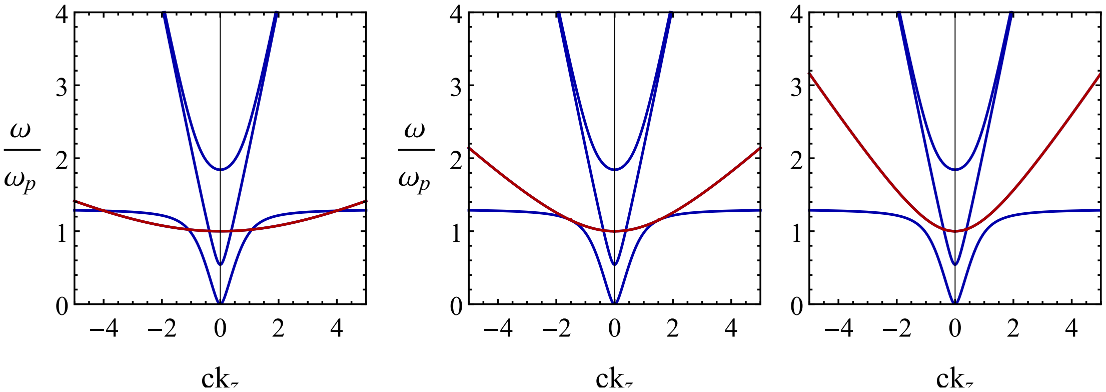

Figure 3.22: Showcasing the three possible cases of Weyl crossings in the k_z axis - varying with β: from left to right, $\beta = 0.1c$, $\beta \approx 0.189c$, $\beta = 0.3c$. The longitudinal mode is displayed in red and the transverse modes are displayed in blue. All of the plots have the parameters $\omega_c = 1.3\omega_p$, $\omega_p = 0.5c$.

Similarly with the helical metamaterial case discussed in section 3.1, the type of Weyl point changes with the introduction of the nonlocality. The crossings between the longitudinal mode and the transverse modes have isofrequency surfaces around it which are hyperboloids. This means that we are dealing with a type-II Weyl point, as one can observe in figure 3.23. If we compare figures 3.21 and 3.8, this is the case of a negative α, and so we have a crossing between a longitudinal mode and a transverse mode, both with group velocities $v_g = \frac{\partial\omega}{\partial k}$ with the same sign. The isofrequency curves are always circular when looking in the $\hat{\mathbf{x}}$ and $\hat{\mathbf{y}}$ directions, due to the rotational symmetry. Therefore to observe the hyperbolicity one needs to check necessarily the $\hat{\mathbf{z}}$ direction plus either $\hat{\mathbf{x}}$ or $\hat{\mathbf{y}}$, both being equivalent because of the rotational symmetry.

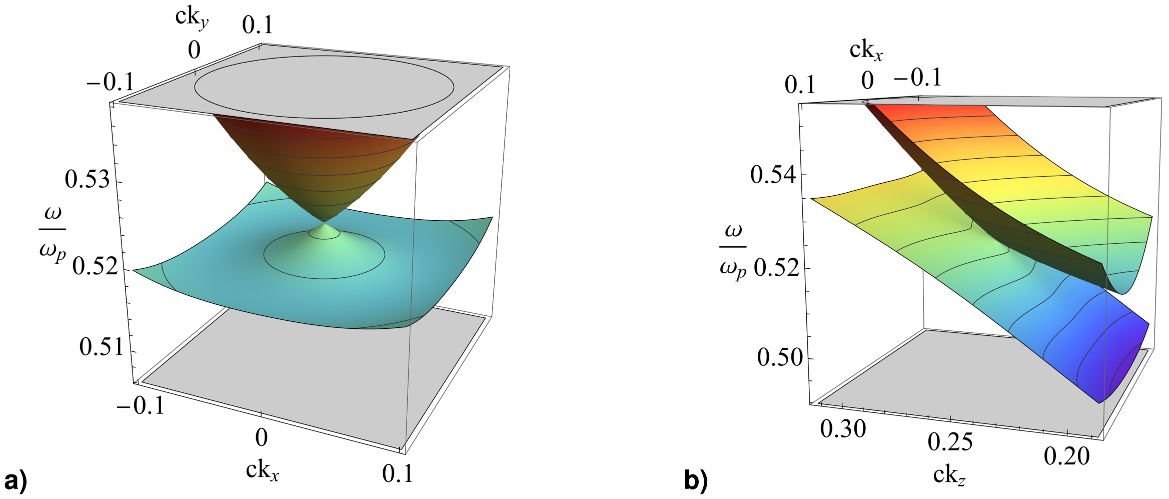

Figure 3.23: Dispersion surfaces and isofrequency curves around Weyl point in **a)** $\hat{\mathbf{x}}$ and $\hat{\mathbf{y}}$ directions and in **b)** $\hat{\mathbf{z}}$ and $\hat{\mathbf{x}}$ directions. The parameters used here were $\beta = 0.6c$, $\omega_c = 0.2\omega_p$ and $\omega_p = 0.5c$.

With respect to the topological characterization of this model, there is one crucial effect that arises with this specific regularization procedure. The effect of the nonlocality on the low-frequency TM mode (figure 3.20) prohibits the possibility of a high-frequency full band gap, even with a plasma frequency shift in the $\hat{\mathbf{z}}$ direction. Hence only the low-frequency band gap can be topologically characterized with our formalism.

3.2.3 Full Cut-Off Model

The full cut-off model implements a high-frequency spatial cut-off to the material response of a system, as:

$$\mathbf{M}_{reg}\left(\omega,\mathbf{k}\right)=\mathbf{M}_{\infty}+\frac{1}{1+k^{2}/k_{max}^{2}}\left(\mathbf{M}\left(\omega\right)-\mathbf{M}_{\infty}\right), \tag{3.55}$$

where $\mathbf{M}\left(\omega\right)$ is the material matrix of the system that represents its electromagnetic response, $\mathbf{M}_{\infty}=lim_{\omega\rightarrow\infty}\mathbf{M}\left(\omega\right)$, $k=\mathbf{k}\cdot\mathbf{k}$ and k_{max} is the high-frequency wave vector cut-off. The consequence of this model is that when $k\rightarrow\infty$, then $\mathbf{M}_{reg}\rightarrow\mathbf{M}_{\infty}$, with $\mathbf{M}_{\infty}$ usually set as the vacuum response. In other words, for large values of k, when $k\gg k_{max}$, the material response is suppressed. When $k\ll k_{max}$, so for small wavelengths comparatively to the cut-off spatial frequency, the regularized material matrix is approximately the original $\mathbf{M}_{reg}\approx\mathbf{M}\left(\omega\right)$. This model has a physical justification. When dealing with realistic materials, fields with very fast spatial variation cannot effectively polarize the microscopic constituents of the medium, therefore its response is effectively suppressed when $k\rightarrow\infty$ and it should reduce to that of the vacuum [2]. For crystalline materials, this cut-off may be estimated as $k_{max}\sim 1/a$, with a the lattice constant. Furthermore, it has been theoretically and experimentally shown that a thin layer of air in-between two materials may effectively imitate this cut-off effect. Let us say a magnetized plasma is separated from a regular plasma by a layer of air with thickness d. If they both share a band gap at the interface, for large wavelengths $|kd|\ll 1$, the cut-off can be approximated as $k_{max}\approx 1/d$ and an edge state can flow in this interface [16]. Conversely, for $|kd|\gg 1$, the air gap is ineffective because the wavelength is much larger than its thickness and so the topology is ill-defined, violating the bulk-edge correspondence. In theses cases, the energy flow can be halted, creating a topological energy sink [32, 33].

In the case of the magnetized plasma, since it has no magnetoelectric coupling ($\overline{\xi}=\overline{\zeta}=0$) and a trivial magnetic response $\overline{\mu}=\mu_0\mathbb{1}$, the application of the full cut-off is performed on the permittivity tensor as follows:

$$\overline{\epsilon}_{cut-off}\left(\omega,\mathbf{k}\right)=\epsilon_0\mathbb{1}+\frac{1}{1+k^{2}/k_{max}^{2}}\left(\overline{\epsilon}_{loc}-\epsilon_0\mathbb{1}\right), \tag{3.56}$$

where $\overline{\epsilon}_{loc}$ is the permittivity tensor of a local magnetized plasma, given in equation (3.25). Just like the hydrodynamic model, the cut-off model of a magnetized plasma is spatially dispersive. However, the high-frequency material response is that of the vacuum and it is independent of the wave vector, i.e.

local. Importantly, it becomes reciprocal because $\bar{\epsilon} = \bar{\epsilon}^T$.

Unlike the hydrodynamic one, this full cut-off model for a magnetized plasma affects all of the dispersion bands. In the xoy plane, the low frequency TM mode is the most affected, again no longer having the limit in 3.37 but now $\omega \to \omega_c$ as $k \to \infty$.

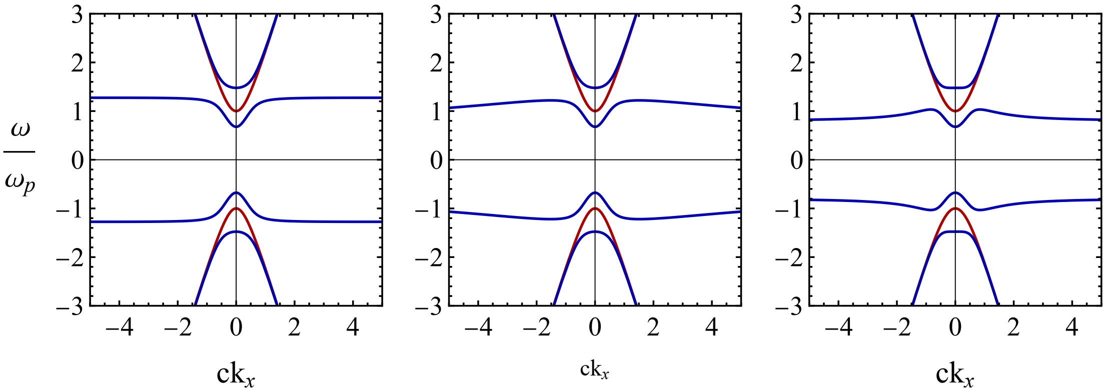

Figure 3.24: Dispersion in xoy plane - varying with k_{max}: from left to right, $k_{max} = 100\omega_p/c$, $k_{max} = 10\omega_p/c$, $k_{max} = 2\omega_p/c$. The TM modes are displayed in blue and the TE modes are displayed in red. All of the plots have the parameters $\omega_c = 0.8\omega_p$, $\omega_p = 0.5c$.

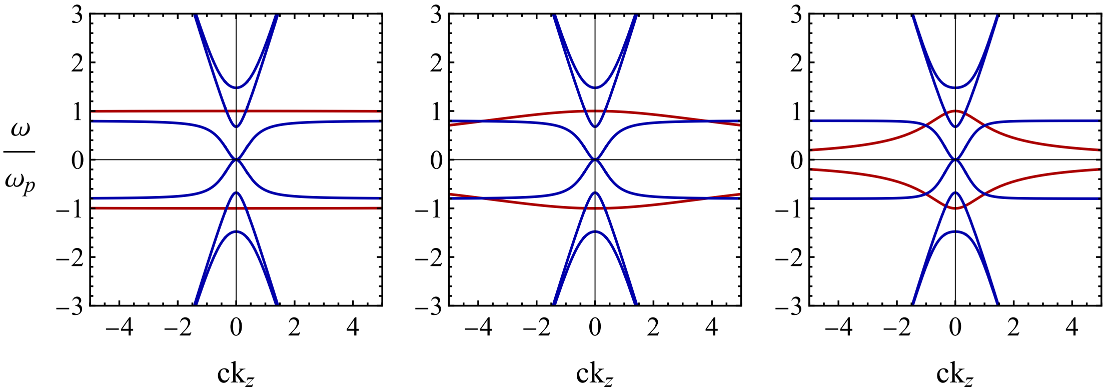

Figure 3.25: Dispersion in the k_z axis - varying with k_{max}: from left to right, $k_{max} = 100\omega_p/c$, $k_{max} = 10\omega_p/c$, $k_{max} = 2\omega_p/c$. The longitudinal mode is displayed in red and the transverse modes are displayed in blue. All of the plots have the parameters $\omega_c = 0.8\omega_p$, $\omega_p = 0.5c$.

The most significant effect is that the longitudinal mode in k_z axis bends downward, contrarily to the hydrodynamic model, and instead of being a flat mode its limit is set by $\omega \to 0$ as $k_z \to \infty$, for any real value of k_{max}. Although this is not noticeable in the first plot of figure 3.25, if we increase the range of the wave vector axis, we can see that this is always the case. The immediate consequence is that for this model there are always two pairs of Weyl points in the k_z axis, because the longitudinal mode crosses two transverse modes. This will be an important detail for the topological characterization in chapter 4.

The nonlocality also changes the type of Weyl point, but this time the isofrequency surfaces that surround the crossing are ellipsoids. Thus this model originates type-I Weyl degeneracies. Comparing figures 3.25 and 3.8, we conclude that this is analogous to the case of a positive α parameter in the helical metamaterial (see figure 3.3). In these conditions, the group velocities of the longitudinal and transverse modes have different signs.

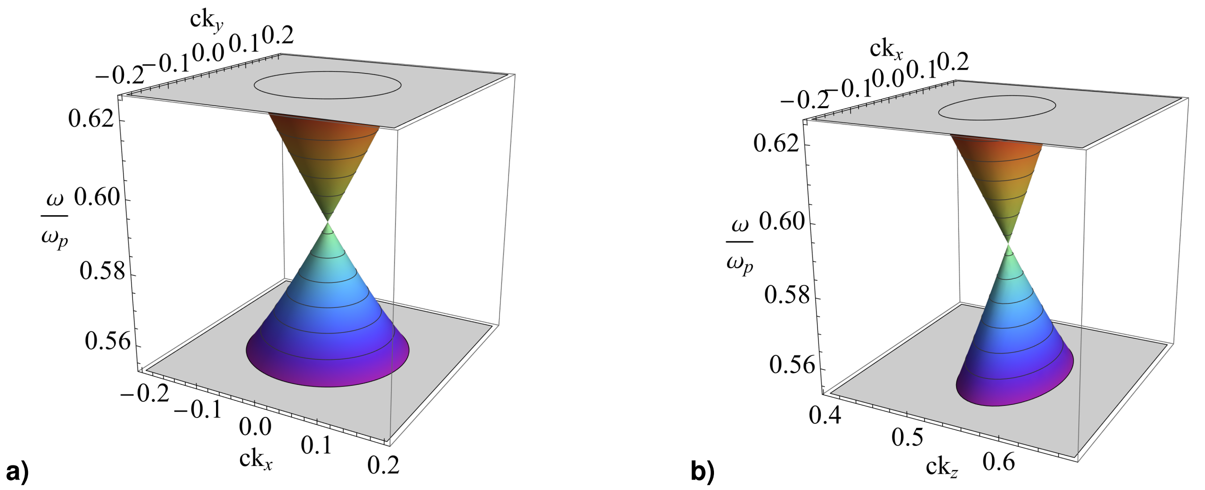

Figure 3.26: Dispersion surfaces and isofrequency curves around Weyl point in **a)** $\hat{\mathbf{x}}$ and $\hat{\mathbf{y}}$ directions and in **b)** $\hat{\mathbf{z}}$ and $\hat{\mathbf{x}}$ directions. The parameters used here were $k_{max} = \omega_p/c$, $\omega_c = 1.2\omega_p$ and $\omega_p = 0.5c$.

With this model, it is now possible to achieve a high-frequency band gap between the TE mode and low-frequency TM mode, by applying the plasma frequency shift only in the $\hat{\mathbf{z}}$ direction. This corresponds again to altering ϵ_z which is the zz component of ϵ_{loc} in 3.56, substituting it with 3.43. The band gaps in the xoy plane are displayed in figure 3.27.

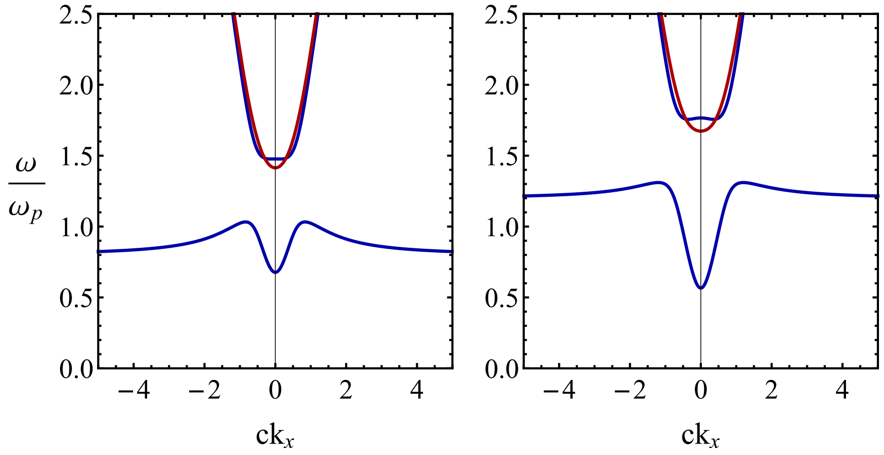

Figure 3.27: Dispersion in xoy plane with new ϵ_z. TM modes are in blue and TE mode is in red. Parameters used on the left were: $\omega_c = 0.8\omega_p$ $\omega_p' = \sqrt{2}\omega_p$. On the right: $\omega_c = 1.2\omega_p$ $\omega_p' = \sqrt{2.8}\omega_p$. On both plots were: $\omega_p = 0.5c$ and $k_{max} = \omega_p/c$.

Importantly, the number of Weyl crossings is the same with a cut-off model with and without the plasma frequency shift. We can now topologically characterize both the low-frequency and the high-frequency band gaps in cross sections. More will be explained in chapter 4.

Lastly, following the same procedure in section 2.2.2, the $\hat{L}$ operator that describes the cut-off model of a magnetized plasma is quickly obtainable. The full cut-off model can be enforced in the system by changing the current density vector **j** in Maxwell's equations (2.18), replacing it with $(-k_{max}^{-2}\nabla^2 + 1)^{-1}\mathbf{j}$. To include the plasma frequency shift, we must again alter component (9,3) of the matrix to include ω_p'. The derived operator is thus:

$$\hat{L}(-i\nabla) =$$

$$= \begin{pmatrix} 0 & 0 & 0 & 0 & -i\partial_z & i\partial_y & \frac{-i}{(-k_{max}^{-2}\nabla^2+1)} & 0 & 0 & 0 \\ 0 & 0 & 0 & i\partial_z & 0 & -i\partial_x & 0 & \frac{-i}{(-k_{max}^{-2}\nabla^2+1)} & 0 & 0 \\ 0 & 0 & 0 & -i\partial_y & i\partial_x & 0 & 0 & 0 & \frac{-i}{(-k_{max}^{-2}\nabla^2+1)} & 0 \\ 0 & i\partial_z & -i\partial_y & 0 & 0 & 0 & 0 & 0 & 0 & 0 \\ -i\partial_z & 0 & i\partial_x & 0 & 0 & 0 & 0 & 0 & 0 & 0 \\ i\partial_y & -i\partial_x & 0 & 0 & 0 & 0 & 0 & 0 & 0 & 0 \\ i\frac{\omega_p^2}{c^2} & 0 & 0 & 0 & 0 & 0 & 0 & -i\frac{\omega_c}{c} & 0 & 0 \\ 0 & i\frac{\omega_p^2}{c^2} & 0 & 0 & 0 & 0 & i\frac{\omega_c}{c} & 0 & 0 & 0 \\ 0 & 0 & i\frac{\omega_p'^2}{c^2} & 0 & 0 & 0 & 0 & 0 & 0 & 0 \\ 0 & 0 & 0 & 0 & 0 & 0 & -i\partial_x & -i\partial_y & -i\partial_z & 0 \end{pmatrix} \tag{3.57}$$

4

Topological Characterisation of Band Structures

Contents

4.1 Ill-Defined Topology of Local Model 46
4.2 Topological Study of Models With Regularized Responses 51
4.3 Convergence Study 57

This chapter contains the main results of the work of this thesis. By applying the Green's function formalism to compute gap Chern numbers, we were able to topologically characterize two different nonlocal models of magnetized plasma with regularized electromagnetic responses. The regularization procedure was required because the local model of magnetized plasma has an ill-defined topology.

4.1 Ill-Defined Topology of Local Model

Here we introduce the approach we undertook to quantify the topological charge of Weyl points in a magnetized plasma. We will only topologically characterize this medium as it is very well studied in the literature and its electrodynamics are much simpler than that of the helical metamaterial. For example, in the magnetized plasma case, the planes in wave vector space which are orthogonal to the k_z axis have dispersion characteristics with rotational invariance. This is not true for the other structure. Nevertheless, our methods could be extended to the effective medium model of the helical metamaterial.

The task to obtain the charge of the Weyl points with the Green's function formalism is a complex one, considering both the facts that we are dealing with 3-dimensional band degeneracies and that the procedure we utilize characterizes the Chern number of full band gaps. The standard problem of Chern number characterization in a rotationally invariant 2D magnetized plasma is illustrated in figure 4.1. In the example, the medium has the permittivity tensor in equation (3.25) and we only consider the TM modes propagating in the xoy plane which is orthogonal to the direction of the applied magnetic field. The problem only contemplates two dimensions in wave vector space, but due to rotational symmetry, we can observe the dispersion in one direction (for instance in the k_x axis) and the same will be observed in other directions in the plane. Now we simply compute the gap Chern numbers of the band gaps between the TM modes or between the low-frequency TM mode and the zero frequency $\omega = 0$.

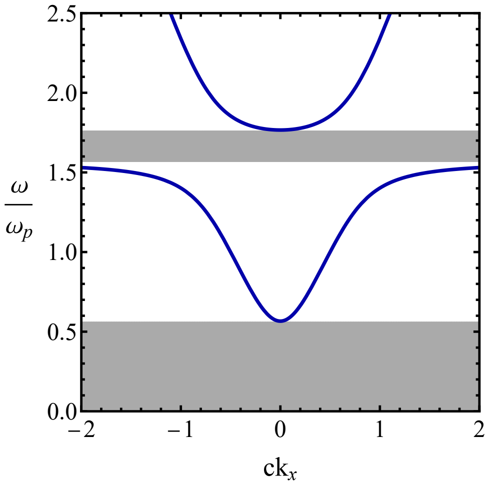

Figure 4.1: Dispersion in the k_x axis of the TM modes of a local magnetized plasma with parameters $\omega_c = 1.2\omega_p$ and $\omega_p = 0.5c$. The band gaps are highlighted in grey.

This case has been studied extensively in the literature [14, 16, 31]. With appropriate regularization, this band structure has topological band gaps such that a finite medium hosts protected edge modes.

The Weyl points arise in the k_z axis, for the case of a magnetized plasma with a bias static magnetic field in the $\hat{\mathbf{z}}$ direction. Our approach will add this wave vector component as an extra dimension for the problem of topological characterization. We then select a cross section in wave vector space that is orthogonal to this axis by fixing a k_z value. Due to the rotational symmetry we just need to choose one direction in this plane to plot the dispersion and observe the band gaps that emerge. For simplicity we always choose the $\hat{\mathbf{x}}$ direction. If we were able to measure a change in the gap Chern number of band gaps situated in cross sections before and after the Weyl crossing, we could quantify its topological charge, by taking the difference. Of course, the band gaps must be between bands that intersect at the Weyl point.

The first object of this study will be the local magnetized plasma with a shifted plasma frequency ω_p' in the $\hat{\mathbf{z}}$ direction, henceforth referred to as the "local model", introduced in section 3.2. As it was explained there, this model only originates the inner pair of Weyl points, so if we take a look at the positive part of the 3-dimensional dispersion characteristic, we can only observe one Weyl crossing, as displayed in figure 4.2.

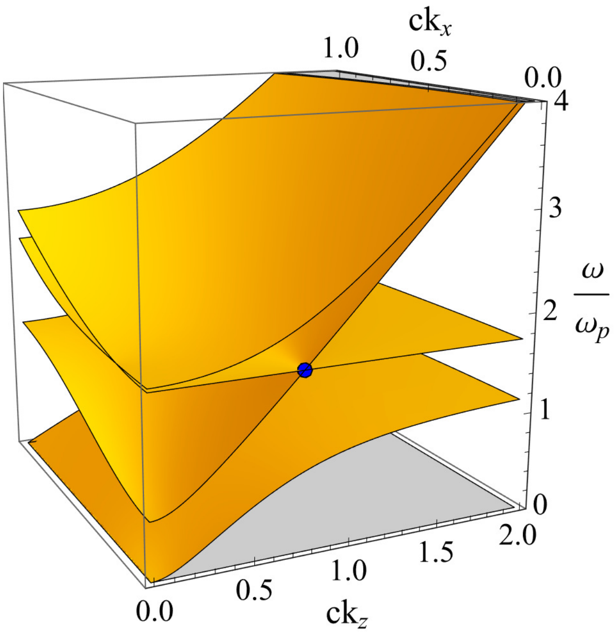

Figure 4.2: Local model - dispersion in k_z and k_x. The propagating modes along k_z are showcased on the foreground. The Weyl crossing is represented by the blue circle. The parameters used here were $\omega_c = 1.2\omega_p$, $\omega_p' = \sqrt{3}\omega_p$ and $\omega_p = 0.5c$.

We will focus on two regions highlighted in different colours, one in blue and one in orange, as illustrated in figure 4.3. On the left plot of this figure, we can observe the dispersion along the k_z axis and the regions that will be topologically characterized. On the right plot, we can see the dispersion in the $\hat{\mathrm{x}}$ direction situated in the cross section with $k_z = 0$. There, two full band gaps are displayed: the high-frequency band gap that appears between the low-frequency TM mode and the lowest point of the TE mode, highlighted in blue because it is in the blue region; and the low-frequency band gap that appears between the zero frequency $\omega = 0$ and the lowest point of the low-frequency TM mode, highlighted in orange because it appears in the orange region. Our aim is to then calculate the Chern invariant of each band gap, and we repeat this procedure in various cross sections, for different values of k_z.

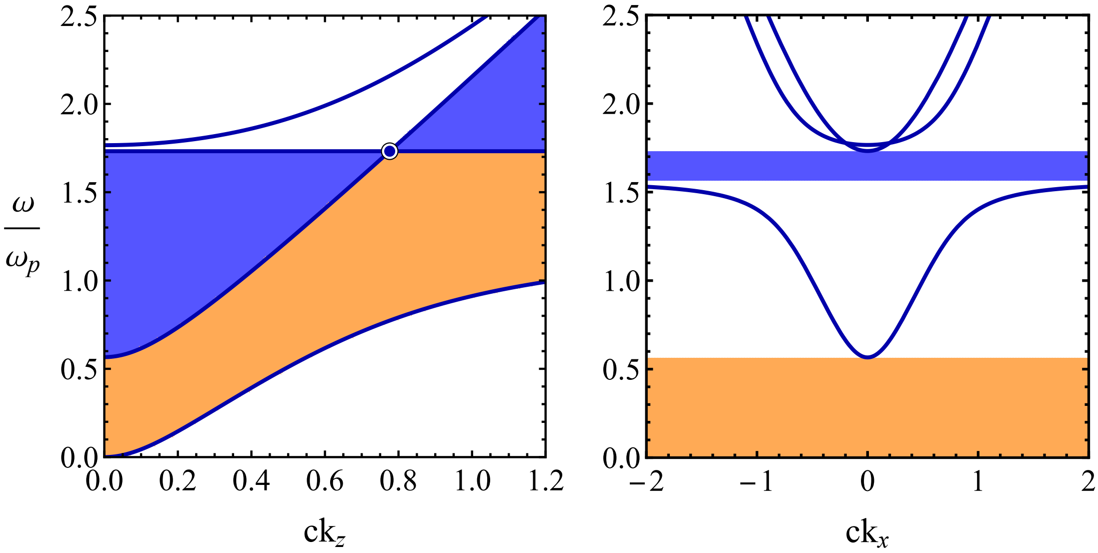

Figure 4.3: Dispersion in the k_z axis on the left exhibits the two regions of interest, in blue and orange. On the right is a cross section of the 3-dimensional dispersion (fig. 4.2), for $k_z = 0$, where the high-frequency band gap is highlighted in blue and the low-frequency one is in orange. The Weyl crossing is represented by the blue circle. The parameters used here were $\omega_c = 1.2\omega_p$, $\omega_p' = \sqrt{3}\omega_p$ and $\omega_p = 0.5c$.

We now apply the Green's function method to compute the gap Chern numbers C_{gap}. C^1_{gap} is relative to the blue band gap and C^2_{gap} is relative to the orange band gap, and the numerical results were $C^1_{gap} = 0.999377$ and $C^2_{gap} = -0.7635322$. The first result is close to +1 and the second result is far from being close to an integer number. To explain these results we will examine the analytical solutions for these gap Chern numbers.

Firstly, it has been shown in [31] that the TE modes propagating in the xoy plane of a local magnetized plasma are topologically trivial. This means that this band's Chern number is zero, so even if this mode is shifted up due to the influence of ω_p', intersecting the high-frequency TM mode, the Chern number of the group formed by these two bands is equal to the Chern number of just the TM mode. This also means that this mode has a null contribution for the gap Chern numbers, ergo the high-frequency band gap of the right plot in figure 4.3 is topologically equivalent to the band gap just between the TM modes. The latter is the high-frequency band gap observed in figure 4.1. The analytical results of the gap Chern numbers, for the band gaps depicted in this figure are presented in [14, 16, 31]. The gap Chern number of the high-frequency band gap is $C^1_{gap}* = +1$ and the low-frequency band gap has a gap Chern number $C^2_{gap}* = -1/\sqrt{1+\omega_p^2/\omega_c^2} \approx -0.768221$, for the constitutive parameters $\omega_c = 1.2\omega_p$ and $\omega_p = 0.5c$. If we compare these with the numerical results we have a relative error of 0.06% and 0.61%, respectively.

The reason why the second gap Chern number is not an integer number is because the topology of the low-frequency TM mode is ill-defined, consequently having a non-integer Chern number. This is the only mode in this situation whose topology is ill-defined and to understand why, we will start by explaining why the other two branches have a well-defined topology. Both the TE and the high-frequency TM modes' limits when $k \to \infty$ are such that $\omega \to \infty$, and as a consequence the material response for these bands approach that of the vacuum (where $\bar{\epsilon} \to \epsilon_0$) in $k \to \infty$. Thus, it is always possible to have integer Chern numbers for these branches [16]. This is not the case with the low-frequency TM mode since it has a constant asymptotic behaviour. These asymptotes are of the form $\omega \to \omega_{n,\infty} = const.$ as $k \to \infty$ and so, the material response for these modes as $k \to \infty$ is $\bar{\epsilon} \to \bar{\epsilon}\left(\omega_{n,\infty}\right)$, which may be different from the material matrix of a reciprocal medium and is usually complex-valued. In the case of this branch whose asymptote is given by $\omega_{n,\infty} = \sqrt{\omega_c^2 + \omega_p^2}$, it can be seen that its material response when $k \to \infty$ is not reciprocal, just by analysing the limits of the components ϵ_t and ϵ_g of the permittivity tensor:

$$\lim_{k\to\infty} \epsilon_t\left(\omega_{n,\infty}\right) = \lim_{k\to\infty} \epsilon_0 \left[1 - \frac{\omega_p^2}{\omega_{n,\infty}^2 - \omega_c^2}\right] = 0 \tag{4.1}$$

$$\lim_{k\to\infty} \epsilon_g\left(\omega_{n,\infty}\right) = \lim_{k\to\infty} \epsilon_0 \left[\frac{-\omega_c\omega_p^2}{\omega_{n,\infty}(\omega_{n,\infty}^2 - \omega_c^2)}\right] = \epsilon_0 \left[\frac{-\omega_c}{\sqrt{\omega_c^2 + \omega_p^2}}\right] \tag{4.2}$$

Because we're dealing with a local model, hence since there is no spatial dispersion in the permittivity tensor, the material response of this mode (i.e. the limits above) persists even for fast spatial variations of the electromagnetic fields, which is unrealistic. Furthermore, the result of equation 4.1 is also not physically realistic.

Hence, an extra step is required. Since we are dealing with a continuous medium some cut-off should be included to the material response, so as to ensure that its nonreciprocal components are suppressed for large wave vectors. For this purpose, the two models described in sections 3.2.1 and 3.2.2 were implemented. They will be topologically characterized in the next section with the same approach described in this one.

Additionally, this is the reason why in the example of reference [17], the band folding caused by the accumulation of bands in a single frequency (see **(b)** of figure 1.4) causes an ill-defined topology in a dispersive photonic crystal whose unit cell includes a magnetized plasma. Initially, the periodicity of the crystal was thought to act as a cut-off to solve this issue of the local model, but it was not enough, and so the problems of ill-defined topologies in a photonic crystal are connected to those in the continuum.

Specifically, the mode with non-zero constant asymptote in the local model is the problem.

It should be noted that due to symmetry, the gap Chern numbers of symmetric band gaps (in frequency) are equal and the same result is observed for band gaps in symmetric cross sections, i.e. for symmetric values of k_z. However, frequency-symmetric bands have symmetric Chern numbers as it can be seen in figure 4.4, for $k_z = 0$. The positive and negative low-frequency band gaps seem to form one completely joint band gap, but this is not true since there are flat (dark) modes at $\omega = 0$ which are not topologically trivial [31]. Nonetheless, they are inconsequential in the topological characterization of the band gaps because these flat modes have symmetric Chern numbers, and so they cancel out.

The band gaps with the same colour have thus the same gap Chern number: $C^1_{gap} = +1$ for the blue band gaps and $C^2_{gap} = -1/\sqrt{1+\omega_p^2/\omega_c^2}$ for the orange band gaps. In figure 4.4, we can observe the importance of the negative frequency modes for the computation of the gap Chern number. The gap Chern number C^1_{gap} of the negative high-frequency blue band gap is the sum of the Chern numbers of the negative TE and high-frequency TM modes: $C^1_{gap} = +1 + 0 = +1$. In turn, the gap Chern number of the orange band gap C^2_{gap} is the sum of C^1_{gap} and the Chern number of the negative low-frequency TM mode: $C^2_{gap} = +1 - 1 - 1/\sqrt{1+\omega_p^2/\omega_c^2} = -1/\sqrt{1+\omega_p^2/\omega_c^2}$. The reason why the high-frequency blue band gap has a well-defined topology meaning it is an integer number and it is not affected by the ill-defined topologies is because the Chern numbers of the negative and positive low-frequency TM modes cancel out: $C^1_{gap} = 1 + 1/\sqrt{1+\omega_p^2/\omega_c^2} - 1 - 1/\sqrt{1+\omega_p^2/\omega_c^2} + 1 + 0 = +1$.

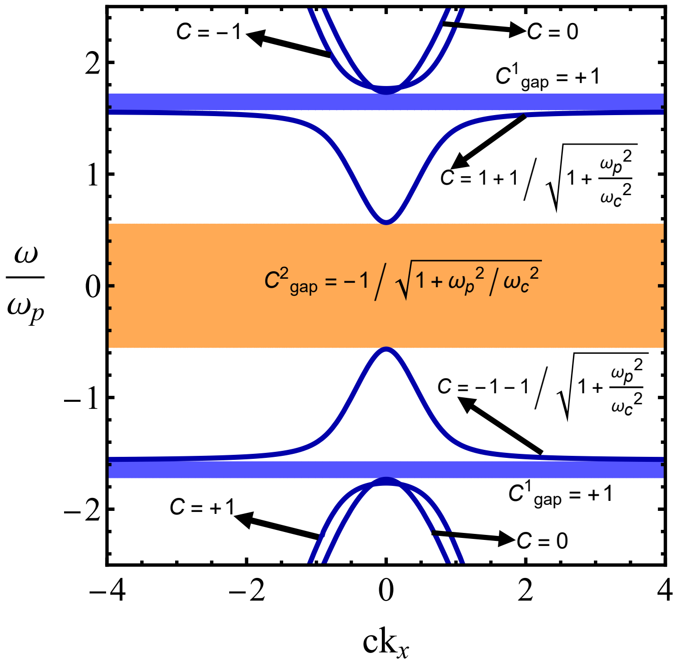

Figure 4.4: k_x dispersion showcasing the positive and negative frequencies for $k_z = 0$. High-frequency band gaps are highlighted in blue and the low-frequency one in orange. Parameters used here were $\omega_c = 1.2\omega_p$, $\omega'_p = \sqrt{3}\omega_p$ and $\omega_p = 0.5c$.

4.2 Topological Study of Models With Regularized Responses

The first solution that we tried as a means to regularize the response of a magnetized plasma is the hydrodynamic model. For this study, we chose a set of constitutive parameters with which there is only one pair of Weyl points, and their location in momentum space will be referred to as $k_z = \pm W$ (plus sign for the one at a positive wave vector value and vice-versa). Furthermore, as it can be seen in figures 4.5-4.7, there is a region in the 3-dimensional dispersion where a low frequency band gap exists regardless of the direction of propagation. We can see another crucial consequence of this model in figure 4.7, this time an universal one, no matter the parameters chosen. The low-frequency TM mode in the k_x axis (for $k_z = 0$, left panel of the figure) and the longitudinal mode in the k_z axis (fig. 4.6) lifts up, for any positive value of diffusion velocity β. This results in the nonexistence of a full band gap between the positive frequency modes, in any cross section at any k_z value. This makes it impossible to quantify the charge of the Weyl point with our proposed approach, or more specifically we cannot topologically characterize the blue region in figure 4.6. However, important results can be drawn from the topological study of the orange region.

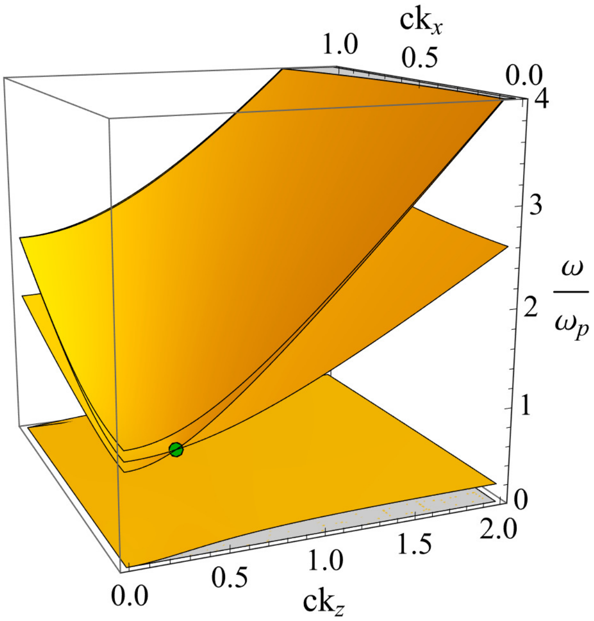

Figure 4.5: Hydrodynamic model - dispersion in k_z and k_x. The propagating modes along k_z are showcased on the foreground. The Weyl crossing is represented by the green circle. The parameters used here were $\beta = 0.6c$, $\omega_c = 0.2\omega_p$, $\omega_p' = \omega_p$ and $\omega_p = 0.5c$.

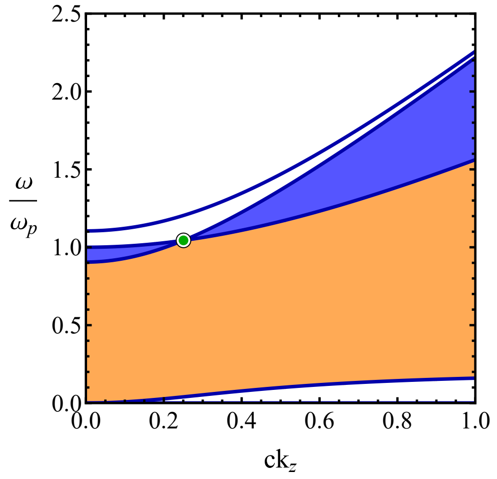

Figure 4.6: Dispersion in the k_z axis exhibiting the two regions of interest in blue and orange. The Weyl crossing is highlighted with the green circle. The parameters used here were $\beta = 0.6c$, $\omega_c = 0.2\omega_p$, $\omega_p' = \omega_p$ and $\omega_p = 0.5c$.

The two regions of interest are highlighted in blue and orange in figure 4.6, but as stated our approach can only topologically characterize the orange region. This region is not influenced by any Weyl point, in the sense that it is not confined between two bands that intersect at a Weyl crossing. Three cross sections were chosen with distinct k_z values: $k_z = 0$, $k_z = W$, $k_z = \frac{3}{2}W$, corresponding to a location in momentum space which is before, at and after the Weyl point, respectively. The band gaps that will be characterized are shown in figure 4.7. Again, it is to be noted that there is a flat mode at $\omega = 0$ for $k_z = 0$ which can be seen rising in the other cross sections.

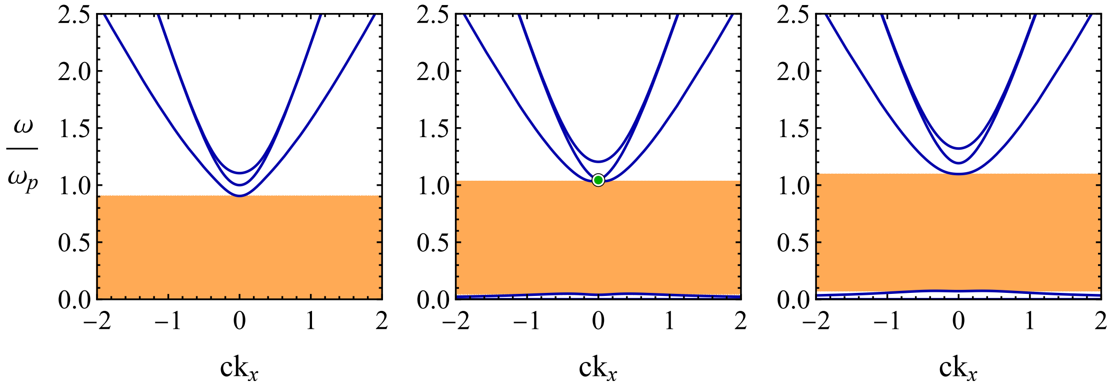

Figure 4.7: Cross sections of the 3-dimensional dispersion (fig. 4.5) for different values of k_z. From left to right, $k_z = 0$, $k_z = W$ and $k_z = \frac{3}{2}W$. The band gaps are highlighted in orange and the Weyl point with the green circle. The parameters used here were $\beta = 0.6c$, $\omega_c = 0.2\omega_p$, $\omega_p' = \omega_p$ and $\omega_p = 0.5c$.

The gap Chern numbers computed for the three cases were the same: $C_{gap} = 0$ which means that the three gaps are topologically trivial. This is expected for a combination of reasons. First of all, the orange region exhibits a full band gap in any cross section and for the interval $k_z \in]-\infty, +\infty[$, only the band gaps' amplitude varies and in a smooth way. This means that, since there is no discontinuity, the gaps' topological invariants (in each cross section) should always be the same. Furthermore, as a result of the regularization, the material's nonreciprocal response to the low-frequency TM mode in the xoy plane is suppressed for large wave vectors, and specifically for $k \to \infty$ the medium is reciprocal which justifies the trivial topology.

The second solution to regularize the topology of a magnetized plasma is the implementation of a full spatial cut-off. With this model, two Weyl points always arise in the positive part of the dispersion characteristic, as observed in figure 4.8. The first or inner Weyl crossing appears for the wave vector value $k_z = W_1$ and the second or outer one appears for $k_z = W_2$. This solution is quite different from the hydrodynamic model, in the sense that we no longer have full band gaps in every cross section situated in the orange region. Specifically, the only values where a full band gap cannot be observed in the cross section are the outer Weyl points, $k_z = \pm W_2$. Additionally, with this model we can observe full band gaps in cross sections situated in the blue region as well. Again, the only values where no band gap is observed are the inner Weyl crossings, $k_z = \pm W_1$. As a consequence, we can topologically characterize two regions that are directly influenced by each Weyl point, by computing gap Chern numbers in cross sections before and after these crossings. The regions of interest are illustrated in figure 4.9.

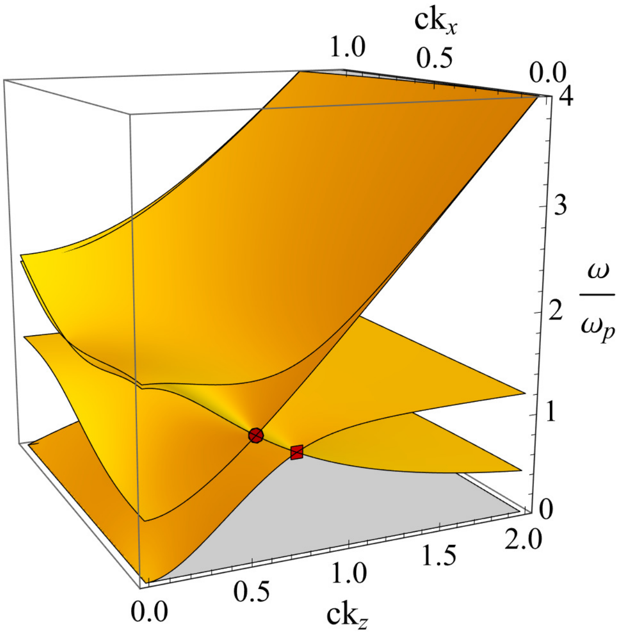

Figure 4.8: Full cut-off model - dispersion in k_z and k_x. The propagating modes along k_z are showcased on the foreground. The inner Weyl crossing is represented by the red circle and the outer one is represented by the red square. The parameters used here were $k_{max} = \omega_p/c$, $\omega_c = 1.2\omega_p$, $\omega_p' = \sqrt{3}\omega_p$ and $\omega_p = 0.5c$.

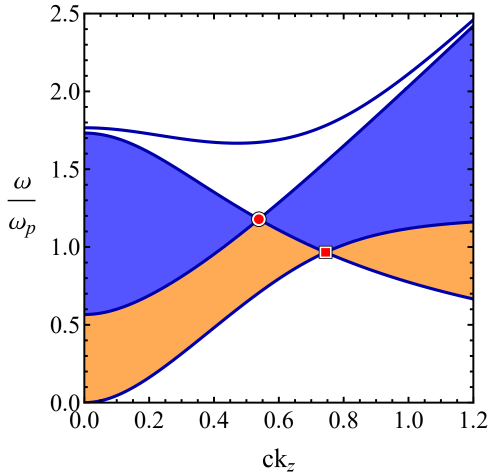

Figure 4.9: Dispersion in the k_z axis exhibiting the two regions of interest in blue and orange. The parameters used here were $k_{max} = \omega_p/c$, $\omega_c = 1.2\omega_p$, $\omega'_p = \sqrt{3}\omega_p$ and $\omega_p = 0.5c$.

This time, various cross sections were considered in order to fully characterize both regions. Six wave vector values in total: $k_z = 0$, $k_z = \frac{3}{4}W_1$, $k_z = W_1$, $k_z = \frac{5}{4}W_1$, $k_z = W_2$ and $k_z = \frac{5}{4}W_2$. If we look at figures 4.10-4.11, we can see the high-frequency band gaps in blue are present except at the first Weyl crossing and the low-frequency band gaps in orange are present except at the second Weyl crossing. The gap Chern number C^1_{gap} is relative to the blue region's band gaps and C^2_{gap} is relative to the orange region's band gaps. For $|k_z| < W_1$, $C^1_{gap} = +1$ and for $|k_z| > W_1$, $C^1_{gap} = 0$, so we can clearly see an influence from the Weyl point. Specifically, the blue band gaps in cross sections between the negative and positive inner Weyl points are topologically non-trivial, and the blue band gaps beyond these values are topologically trivial. A similar result is observed for the low-frequency band gaps. For $|k_z| < W_2$, $C^2_{gap} = -1$, hence the orange band gaps in cross sections between the positive and negative outer Weyl points are topologically non-trivial, and they are trivial $C^2_{gap} = 0$ for $|k_z| > W_2$.

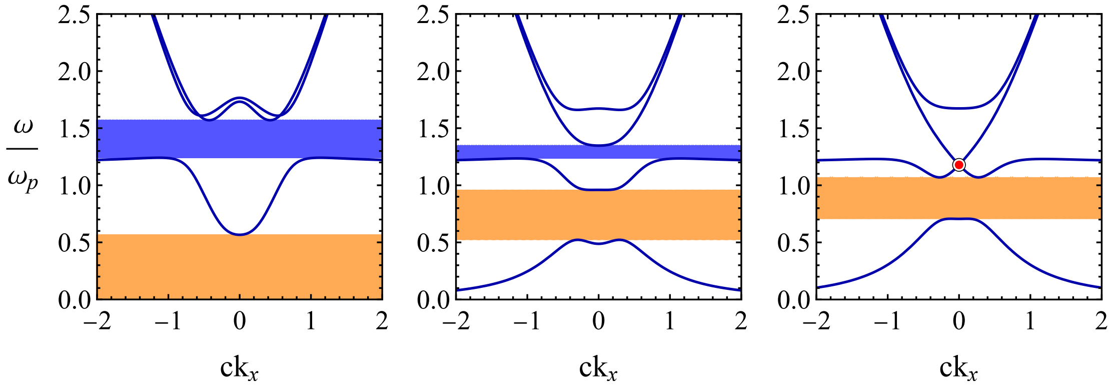

Figure 4.10: First set of cross sections of the 3-dimensional dispersion (fig. 4.8) for different k_z values. From left to right, $k_z = 0$, $k_z = \frac{3}{4}W_1$ and $k_z = W_1$. The high-frequency band gaps are highlighted in blue, the low-frequency ones in orange and the inner Weyl point with the red circle. The parameters used here were $k_{max} = \omega_p/c$, $\omega_c = 1.2\omega_p$, $\omega'_p = \sqrt{3}\omega_p$ and $\omega_p = 0.5c$.

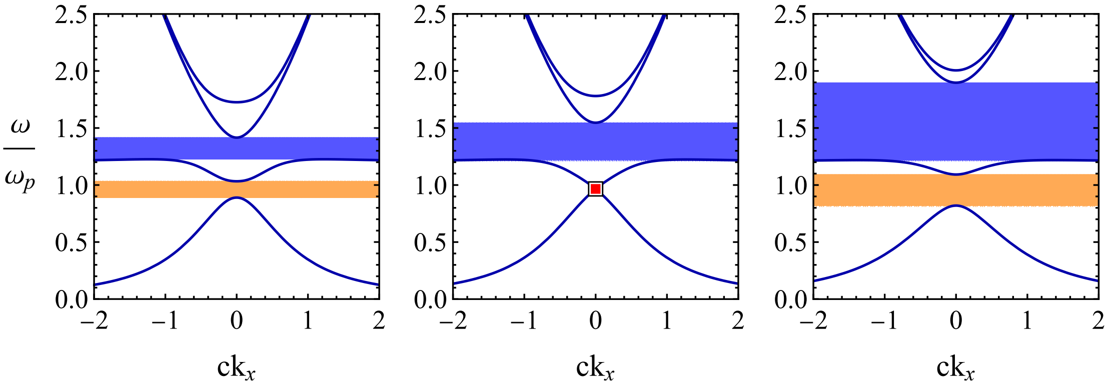

Figure 4.11: Second set of cross sections of the 3-dimensional dispersion (fig. 4.8) for different k_z values. From left to right, $k_z = \frac{5}{4}W_1$, $k_z = W_2$ and $k_z = \frac{5}{4}W_2$. The high-frequency band gaps are highlighted in blue, the low-frequency ones in orange and the outer Weyl point with the red square. The parameters used here were $k_{max} = \omega_p/c$, $\omega_c = 1.2\omega_p$, $\omega'_p = \sqrt{3}\omega_p$ and $\omega_p = 0.5c$.

This corroborates the fact that the Weyl points are indeed sources and drains of Berry curvature, and so it is consistent with the emergence of the non-trivial topological properties in a magnetized plasma [24], because the cross section's band gaps in the regions confined between each pair were shown to be topologically non-trivial. It also explains why the orange band gaps of the hydrodynamic model are in turn trivial, since they are not confined between any pair of Weyl points.

Finally, to complete this study and to conclude the main objective of this thesis, we will quantify the Weyl points' monopole charge. As previously explained, this is obtained by computing the difference of the gap Chern numbers in cross sections situated before and after the crossing, in a momentum space path across it. Specifically, the magnitude of the topological charge is given by the absolute difference of the gap chern numbers. The sign can only be attributed by defining the order in which the difference is computed. We will assume the negative orientation of the k_z axis as a convention to determine the order of the difference, which means that the minuend will be the gap Chern number in a cross section with a higher k_z than that of the subtrahend. The topological charge of the inner Weyl point with positive momentum is $0 - 1 = -1$ since before the crossing, the gap Chern number is $C^1_{gap} = +1$ and after it is $C^1_{gap} = 0$. This is because the band gaps in the cross sections after the crossing are trivial, so the sum between C^1_{gap} before the crossing and the topological charge of the Weyl degeneracy should be zero. The outer Weyl point in the positive wave vector space has a topological charge of $0 - (-1) = +1$, since before the crossing the gap Chern number is $C^2_{gap} = -1$ and after it is $C^2_{gap} = 0$, by the same logic. The topological charge of the Weyl points that arise in the negative wave vector space have symmetric values to those in positive wave vector space. This is congruent with the fact that a pair of Weyl points constitute one source and one sink of Berry flux. The results are summarized in picture 4.12.

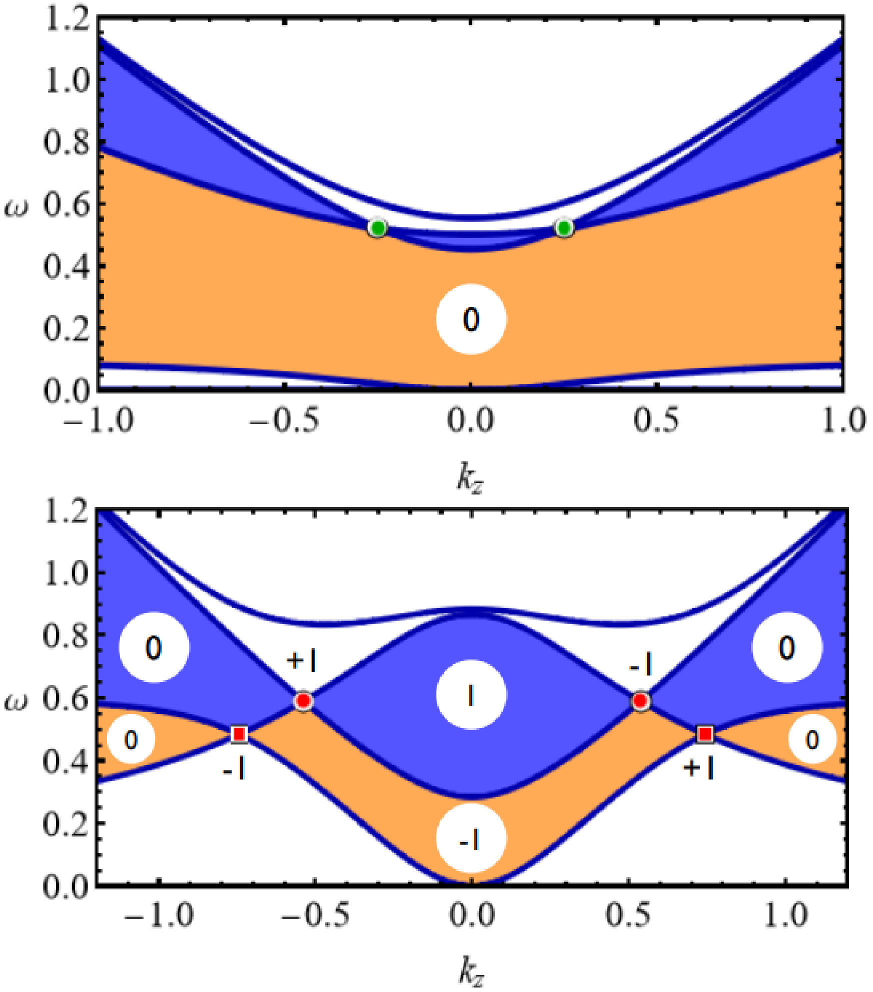

Figure 4.12: The plot on top is the k_z axis dispersion of the hydrodynamic model with the Weyl pair as green circles. The plot on the bottom is the k_z axis dispersion of the cut-off model with the inner Weyl pair as red circles and the outer pair as red squares. The numbers in white circles represent the gap Chern numbers obtained in each region. Near the Weyl points of the cut-off model you can see the number that represents their topological charge. The parameters used for the hydrodynamic model were $\beta = 0.6c$, $\omega_c = 0.2\omega_p$, $\omega'_p = \omega_p$ and $\omega_p = 0.5c$ and the ones used for the full cut-off model were $k_{max} = \omega_p/c$, $\omega_c = 1.2\omega_p$, $\omega'_p = \sqrt{3}\omega_p$ and $\omega_p = 0.5c$.

4.3 Convergence Study

Since the program that computes gap Chern numbers is a numerical implementation of the Green's function formalism (2.13), one is concerned about the convergence of the numerical method. This is because the result of a numerical method can usually only give an approximation of the analytical result, up to a certain error. Regarding numerical integration, a better convergence is equivalent to a lower absolute error which for our case is measured between the result of the program and the actual integer value of the gap Chern number. The parameters that influence the convergence of this program can be divided into two groups: model parameters that combine the constitutive parameters and momentum space value k_z that is fixed and from where the cross sections are taken; and the program parameters that are simply the ones used in the implemented numerical method like ξ_{max}, N and N_w, described in section 2.2.1. The fact that the constitutive parameters are important variables is not surprising because they control many aspects of the system, from the amplitude of band gaps to the case of having or not a well-defined topology.

The model that will be used to illustrate the influence of such variables on the numerical convergence is the magnetized plasma with a full cut-off having $k_{max} = \omega_p/c$, $\omega_c = 1.2\omega_p$, $\omega_p' = \sqrt{3}\omega_p$ and $\omega_p = 0.5c$. Firstly, we will focus on the topologically non-trivial blue subregion between the inner pair of Weyl points. Specifically, the high-frequency band gap on the left plot of figure 4.10 in the $k_z = 0$ cross section, with a gap Chern $C^1_{gap} = 1$.

Firstly, we will see the effect of the program parameters ξ_{max}, N and N_w. As the value of these parameters increase, we observe convergence to the integer gap Chern number. This can be graphically observed in figures 4.13 and 4.14.

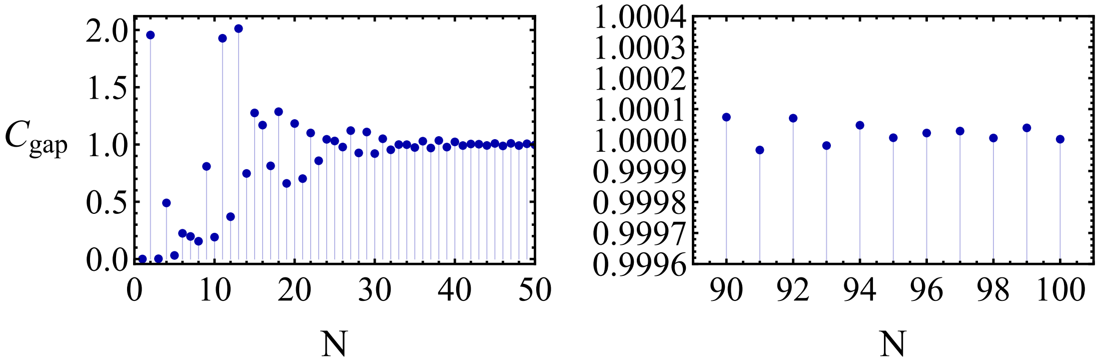

Figure 4.13: Convergence study of the numerical gap Chern number of the high-frequency band gap in $k_z = 0$ as a function of N, for a full cut-off model with the parameters above. The parameters used here were $N_w = 150$, $\xi_{max} = 3$ and $\omega'_{gap} = 0.7$.

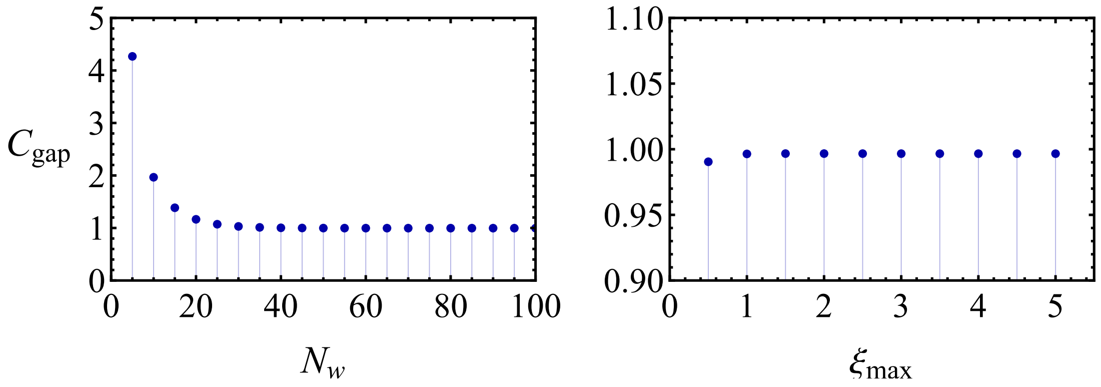

Figure 4.14: Convergence study of the numerical gap Chern number of the high-frequency band gap in $k_z = 0$ as a function of N_w and ξ_{max}, for a full cut-off model with the parameters above. The parameters used on the right plot were $N = 50$, $\xi_{max} = 3$ and $\omega'_{gap} = 0.7$ and on the left plot $N_w = 150$, $N = 50$ and $\omega'_{gap} = 0.7$.

The parameters N and N_w have a greater impact, as opposed to ξ_{max} which can be small and still guarantee a good convergence.

Momentum space location has a very big influence in the convergence of program results. Explicitly, in the context of our problem, this location is the value in the k_z axis from which the cross sections are taken. Generally speaking, the more we increase k_z, the better the convergence. This is true except in one very important case. When the topological characterization is executed in cross sections with k_z values that are small deviations from the Weyl crossing, the numerical gap Chern number diverges when using the same program parameters (except for ω'_{gap} since of course it needs to be adapted to be confined within the different band gaps in each cross section). This divergence in the proximity of the frontier between two topologically inequivalent regions is due to the extremely narrow band gaps around the crossing. This is better understood graphically in figure 4.15 that showcases the numerical gap Chern number of the band gaps situated in the blue region (fig. 4.9) from cross sections with different k_z values.

To further exemplify the influence of momentum space location in the convergence we will take two different k_z values after the positive inner Weyl point $k_z = W_1$, in the topologically trivial blue subregion. For $k_z = \frac{3}{2}W_1$, the numerical gap Chern number is $C^1_{gap} = -0.001411$ and for a really large value ($k_z \gg W_1$) like $k_z = 50W_1$, we get $C^1_{gap} = -5.44789 \times 10^{-10}$, for the same program parameters. This seems to be congruent with the effect of the limit $k_z \to \infty$, where the material response becomes reciprocal, and so the numerical gap Chern number converges significantly faster to 0.

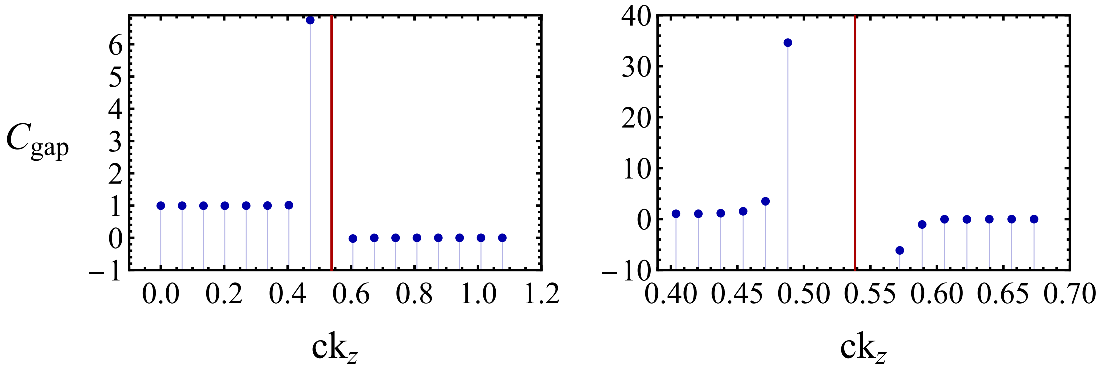

Figure 4.15: Convergence study of the numerical gap Chern number for band gaps in the blue region of figure 4.9 in different cross sections, for a full cut-off model with the same constitutive parameters. The red line represents the frontier between the two topologically inequivalent subregions at the wave vector location of the Weyl crossing. The program parameters used here were $N = 50$, $N_w = 100$, $\xi_{max} = 3$ and ω'_{gap} takes a different value for cross section.

Another important parameter is ω'_{gap}, the real-valued frequency of the contour for the integration in frequency, which should be positioned in the middle of the band gap, since the numerical result may diverge if this value is too close to a dispersion band.

5

Conclusion

We studied two photonic structures that were shown to possess Weyl points. The first one was a helical metamaterial which is reciprocal and the second one was an electron plasma biased with a static magnetic field which is nonreciprocal.

To acquire Weyl points, it is necessary to break either time-reversal symmetry or inversion symmetry. The helical metamaterial has no inversion symmetry precisely because of the helical geometry, but this alone does not guarantee the twofold point-like degeneracies in the system. The permittivity components in the $\hat{\mathbf{x}}$ and $\hat{\mathbf{y}}$ directions (for a helix oriented along the $\hat{\mathbf{z}}$ direction) must also be different, or in other terms, the system's response must be anisotropic in planes that are orthogonal to the helix orientation. This is the reason why the unit cell has an elliptical helix.

In the case of the magnetized plasma, time-reversal symmetry is broken by the applied magnetic field. This is the reason why it is nonreciprocal which is a necessary property to obtain non-trivial topological invariants in this system [14], such as the gap Chern numbers. The existence of Weyl crossings in this medium is thus inherently connected with its nonreciprocity since they have been shown to be responsible for the non-trivial topological properties of the magnetized plasma [24]. This is corroborated by the results in section 4.2 of this dissertation.

The emergence of these Weyl degeneracies in both systems is similar, in the sense that the point-like band crossings occur along a single direction of propagation $\mathbf{k}$, between one longitudinal mode and transverse modes. Such direction is determined differently for each medium. It is given by the helices' principal axis for the helical metamaterial, and in the case of the magnetized plasma it is given by the direction of the static bias magnetic field.

The Weyl point generated by the crossing between a flat longitudinal mode and a transverse mode rests at the boundary between type-I and type-II. A type-I Weyl system possesses isofrequency surfaces surrounding the Weyl point's frequency which are ellipsoids and a type-II system possesses isofrequency surfaces which are hyperboloids. To acquire either type, nonlocality must be introduced into the system. If the nonlocality acts on the longitudinal mode by bending it upward (second derivative with respect to the wave vector is positive), the isofrequency curves around the crossing turn hyperbolic, thus it changes into a type-II Weyl point. If it bends downward (negative second derivative), the isofrequency curves turn into closed ellipses, thus changing it to a type-I Weyl point.

The introduction of spatial dispersion is a consequence of the regularization procedure for the local magnetized plasma due to its ill-defined topology. It was possible to replicate the two different types of Weyl crossings with the two solutions explored in sections 3.2.2-3.2.3. On the other hand, the helical metamaterial possesses intrinsic strong spatial dispersion for any frequency and even in the very large wavelength limit [29]. By analysing the effective medium theory in [4], we showed that this nonlocality can only originate the second type.

We concluded that nonlocality is necessary to ensure that the topology of a 3-dimensional magnetized plasma is well-defined, in order to obtain integer gap Chern numbers, which may be non-trivial. A wave vector cut-off is required to regularize the topology of an electromagnetic continuum in a way that its nonreciprocal response is suppressed for large wave vectors. In section 4.2 we observed that after this regularization, the gap Chern numbers indeed converged to integers (some non-trivial), with spatially dispersive models.

The most important and novel conclusions were derived in section 4.2, after the topological characterization of the band structures of two nonlocal models of a magnetized plasma. Taking into account the geometry of the problem described in this chapter (4), it was numerically shown that topologically non-trivial band gaps exist in specific regions of the 3-dimensional dispersion. These regions are confined between each Weyl point pair in momentum space. By taking cross sections of the dispersion in orthogonal directions ($k_{x,y}$) relatively to the axis that connects the pair (k_z) and if we can guarantee the existence of full band gaps in these cuts that are situated in the region of interest, we can compute their gap Chern number. Our results show that these band gaps are non-trivial. In fact, the gap Chern number remains constant for any cross section in this region. This is expected since the band gaps are all connected if we are looking along the k_z axis and they only change in amplitude in an adiabatic way. The situation is completely different if we consider cross sections immediately before and after the Weyl crossing. As it was seen best in figure 4.12, the gap Chern numbers are different in each situation, becoming trivial in cross sections beyond the interval in wave vector space that directly connects the pair. This is also expected since the gaps in these cross sections are all connected even when $k_z \to \infty$, consequently the gap Chern number must be constant, and since in this limit the electromagnetic response is reciprocal, it should be indeed zero.

The previous arguments explain why the gap Chern numbers are trivial in cross sections situated in a region that is not bounded by any Weyl points, as is the case of the low-frequency (orange) region of the hydrodynamic model that was characterized in section 4.2. Equivalently, since there are no Weyl crossings in this region, there is no Berry curvature flux being captured in the respective band gaps of the cross sections with our Green's function method.

The difference of the gap Chern numbers before and after the crossing is the magnitude of the topological charge of the Weyl point. However, the sign can only be attributed by defining the order in which the difference is computed. Such order is given by a trajectory with positive or negative orientation in the direction of the axis that unites the Weyl pair. This trajectory is defined before-hand as a convention and maintained for the computation of topological charges for all Weyl crossings. As we conclude in section 4.2, for each pair with opposite wave vector values, there is one with a positive sign and another with a negative sign, representing the existence of a source and a drain of Berry flux. Our method can then quantify the magnitude of the topological charge and the relative signs between pairs (figure 4.12), but cannot distinguish which Weyl point has the positive or the negative charge out of each pair.

In conclusion, we have applied a first principles method to the calculation of topological charge of Weyl points in continuous media. Unlike standard methods based on the direct computation of the Berry curvature, this approach does not require the calculation of the eigenvectors at each value of the wave vector and is thus more computationally efficient. Future work may include analysing the topology of the helical metamaterial and study protected edge modes in these systems.

Bibliography

[1] N. Engheta and R. W. Ziolkowski, *Metamaterials: Physics and Engineering Explorations*. John Wiley & Sons and IEEE Press, 2006.

[2] M. G. Silveirinha, "Nano-electromagnetics: Plasmonics and metamaterials," lecture notes, Dec 2019.

[3] P. Huidobro, M. Silveirinha, E. Galiffi, and J. Pendry, "Homogenization theory of space-time metamaterials," *Phys. Rev. Applied*, vol. 16, p. 014044, Jul 2021. [Online]. Available: https://link.aps.org/doi/10.1103/PhysRevApplied.16.014044

[4] M. G. Silveirinha, "Design of linear-to-circular polarization transformers made of long densely packed metallic helices," *IEEE Transactions on Antennas and Propagation*, vol. 56, no. 2, pp. 390–401, 2008.

[5] V. G. Veselago, "The electrodynamics of substances with simultaneously negative values of ϵ and µ," *Soviet Physics Uspekhi*, vol. 10, no. 4, p. 509, apr 1968. [Online]. Available: https://dx.doi.org/10.1070/PU1968v010n04ABEH003699

[6] T. Ozawa, H. M. Price, A. Amo, N. Goldman, M. Hafezi, L. Lu, M. C. Rechtsman, D. Schuster, J. Simon, O. Zilberberg, and I. Carusotto, "Topological photonics," *Rev. Mod. Phys.*, vol. 91, p. 015006, Mar 2019. [Online]. Available: https://link.aps.org/doi/10.1103/RevModPhys.91.015006

[7] M. S. Rider, S. J. Palmer, S. R. Pocock, X. Xiao, P. A. Huidobro, and V. Giannini, "A perspective on topological nanophotonics: Current status and future challenges," *J. Appl. Phys. 1*, vol. 125, p. 120901, Mar 2019. [Online]. Available: https://doi.org/10.1063/1.5086433

[8] F. D. M. Haldane and S. Raghu, "Possible realization of directional optical waveguides in photonic crystals with broken time-reversal symmetry," *Phys. Rev. Lett.*, vol. 100, p. 013904, Jan 2008. [Online]. Available: https://link.aps.org/doi/10.1103/PhysRevLett.100.013904

[9] S. Raghu and F. D. M. Haldane, “Analogs of quantum-hall-effect edge states in photonic crystals,” *Phys. Rev. A*, vol. 78, p. 033834, Sep 2008. [Online]. Available: https://link.aps.org/doi/10.1103/PhysRevA.78.033834

[10] M. G. Silveirinha, “Bulk-edge correspondence for topological photonic continua,” *Phys. Rev. B*, vol. 94, p. 205105, Nov 2016. [Online]. Available: https://link.aps.org/doi/10.1103/PhysRevB.94.205105

[11] M. G. Silveirinha, “Proof of the bulk-edge correspondence through a link between topological photonics and fluctuation-electrodynamics,” *Phys. Rev. X*, vol. 9, p. 011037, Feb 2019. [Online]. Available: https://link.aps.org/doi/10.1103/PhysRevX.9.011037

[12] M. Kim, Z. Jacob, and J. Rho, “Recent advances in 2d, 3d and higher-order topological photonics,” *Light: Science & Applications*, vol. 9, p. 130, jul 2020. [Online]. Available: https://doi.org/10.1038/s41377-020-0331-y

[13] M. G. Silveirinha, “Topological theory of non-hermitian photonic systems,” *Phys. Rev. B*, vol. 99, p. 125155, Mar 2019. [Online]. Available: https://link.aps.org/doi/10.1103/PhysRevB.99.125155

[14] M. G. Silveirinha, “Topological classification of chern-type insulators by means of the photonic green function,” *Phys. Rev. B*, vol. 97, p. 115146, Mar 2018. [Online]. Available: https://link.aps.org/doi/10.1103/PhysRevB.97.115146

[15] F. R. Prudêncio and M. G. Silveirinha, “First principles calculation of topological invariants of non-hermitian photonic crystals,” *Communications Physics*, vol. 3, p. 221, Dec 2020. [Online]. Available: https://doi.org/10.1038/s42005-020-00482-3

[16] M. G. Silveirinha, “Chern invariants for continuous media,” *Phys. Rev. B*, vol. 92, p. 125153, Sep 2015. [Online]. Available: https://link.aps.org/doi/10.1103/PhysRevB.92.125153

[17] F. R. Prudêncio and M. G. Silveirinha, “Ill-defined topological phases in local dispersive photonic crystals,” *Phys. Rev. Lett.*, vol. 129, p. 133903, Sep 2022. [Online]. Available: https://link.aps.org/doi/10.1103/PhysRevLett.129.133903

[18] L. Lu, L. Fu, J. D. Joannopoulos, and M. Soljačić, “Weyl points and line nodes in gyroid photonic crystals,” *Nature Photonics*, vol. 7, Apr 2013. [Online]. Available: https://doi.org/10.1038/nphoton.2013.42

[19] L. Lu, J. D. Joannopoulos, and M. Soljačić, “Topological photonics,” *Nature Photonics*, vol. 8, p. 821, nov 2014. [Online]. Available: https://doi.org/10.1038/nphoton.2014.248

[20] M. Xiao, Q. Lin, and S. Fan, “Hyperbolic weyl point in reciprocal chiral metamaterials,” *Phys. Rev. Lett.*, vol. 117, p. 057401, Jul 2016. [Online]. Available: https://link.aps.org/doi/10.1103/PhysRevLett.117.057401

[21] S. Howard, L. Jiao, Z. Wang, N. Morali, R. Batabyal, P. Kumar-Nag, N. Avraham, H. Beidenkopf, P. Vir, E. Liu, C. Shekhar, C. Felser, T. Hughes, and V. Madhavan, “Evidence for one-dimensional chiral edge states in a magnetic weyl semimetal co3sn2s2,” *Nature Communications*, vol. 12, Jul 2021. [Online]. Available: https://doi.org/10.1038/s41467-021-24561-3

[22] Y. Yang, W. Gao, L. Xia, H. Cheng, H. Jia, Y. Xiang, and S. Zhang, “Spontaneous emission and resonant scattering in transition from type i to type ii photonic weyl systems,” *Phys. Rev. Lett.*, vol. 123, p. 033901, Jul 2019. [Online]. Available: https://link.aps.org/doi/10.1103/PhysRevLett.123.033901

[23] B. Yang, Q. Guo, B. Tremain, L. E. Barr, W. Gao, H. Liu, B. Béri, Y. Xiang, D. Fan, A. P. Hibbins, and S. Zhang, “Direct observation of topological surface-state arcs in photonic metamaterials,” *Nature Communications*, vol. 8, Jul 2017. [Online]. Available: https://doi.org/10.1038/s41467-017-00134-1

[24] W. Gao, B. Yang, M. Lawrence, F. Fang, B. Béri, and S. Zhang, “Photonic weyl degeneracies in magnetized plasma,” *Nature Communications*, vol. 7, p. 12435, Aug 2016. [Online]. Available: https://doi.org/10.1038/ncomms12435

[25] D. Wang, B. Yang, W. Gao, H. Jia, Q. Yang, X. Chen, M. Wei, C. Liu, M. Navarro-Cía, J. Han, W. Zhang, and S. Zhang, “Photonic weyl points due to broken time-reversal symmetry in magnetized semiconductor,” *Nature Physics*, vol. 15, Nov 2019. [Online]. Available: https://doi.org/10.1038/s41567-019-0612-7

[26] Wolfram. (2022) Wolfram Mathematica. [Online]. Available: https://www.wolfram.com/mathematica/

[27] F. R. Prudêncio and M. G. Silveirinha, “First principles calculation of the topological phases of the photonic haldane model,” *Symmetry*, vol. 13, 2021. [Online]. Available: https://www.mdpi.com/2073-8994/13/11/2229

[28] J. A. Kong, *Electromagnetic Wave Theory*. EMW Publishing, 2021.

[29] P. A. Belov, R. Marqués, S. I. Maslovski, I. S. Nefedov, M. Silveirinha, C. R. Simovski, and S. A. Tretyakov, “Strong spatial dispersion in wire media in the very large wavelength limit,” *Phys. Rev. B*, vol. 67, p. 113103, Mar 2003. [Online]. Available: https://link.aps.org/doi/10.1103/PhysRevB.67.113103

[30] I. Almog, M. Bradley, and V. Bulović. Mit opencourseware: 6.007 electromagnetic energy: From motors to lasers - the lorentz oscillator and its applications. [Online]. Available: http://ocw.mit.edu

[31] M. G. Silveirinha, “Topological angular momentum and radiative heat transport in closed orbits,” *Phys. Rev. B*, vol. 95, p. 115103, Mar 2017. [Online]. Available: https://link.aps.org/doi/10.1103/PhysRevB.95.115103

[32] D. E. Fernandes, R. A. M. Pereira, S. Lannebère, T. A. N. Morgado, and M. G. Silveirinha, “Experimental verification of ill-defined topologies and energy sinks in electromagnetic continua,” *Advanced Photonics*, vol. 4, no. 3, p. 035003, 2022. [Online]. Available: https://doi.org/10.1117/1.AP.4.3.035003

[33] D. E. Fernandes and M. G. Silveirinha, “Topological origin of electromagnetic energy sinks,” *Phys. Rev. Applied*, vol. 12, p. 014021, Jul 2019. [Online]. Available: https://link.aps.org/doi/10.1103/PhysRevApplied.12.014021